Physics under extreme magnetic fields: probing the curious case of peculiar magnetars

M.Sc. Thesis

Submitted in partial fulfillment of the requirements for the awards of the degree
of
Master of Science

by

Nityananda Padhi



Department of Astronomy, Astrophysics and Space Engineering

INDIAN INSTITUTE OF TECHNOLOGY INDORE

May 18, 2026

INDIAN INSTITUTE OF TECHNOLOGY INDORE

CANDIDATE'S DECLARATION

I hereby certify that the work which is being presented in the thesis entitled **Physics under extreme magnetic fields : Probing the curious case of peculiar magnetars** in the partial fulfillment of the requirements for the award of the degree of **MASTER OF SCIENCE** and submitted in the **Department of Astronomy, Astrophysics and Space Engineering, Indian Institute of Technology Indore**, is an authentic record of my own work carried out during the time period from June 2025 to May 2026 under the supervision of Dr. Manoneeta Chakraborty, Associate Professor.

The matter presented in this thesis has not been submitted by me for the award of any other degree of this or any other institute.

08/05/26

Signature of the student with date
Nityananda Padhi

This is to certify that the above statement made by the candidate is correct to the best of my knowledge.

Manoneeta Chakraborty

8/5/2026

Signature of the Supervisor of

M.Sc. thesis (with date)

Dr. Manoneeta Chakraborty

Nityananda Padhi has successfully given his M.Sc. Oral Examination held on **06/05/2026**.

Manoneeta Chakraborty

Signature(s) of Supervisor(s) of MSc thesis
Date: 8/5/2026

Manoneeta Chakraborty

Programme Coordinator, M.Sc.
Date: 8/5/2026

Manoneeta Chakraborty

Convenor, DPGC
Date: 8/5/2026

HoD, DAASE
Date: 8/5/2026

Acknowledgements

I would like to express my deepest gratitude to my supervisor, **Dr. Manoneeta Chakraborty**, for her guidance, encouragement, and support throughout the course of this thesis. Her patience, insightful discussions, and constant motivation have played a fundamental role in shaping both this work and my broader understanding of neutron stars and magnetar physics. I am truly grateful for the opportunity to work under her supervision, and for all the knowledge, trust, and encouragement she has provided during this journey.

I am also grateful to **Dr. Mayuresh Surnis** and **Abhinandan Yadav** for providing the radio observational data used in this work and for their kind support throughout the project. I sincerely appreciate his valuable input, and the opportunity to incorporate radio perspectives into understanding the fascinating behaviour of XTE J1810−197.

I would like to thank my labmate **Kaivan**, who has been a constant source of support throughout my thesis journey. From scientific discussions to tea breaks at Yewale in the afternoon, his encouragement and companionship have meant a great deal to me. I would also like to thank my other labmates, **Aromal**, **Jibin**, and **Biki**, for creating a supportive and enjoyable research environment filled with discussions, laughter, and shared struggles that made this journey far more memorable. A special thanks to **Manpreet** for working on effective CS2 strategies that made us feel like a pro player, even when both of our projects were hanging by a thread, and to **Mayukh** for recommending great story games that made the master's thesis journey enjoyable. I am equally grateful to my friends, **Kartik**, **Sangeetha**, **Vishal**, **Sangeeta**, and **Kanishka**, for their constant encouragement, motivation, and support throughout this journey.

Abstract

Magnetars are a rare class of young neutron stars characterized by extremely strong internal magnetic fields exceeding 10^{14} G. These intense magnetic fields power their high-energy emission, placing magnetars among the most luminous X-ray sources in the neutron-star population. They have spin periods typically in the range of 2–12 s, which exhibit remarkable temporal and spectral variability. They are known for producing transient X-ray and soft gamma-ray outbursts during which their luminosity can increase by several orders of magnitude, followed by a long-term relaxation toward quiescence. These events provide a unique window into the processes governing magnetic-field decay, crustal heating, and magnetospheric reconfiguration.

Although magnetars predominantly emit in the high-energy X-ray and gamma-ray bands and are generally radio-quiet. However, a small subset (5 out of 30) exhibits transient radio-loud phases that appear to be linked to magnetospheric reactivation. The broadband radiative behavior of magnetars holds essential clues to understanding their emission physics and their connection to canonical rotation-powered pulsars. They can also be associated with fast radio bursts and other transient phenomena of possible magnetar origin. Studying how the spectrum and timing of these peculiar magnetars change across different energy bands is important for understanding the behavior of magnetars and their emission process.

In this project, we present a detailed analysis of the timing and spectral properties of the transient magnetar *XTE J1810–197*, a well-studied source that underwent a major outburst in 2003 and remained in a prolonged quiescence phase until its reactivation in late 2018. We investigate the post-reactivation behavior of the magnetar over multiple epochs. Our timing study focuses on determining the spin period evolution, examining the evolution of the pulse profile shape, and quantifying pulse parameters such as the pulsed fraction (PF) and fractional amplitude (FA) across different energy bands. These measurements allow us to probe changes in the surface geometry, identify the possible locations of hotspots, and detect potential signatures of magnetic-field reconfiguration.

Contents

List of Figures

List of Tables

1 Introduction **1**

1.1 Magnetars . . . 1

1.1.1 An overview . . . 1

1.1.2 Internal mechanism of magnetars . . . 3

1.1.3 Basic observational properties . . . 5

1.2 Transient behaviour in magnetars . . . 6

1.3 Timing properties of magnetars . . . 7

1.3.1 Pulse Profile . . . 7

1.3.2 Pulsed fraction . . . 7

1.3.3 Fractional amplitude . . . 8

1.4 Why XTE J1810-197? . . . 9

1.4.1 Previous Studies on this magnetar post 2018 . . . 10

1.5 Research objective . . . 11

2 Instrument **13**

2.1 XMM-NEWTON Telescope . . . 13

2.1.1 Basic Characteristics . . . 14

2.1.2 Spacecraft overview . . . 14

2.1.3 Scientific Instruments . . . 15

2.1.4 Data archival and Download . . . 17

2.2 Neil Gehrels Swift Observatory . . . 18

2.2.1 Instrument Overview . . . 18

2.2.2 Basic characteristics of XRT . . . 19

2.2.3 Data Archive and Acquisition . . . 20

3 Timing Properties **22**
3.1 Light Curves . . . 23
3.1.1 Data Reduction . . . 23
3.1.2 Light Curve plots . . . 25
3.1.3 Post-outburst X-ray Flux Evolution . . . 27
3.2 Estimation of Spin frequency and Pulse Profile plot . . . 29
3.2.1 Construction of Background-Subtracted Pulse Profiles from XMM-Newton Observations . . . 29
3.2.2 Temporal Evolution of Pulse Profiles from XMM-Newton Observations 33
3.2.3 Construction of Background-Subtracted Pulse Profiles from *Swift*-XRT Observations . . . 34
3.2.4 Temporal Evolution of Pulse Profiles from *Swift*-XRT Observations . . 36
3.2.5 Spin frequency evolution . . . 37
3.3 Evolution of Pulse profile in different energy bands . . . 42
3.4 Fractional Amplitude of subpeaks . . . 50
3.4.1 Evolution of fractional amplitude with time . . . 50
3.4.2 Evolution of fractional amplitude in different energy bands . . . 55
3.4.3 Evolution of Fractional Amplitude with Energy for Each Observation . 57
3.5 Total Fractional amplitude . . . 60
3.6 Pulsed Fraction . . . 62
3.6.1 Evolution of Pulsed Fraction with energy . . . 62
3.6.2 Evolution of Pulsed Fraction with energy for each observation . . . 63
3.7 Correlation between X-ray pulsed fraction and radio flux density . . . 66

4 Spectral Properties **68**
4.1 Spectral Extraction . . . 69
4.2 Spectral Modelling . . . 70
4.2.1 Blackbody and Power-law Spectral Components . . . 70
4.2.2 Model Selection and Goodness of Fit . . . 71
4.3 Temporal Evolution of spectral parameters . . . 75
4.3.1 Flux Evolution . . . 78

5 Summary and Discussion **80**

6 Future directions **87**

7 Appendix **88**
7.1 XMM NEWTON data reduction using SAS . . . 88

7.1.1 Calibrating the Data 88
7.2 Cleaning the Data and Plotting the light curve 90
7.2.1 Generate a Light Curve for Background Check 90
7.2.2 Plot the Light Curve 91
7.2.3 Determine Background Threshold using Sigma Clipping 91
7.2.4 Filter the Event File using GTI 93
7.2.5 Create a Cleaned Image from the Filtered Event List 93
7.2.6 Display the Clean Image in DS9 94
7.2.7 Apply Barycentric Correction 95
7.2.8 Extract the Source Light Curve 95
7.2.9 Extract the Background Light Curve 95
7.2.10 Apply Light Curve Corrections 96

List of Figures

1.1 Rotation powered pulsar. Image source : Bell Burnell 2017 2

1.2 Accretion powered pulsars. Image source: Moscow Institute of Physics and Technology 2

1.3 Schematic illustration of the dynamo mechanism in a rapidly spinning newborn neutron star Image source: Dave dooling, NASA Marshall Space Flight Center. 3

1.4 Schematic illustration of magnetar outburst initiation. Crustal motions twist the external magnetic field lines, storing energy in the magnetosphere. When the twist becomes unstable, the field releases energy through magnetospheric currents, heating the surface and producing enhanced X-ray emission. Image Source : https://ariccio.com/2013/06/08/magnetars-soft-gamma-repeaters-very-strong-magnetic-fields/ 4

2.1 View of the XMM-NEWTON spacecraft subsystems. Image credit : Jansen et al. 2001 14

2.2 The EPIC pn camera layout as displayed in SAS, showing the orientation of the RAWX/RAWY and DETX/DETY axes and their alignment with the RGS dispersion direction. Image credit : XMM-Newton Science Operations Centre 2022 16

3.1 Light curve plots for all 6 XMM-NEWTON observations. 25

3.2 Light curve plots from selected Swift observations, sampled at approximately yearly intervals from the full dataset. 26

3.3 *Swift*-XRT count rate evolution of the source in the 0.3–10 keV band. The red dashed line marks the epoch of the 2018 outburst. The black curve represents the best-fit exponential decay model. 27

3.4 Frequency corresponding to maximum fractional amplitude for ObsID 0804590701. f = 0.18046 Hz 32

3.5 Pulse profile corresponding to the best-fit spin frequency $f = 0.18046$ Hz for ObsID 0804590701, along with the harmonic fit. 32

3.6 Best pulse profile fits for six observations (XMM-Newton). From left to right and top to bottom, (a) 0804590701 (03-03-2018), (b) 0784303101 (04-03-2019), (c) 0784303201 (22-09-2019), (d) 0913991301 (17-09-2022), (e) 0921410201 (24-09-2023), and (f) 0921410301 (07-04-2024). 33
3.7 Fractional amplitude as a function of trial frequency for a representative *Swift* observation. The peak corresponds to the best-fit spin frequency where phase coherence is maximized. 35
3.8 Pulse profile corresponding to the best-fit spin frequency $f = 0.18044$ Hz for ObsID 2019_03_00031335011, along with the harmonic fit. 35
3.9 Pulse profiles obtained from selected *Swift XRT* observations spanning multiple epochs. Each profile is constructed using the best-fit frequency and corresponding number of harmonics (m) as listed in Table 3.1. 36
3.10 Spin frequency evolution pre and post outburst. 40
3.11 Best-fit pulse profiles for energy bands 0.2–0.8 keV, 1.0–1.2 keV, 1.4–1.6 keV, 1.8–2.0 keV, 3.0–4.0 keV, and 4.8–10.0 keV. All profiles are modeled using a single harmonic component. 43
3.12 Best fit pulse profile plots for energy bands: 0.2 -2 keV, 2-4 keV, 4-6 keV, 6-8 keV, 8-10 keV, respectively. No. of harmonics used (from left to right and top to bottom): 2,2,2,2,1 respectively. 44
3.13 Best-fit pulse profiles for energy bands 0.2–2 keV, 2–4 keV, 4–6 keV, 6–8 keV, and 8–10 keV. The number of harmonics used (left to right and top to bottom) are 2, 3, 3, 2, and 1, respectively. 45
3.14 Best-fit pulse profiles for energy bands 0.2–0.8 keV, 1.0–1.2 keV, 1.4–1.6 keV, 1.8–2.0 keV, 3.0–4.0 keV, and 4.8–10.0 keV. All profiles are modeled using a single harmonic component. 46
3.15 Best-fit pulse profiles for energy bands 0.4–1.0 keV, 1.0–1.6 keV, 1.6–1.8 keV, 2.0–3.0 keV, and 3.6–10.0 keV. All profiles are modeled using a single harmonic component. 47
3.16 Best-fit pulse profiles for energy bands 0.2–0.8 keV, 1.0–1.2 keV, 1.4–1.6 keV, 1.8–2.0 keV, 2.2–2.4 keV, and 3.1–10.0 keV. All profiles are modeled using a single harmonic component. 48
3.17 Evolution of fractional amplitude. 54
3.18 Energy-dependent fractional amplitude for all *XMM-Newton* observations, shown on logarithmic scales for both axes. 56
3.19 Energy dependence of the fractional amplitude for *XMM-Newton* observations. The top panel is shown in log–log scale, while the bottom panel is plotted in linear scale. 57

3.20 Energy dependence of the fractional amplitude for *XMM-Newton* observations. The top panel is plotted in linear scale, while the remaining panels are shown in log–log scale. . . . 58
3.21 Energy dependence of the fractional amplitude for the final *XMM-Newton* observation, shown in log–log scale. . . . 59
3.22 Evolution of the total fractional amplitude as a function of time. . . . 60
3.23 Energy-dependent pulsed fraction for all *XMM-Newton* observations, shown on logarithmic scales for both axes. . . . 62
3.24 Energy dependence of the pulsed fraction for the first *XMM-Newton* observation, shown in linear and log–log scales to highlight behaviour across different energy ranges. . . . 63
3.25 Energy dependence of the pulsed fraction for selected *XMM-Newton* observations. The first two panels are shown in linear scale, while the third panel is presented in log–log scale. . . . 64
3.26 Energy dependence of the pulsed fraction for *XMM-Newton* observations, shown in log–log scale. . . . 65
3.27 Evolution of X-ray Pulsed Fraction and Radio Flux density. . . . 67

4.1 Best fit XMM-Newton spectra for pre 0804590701 (top, 2BB) and peak of the outburst 0784303101 (bottom, 3BB). . . . 72
4.2 Best-fit XMM-Newton spectra showing spectral evolution from peak of the outburst 0784303201 (22-09-2019) and the later phase of the outburst 0913991301 (17-09-2022). The peak of the outburst has been fitted with 3BB components, and the later phase of the outburst has been fitted with 2BB components. . . . 73
4.3 Best-fit XMM-Newton spectra showing spectral evolution at the later phases of the outburst 0921410201 (24-09-2023) and 0921410301 (07-04-2024). Both of the spectra has been fitted with 2BB components. . . . 74
4.4 Temperature evolution. . . . 77
4.5 Radius evolution. The y-axis is in log scale. . . . 77
4.6 Flux evolution of each Blackbody components . . . 79
4.7 Final flux evolution . . . 79

7.1 Preliminary Light curve to check for background flares. A spike can be clearly seen. . . . 91
7.2 Plot depicting threshold to remove background flares. . . . 93
7.3 DS9 image for ObsID 0784303101 after filtering. This image is in Timing mode. 94

List of Tables

2.1 Summary of instrument characteristics of XMM-Newton (XMM-Newton Science Operations Centre 2022). 14
2.2 Summary of downloaded XMM-Newton datasets. 17
2.3 Key parameters of the Swift XRT instrument. 19
2.4 Log of observations with ObsID and observation dates. 20

3.1 Log of observations with estimated spin frequencies and associated harmonics. 37
3.2 Log of observations with measured fractional amplitudes and harmonics. . . . 50

4.1 Blackbody temperatures, normalizations, and inferred emitting radii assuming a source distance of 3.5 kpc. 76
4.2 Flux measurements from spectral fits 78

Chapter 1

Introduction

1.1 Magnetars

1.1.1 An overview

The formation of a neutron star is one of the most dramatic endpoints in stellar evolution, resulting from the core collapse supernova of a massive star. When a massive star, with a mass in the range of 10 to 25 times the mass of our sun (Turolla, Zane, and Watts 2015), exhausts its nuclear fuel in its core, the stellar core is no longer supported by thermal pressure and undergoes a rapid gravitational collapse, resulting in a supernova explosion. This forces electrons and protons to combine into neutrons and results in an object with a high density, with around 1 solar mass packed into a radius of a few tens of kilometres. These neutron stars possess extreme properties, which include powerful magnetic fields and rapid rotation.

The most well-known type of neutron star is the rotation-powered pulsar. These are rapidly spinning neutron stars whose emission is due to the loss of rotational kinetic energy. As their tightly collimated beams of electromagnetic radiation sweep across our line of sight, they produce highly regular periodic pulses, allowing them to function as exceptionally precise cosmic clocks (Kaspi and Beloborodov 2017). Another major class is the accretion-powered pulsars, found in binary systems. In these binary systems, material from a companion star is funnelled onto the magnetic poles of the neutron star. The release of gravitational potential energy in this process powers bright X-ray emission.

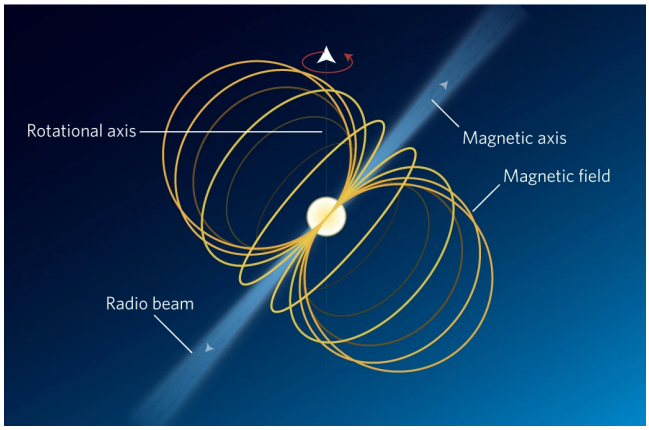


Figure 1.1: Rotation powered pulsar. Image source : Bell Burnell 2017

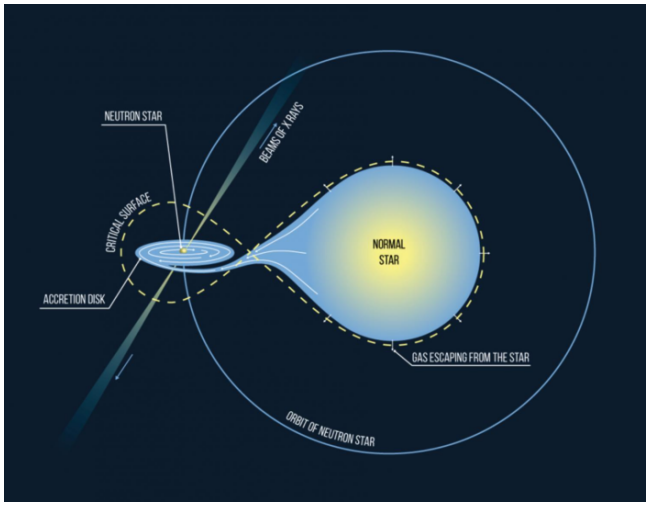


Figure 1.2: Accretion powered pulsars. Image source: Moscow Institute of Physics and Technology

Beyond these two families lies a third, more extreme class of neutron stars, which is the magnetars. Magnetars exhibit the strongest magnetic fields known in the universe, with strengths ($\sim 10^{14}$–10^{15} G), about 10^3 times higher than those of typical X-ray pulsars. These magnetars are powered by the slow decay and sudden reconfiguration of their magnetic fields, leading to their intense and often violent high-energy activity.

Historically, magnetars were observed to be in two main forms, Soft Gamma Repeaters (SGRs) and Anomalous X-ray Pulsars (AXPs). SGRs are famous for randomly releasing short, powerful bursts of gamma-rays. AXPs, on the other hand, are identified by their steady and unusually bright X-ray emission. Today, we understand that SGRs and AXPs are not separate types of objects but are instead two sides of the same coin.

Both are different forms of magnetar, and their behaviours are simply different expressions of the same powerful magnetic engine at their core (Kaspi and Beloborodov 2017).

1.1.2 Internal mechanism of magnetars

Magnetars are understood to have extremely strong magnetic fields, far stronger than those of ordinary neutron stars. According to the model proposed by Thompson and Duncan (Thompson and Duncan 1996), these fields are created when the neutron star is newly formed and still very hot and rapidly rotating. In this early phase, the intense convection and differential rotation inside the star can drive a dynamo mechanism as shown in figure 1.3, which efficiently amplifies the initial magnetic field to extreme strengths up to values of 10^{14}–10^{15} G. Such a huge magnetic field stores an enormous amount of energy inside the star and slowly changes over time. As it evolves, it pushes and strains the solid outer crust of the neutron star, making magnetars fundamentally powered by magnetic energy rather than by rotation (Kaspi and Beloborodov 2017).

The magnetic field changes slowly over years to centuries. This continuously puts stress on the crust. When the stress becomes too large, the crust cracks and suddenly releases an immense amount of magnetic energy. These events heat the surface and inject energetic particles into the surroundings of the magnetar. Observationally, these releases appear as bursts, flares, or longer X-ray outbursts.

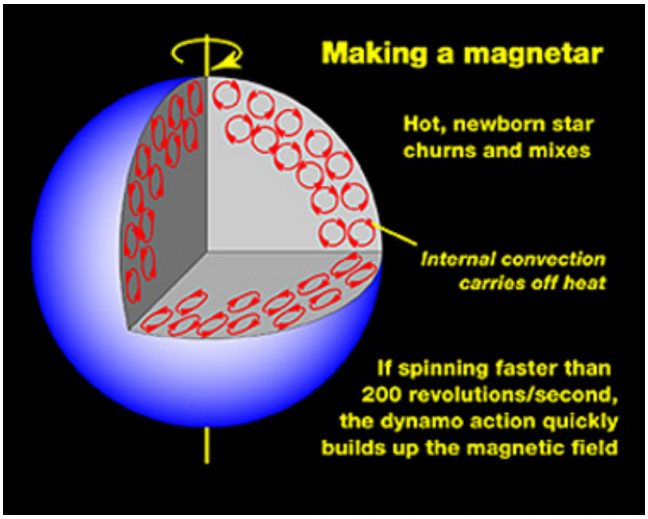


Figure 1.3: Schematic illustration of the dynamo mechanism in a rapidly spinning newborn neutron star Image source: Dave dooling, NASA Marshall Space Flight Center.

The surface heating and the slow cooling that follows can last from months to years, explaining why magnetars often show long-term decays after an outburst (Kaspi and Beloborodov 2017).

Another important feature of the Thompson–Duncan model is that movements in the crust can twist the star's external magnetic field. A twisted magnetosphere carries electric currents that interact with the X-ray photons coming from the surface, producing the characteristic non-thermal emission seen in many magnetars. As the twist slowly relaxes, the currents weaken and the X-ray brightness fades back toward a quieter state. Together, these ideas link the hidden internal magnetic field, the behaviour of the crust, and the X-ray emission that we observe. With this basic picture in place, we can now look at the observable characteristics of magnetars and then discuss the various transient behaviours, such as bursts, giant flares, and large outbursts, that arise from these internal processes.

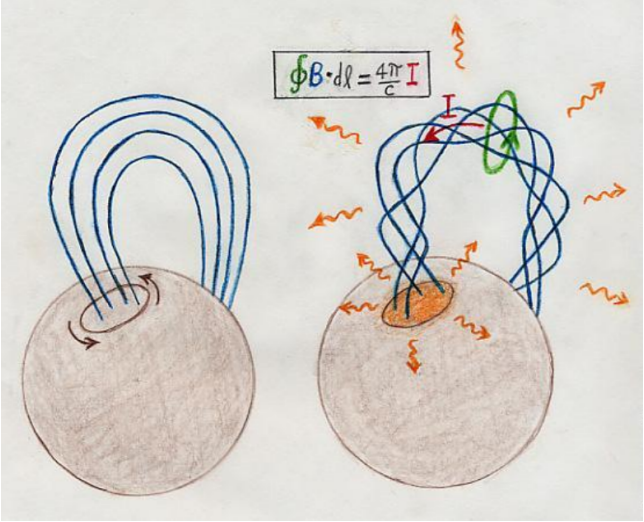


Figure 1.4: Schematic illustration of magnetar outburst initiation. Crustal motions twist the external magnetic field lines, storing energy in the magnetosphere. When the twist becomes unstable, the field releases energy through magnetospheric currents, heating the surface and producing enhanced X-ray emission. Image Source : https://ariccio.com/2013/06/08/magnetars-soft-gamma-repeaters-very-strong-magnetic-fields/

1.1.3 Basic observational properties

Magnetars form a rare and remarkable class of neutron stars distinguished by their strong magnetic fields. While thousands of neutron stars are known, only about thirty objects have been confirmed as magnetars to date. Their magnetic fields, among the strongest found in the Universe, can exceed 10^{14}–10^{15} G, far surpassing those of ordinary pulsars. Sources such as SGR 1806−20 and 1E 2259+586 have played an important role in establishing magnetars as a distinct population, showing that their behaviour is unlike that of typical rotation-powered pulsars.

Unlike millisecond radio pulsars, which spin hundreds of times per second, magnetars rotate very slowly, typically once every 2-12 seconds (Turolla, Zane, and Watts 2015). This slow rotation is understood to result from intense magnetic braking: the strong magnetic fields extract rotational energy efficiently, causing the star to spin down rapidly over time. Their spin-down rates are therefore much higher than those of ordinary pulsars, and independent measurements consistently point to magnetic field strengths in the 10^{14}–10^{15} G range.

One of the defining signatures of magnetars is that their persistent X-ray luminosity exceeds the energy available from their rotational spin-down alone (Kaspi and Beloborodov 2017). This simple but powerful observation demonstrates that magnetars cannot be powered primarily by rotation, as ordinary pulsars are. Instead, their emission is believed to be fueled by the decay and rearrangement of their strong magnetic fields, along with internal heating processes. This stored magnetic energy is what powers the dramatic and short-lived events seen from magnetars. These include sudden increases in X-ray brightness, brief bursts of radiation, and, in the most extreme cases, powerful giant flares such as those observed from SGR 1900+14 and SGR 1806−20. Such events make magnetars important objects for studying how matter behaves under extremely strong magnetic fields and intense gravity. Now let's look at the transient behaviour in magentars.

1.2 Transient behaviour in magnetars

Magnetar transient activity encompasses diverse features, including month-scale outbursts, short-duration X-ray flares, and rare but extremely intense giant flares.

Magnetars sometimes experience events called outbursts, where their X-ray brightness suddenly increases, by a factor of 10 to 1000, and can stay high for weeks, months, or even several years. During these times, their luminosities can reach upto 10^{36} erg s^{-1}. These events often bring noticeable changes in the star's behaviour, such as shifts in the pulse profile morphology, a harder X-ray spectrum, or abrupt variations in the spin rate called glitches. Outbursts are widely believed to occur when strong magnetic stresses inside the neutron star disturb the crust or twist the surrounding magnetic field, releasing stored magnetic energy that heats the surface and boosts the X-ray emission. Transient magnetars are especially known for how different they appear in their quiet and active states. In quiescence, they are very faint, with X-ray luminosities below 10^{33} erg s^{-1}. But during an outburst, their brightness can increase sharply. Examples such as SGR 0418+5729 and Swift J1822.3–1606 show that even magnetars with relatively low dipole magnetic fields can produce strong outbursts, which suggests they may have much stronger internal magnetic fields (Kaspi and Beloborodov 2017). These sources have helped us better understand how magnetic energy powers magnetar activity.

Short bursts are common events observed in magnetars, typically lasting from a few milliseconds to a few seconds and reaching luminosities up to 10^{36}–10^{43} erg s^{-1}. These bursts are believed to result from crustal fractures or magnetic reconnection in the magnetosphere triggered by magnetic stresses, which release Alfvén waves and accelerate particles, producing hard X-ray and γ-ray emission (Kaspi and Beloborodov 2017; Lyutikov 2003).

Giant flares (GFs) are the most energetic and rarest events observed from magnetars, releasing 10^{44}–10^{47} erg in hard X-rays and γ-rays within fractions of a second. These events are believed to arise from catastrophic magnetic reconnection or large-scale untwisting of the magnetosphere, possibly triggered by a crustal fracture due to extreme internal magnetic stresses (Kaspi and Beloborodov 2017). Such rare, extreme outbursts

provide direct evidence of the immense magnetic energy reservoirs in magnetars and the dynamic coupling between their crust and magnetosphere.

1.3 Timing properties of magnetars

Timing studies of magnetars provide important insights into their emission geometry and magnetospheric activity. Parameters such as Pulse profiles, Pulsed fraction (PF), Pulsed Count Rate(PCR) are essential for understanding how the radiation varies with rotation and evolves during different activity states, like bursts or outbursts.

1.3.1 Pulse Profile

The pulse profile shows how a magnetar's X-ray brightness changes as it rotates. It is made by folding the light curve using the star's spin period. These pulse profiles often change during and after an outburst, so they are useful for tracking how the magnetar evolves. Looking at features such as how many peaks there are, how they are shaped, and how strong they are helps us understand where the X-rays are coming from and how the magnetic field is arranged. In several magnetars, like XTE J1810–197 and SGR 1745–2900, such changes have been seen after outbursts (Bernardini et al. 2009). These variations may point to the appearance of new hot spots on the surface or changes in currents in the magnetosphere, giving important clues about how the magnetic field changes over time.

1.3.2 Pulsed fraction

The pulsed fraction provides a convenient measure of how strongly the observed X-ray emission varies as the neutron star rotates. In magnetars, this quantity often reflects the geometry of the emitting regions and how the surface or magnetospheric hotspots evolve following an outburst. For example, studies of sources such as XTE J1810–197 (Ibrahim et al. 2004; Alford and Halpern 2016) and 1E 1547.0−5408 (Bernardini et al. 2009) have shown that the pulsed fraction can change significantly as the surface cools or as the magnetosphere reorganizes, making it an important tracer of the underlying physical processes.

In practice, the pulsed fraction is computed from the pulse profile, which represents the distribution of photon counts as a function of ro-

tational phase. First, the average number of photons per phase bin is evaluated as

$$n_{\rm ave} = \frac{1}{m}\sum_{i=1}^{m} n_i,$$

where n_i is the number of photons in the $i^{\rm th}$ bin and m is the total number of bins. The variance of the profile is then calculated to quantify the level of modulation around this mean,

$$\sigma^2 = \frac{1}{m}\sum_{i=1}^{m} (n_i - n_{\rm ave})^2 .$$

Finally, the pulsed fraction is defined as the ratio of the root-mean-square variation to the mean count rate:

$$\mathrm{PF} = \frac{\sqrt{\sigma^2}}{n_{\rm ave}}. \tag{1.1}$$

This definition provides a straightforward way to compare pulse profile variability across different epochs or energy bands and is commonly used in studies of magnetar outbursts.

1.3.3 Fractional amplitude

Fractional amplitude is a timing parameter used to quantify the strength of rotational modulation relative to the mean emission level of a periodic source. It provides a direct measure of how strongly the observed flux is modulated as the star rotates. Unlike luminosity, which measures the total emitted energy, fractional amplitude specifically traces the relative contribution of periodic variability to the overall emission.

For complex pulse profiles, a single sinusoidal component is often insufficient to describe the full pulse morphology. In such cases, the pulse profile is more accurately represented using a Fourier decomposition, where the observed emission is expressed as the sum of multiple harmonic components:

$$P(\phi) = A_0 + \sum_{k=1}^{N} A_k \sin(2\pi k\phi + \phi_k), \tag{1.2}$$

where A_0 represents the mean emission level, A_k is the amplitude of the k-th harmonic, and ϕ_k is its corresponding phase offset. Each harmonic captures a different structural feature of the pulse profile, with the fundamental harmonic typically tracing the broad primary modulation, while higher-order harmonics describe additional complexity such as sharper peaks, asymmetries, or multiple substructures.

For such multi-harmonic profiles, the fractional amplitude of the k-th harmonic is defined as

$$f_k = \frac{A_k}{A_0} \tag{1.3}$$

which quantifies the contribution of that harmonic relative to the mean emission level. Physically, this allows us to determine how strongly each harmonic contributes to the overall pulse structure. Larger values of f_k indicate that a given harmonic plays a more significant role in shaping the pulse profile, while smaller values suggest weaker structural influence.

1.4 Why XTE J1810-197?

XTE J1810-197 is one of the most unique transient magnetars known. It is primarily known because of its transient nature and unique opportunity to study magnetar reactivation in real time. It was discovered in 2003 by the *RXTE* satellite and was the first magnetar ever to be detected as a radio pulsar. This discovery changed our understanding of neutron star magnetospheres, showing that magnetars are capable of producing radio emission, which was thought to happen only in conventional (rotation-powered) pulsars. Its transition from a bright, active X-ray and/or radio state to a quiescent state offers a rare opportunity to study magnetar broadband emission and activity over time.

Following the outburst in 2003, the X-ray brightness and surface temperature of XTE J1810−197 slowly decreased over the next few years, as shown by several XMM–Newton observations (Bernardini et al. 2009). Its X-ray spectrum was best described by three thermal components, meaning the star had a cool overall surface, possibly along with two much hotter spots created during the outburst. Around the same time, the radio emission disappeared in 2008, hinting at a possible link between the fading hotspot and the loss of radio pulses. By 2014, the magnetar seemed to reach a stable state with one persistent hotspot that was still brighter than what could be explained by its rotational energy alone (Alford and Halpern 2016). This suggested that the magnetic field continued releasing energy long after the outburst. Following this, the magnetar went into quiescence.

After staying quiet for more than ten years, XTE J1810−197 became active again in late 2018. This made it one of the few magnetars ever

seen to produce a second major outburst. Similar long-lasting behaviour has been observed in other transient magnetars, such as SGR 0418+5729 and Swift J1822.3−1606, whose X-ray emission also evolved slowly for many years. Because XTE J1810−197 has shown two outbursts, it offers a rare chance to compare how the magnetar changed between the two outbursts, especially its magnetic field, surface heating, and emission pattern. A detailed examination of the relationship between the radio emission phase and canonical X-ray emission phase, as well as the evolution of their correlation between the two outbursts, will yield critical insights into the evolutionary history of magnetars and pulsars.

1.4.1 Previous Studies on this magnetar post 2018

After the magnetar XTE J1810–197 became active again in 2018, only a few studies have examined its behaviour during this new outburst. (Gotthelf, Halpern, and Alford 2019) reported reactivation activity from SWIFT-XRT and NICER observations. They found that the X-ray brightness had increased, marking the start of a new outburst after many years of quiescence. They also noted that the X-ray spectrum during the 2018 event was softer than in the 2003 outburst, suggesting that the magnetar's magnetic field or surrounding environment may have changed over time.

Soon after, (Borghese et al. 2018) analysed early X-ray observations from 2018. Their results showed that the X-ray emission could be described by two heated regions on the neutron-star surface—one small and hot, and another larger and cooler. This behaviour is consistent with models of magnetar outbursts, where the crust is heated and electric currents form in the magnetosphere. They also suggested that some of the twisted magnetic field lines may have begun to relax, which could explain the gradual changes in both the spectral and timing properties.

In addition, (Güver et al. 2019) used NICER to monitor the source during the initial stages of the 2018 outburst. Thanks to NICER's high timing resolution, they were able to detect rapid changes in the pulse shape and pulsed fraction. These observations indicate that the size and location of the X-ray emitting regions were evolving soon after the reactivation. Their findings further support the important role that magnetospheric processes play in shaping the observed pulse profile during magnetar outbursts.

Together, these post-2018 studies provide important clues about how

XTE J1810–197 behaves after becoming active again. The observed changes in spectral hardness, pulse morphology, and radio properties support models in which magnetic field decay, crustal motion, and magnetospheric twists act together to power the magnetar's emission. However, many questions remain—including what triggers such reactivation and how the surface and magnetosphere interact over long timescales. These open questions motivate the detailed investigation presented in this thesis.

1.5 Research objective

The primary objective of this project is to carry out a detailed X-ray analysis of the transient magnetar XTE J1810–197 using *XMM-Newton* observations obtained after its 2018 outburst. This outburst marks a rare reactivation event, making XTE J1810–197 one of the few magnetars observed to undergo a second major outburst following a long period of quiescence since 2003. Studying this event provides a unique opportunity to explore the renewed magnetar activity, investigate the physical mechanisms driving the reactivation, and understand the evolution of its emission and magnetic field configuration over time.

The specific objectives of this work are as follows:

1. **Timing Analysis:** To study the timing properties by determining the spin frequency and examining the evolution of its pulse profile, pulsed fraction (PF), and fractional amplitude (FA). This analysis will help us understand the emission geometry, magnetospheric dynamics, and possible changes in the surface emission regions.

2. **Energy-Resolved Studies:** To study the timing properties in different energy bands in order to identify any energy-dependent variations in pulse shape, amplitude, and emission components. This will help identify the dominant emission processes in different energy ranges and provide insights into the connection between surface and magnetospheric emission zones.

3. **Spectral Analysis:** To perform spectral analysis on the *XMM-Newton* data to model the thermal and non-thermal components of the X-ray emission. This will help investigate the cooling behaviour and study the evolution of the surface hot spots.

4. **Comparison with 2003 Results:** By comparing the post-2018 results with those from the 2003 outburst, we aim to identify similarities and differences in the magnetar's radiative and magnetic evolution. Here, we also plan to investigate the radio and X-ray correlated behaviour across the two outbursts. This comparison will also help us understand the conditions leading to the source's radio-loud phase and the long-term evolution of its magnetic field.

5. **Physical Interpretation and Correlation:** To interpret the observed spectral and timing evolution in the context of magnetothermal and magnetospheric models, and correlate the results with multi-wavelength findings where available. This will help build a more comprehensive understanding of the energy release, magnetic field decay, and emission mechanisms governing the post-outburst behaviour of transient magnetars.

Chapter 2

Instrument

2.1 XMM-NEWTON Telescope

The X-ray Multi-Mirror Mission (XMM-Newton) is one of the cornerstone observatories of the European Space Agency, launched in December 1999 to study high-energy astrophysical processes (Jansen et al. 2001).The observatory carries two types of telescopes: three co-aligned Wolter type-I X-ray telescopes, each equipped with dedicated focal-plane detectors. It also carries a 30-cm Optical/UV Monitor (OM) that uses a microchannel-plate–intensified CCD detector. This configuration allows XMM-Newton to provide simultaneous coverage in both the X-ray and optical/UV bands. (XMM-Newton Science Operations Centre 2022).

In this chapter, we will provide a brief overview of the XMM-Newton observatory, summarizing its basic characteristics, spacecraft design, telescope optics, and the key scientific instruments relevant to our analysis.

2.1.1 Basic Characteristics

Some of the most important characteristics is summarised in the table below

Table 2.1: Summary of instrument characteristics of XMM-Newton (XMM-Newton Science Operations Centre 2022).

Instrument	EPIC pn
Bandpass	0.15–12 keV
Orbital target vis.	5–135 ks
Sensitivity	$\sim 10^{-14}$
Field of view (FOV)	30′
PSF (FWHM/HEW)	6″/15″
Pixel size	150 μm (4.1″)
Timing resolution	0.03 ms
Spectral resolution	~80 eV

2.1.2 Spacecraft overview

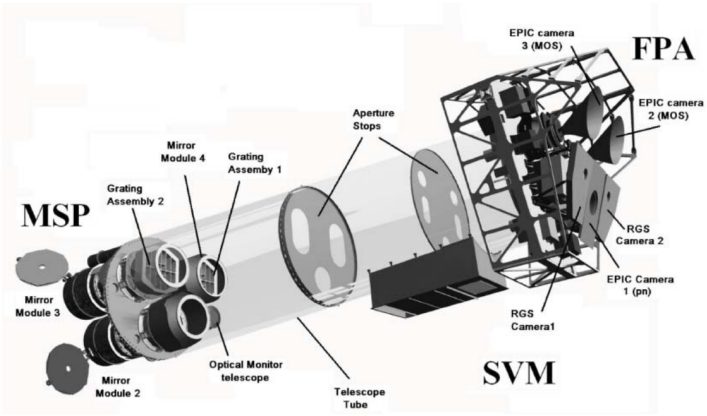


Figure 2.1: View of the XMM-NEWTON spacecraft subsystems. Image credit : Jansen et al. 2001

The XMM-Newton spacecraft is built around four major structural elements that support its scientific payload. At the focal-plane end, the Focal Plane Assembly (FPA) has the primary detectors: the EPIC pn and EPIC MOS imaging cameras, together with the two RGS readout systems. These instruments are mounted on a thermally controlled platform and are equipped with passive radiators to keep the CCDs at the low temperatures required for optimal performance. At the opposite end,

the Mirror Support Platform (MSP) carries three X-ray mirror modules, the Optical/UV Monitor (OM), and two star-trackers used for precise attitude control. The FPA and MSP are connected by a long carbon-fibre telescope tube, which maintains the 7.5-m focal length while providing mechanical stability.

Supporting these structures is the Service Module (SVM), which contains the spacecraft's power, communication, thermal, and attitude control subsystems, along with the solar arrays and the Sun shield. The spacecraft has a launch mass of about 3800 kg and a total length of roughly 10 meters. XMM-Newton operates in a highly elliptical 48-hour orbit—with an apogee of 114,000 km, allowing long, uninterrupted science exposures with minimal Earth occultation. The spacecraft transmits data continuously to Earth through ESA's ground stations (Mereghetti 2008).

2.1.3 Scientific Instruments

The main payload consists of the European Photon Imaging Cameras (EPIC), which This provides imaging an spectral resolution. Reflection Grating Spectrometers (RGS), which delivers high-resolution soft X-ray spectroscopy. In addition to the X-ray instruments, the Optical/UV Monitor (OM) enables multiwavelength observations in the optical and ultraviolet bands. In our analysis, we have used the data from EPIC PN detector.

The EPIC pn camera is one of the primary X-ray imaging detectors on board XMM-Newton, designed for high time resolution and high sensitivity. It uses a large-format silicon CCD array arranged in a back-illuminated configuration as given in Figure 2.2. This gives excellent quantum efficiency across the 0.15–12 keV energy band. The pn detector provides the highest effective area among the EPIC cameras and supports several readout modes. This includes Full Frame, Small Window. Timing Mode allows users to optimize observations for spectroscopy, imaging, or submillisecond timing studies of bright sources shown in figure **??**. Its resolution can reach 30 microseconds, making it ideal for studying pulsars, magnetars, and other rapidly varying X-ray emitters. The EPIC pn camera achieves a spectral resolution of about 80 eV at 1 keV and offers a wide field of view of approximately 30 arcminutes (XMM-Newton Science Operations Centre 2022).

The EPIC MOS detectors consist of two front-illuminated CCD arrays placed at the focal planes of the other two XMM-Newton telescopes. Like the pn camera, the MOS instruments operate over the 0.15–12 keV band, but they are optimized for high-quality imaging rather than high-speed timing. Each MOS camera contains seven CCDs arranged in a mosaic, providing uniform spatial coverage and a field of view comparable to the pn detector. The MOS CCDs offer good spectral resolution (about 70 eV at 1 keV) and support several observing modes, including Full Frame, Large Window, and Small Window configurations. Although their timing capabilities are more limited than the pn camera, the MOS detectors have lower background noise and excel in imaging faint or extended sources. Their stable performance and redundancy make them essential components of the EPIC system's overall scientific capability (XMM-Newton Science Operations Centre 2022).

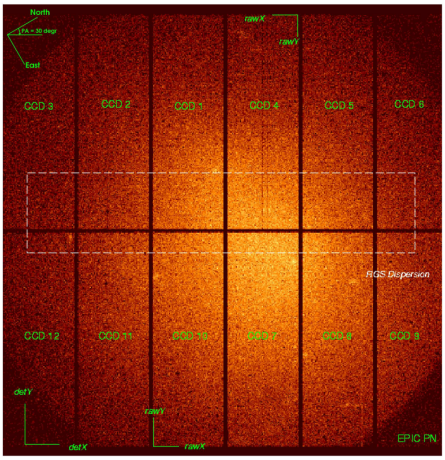


Figure 2.2: The EPIC pn camera layout as displayed in SAS, showing the orientation of the RAWX/RAWY and DETX/DETY axes and their alignment with the RGS dispersion direction. Image credit : XMM-Newton Science Operations Centre 2022

2.1.4 Data archival and Download

All XMM-Newton datasets used in this work were taken from the XMM-Newton Science Archive (XSA). The archive provides access to all public observations, along with associated calibration files, housekeeping data, and processing logs. For each observation of XTE J1810–197, the raw Observation Data Files (ODFs) were downloaded directly from XSA using the web interface. Each dataset was checked for completeness, data integrity, and compatibility with the required SAS version before proceeding with reduction.

Table 2.2: Summary of downloaded XMM-Newton datasets.

ObsID	Date	Status
0804590701	2018-03-03	visible
0784303101	2019-03-04	visible
0784303301	2019-09-22	not visible
0784303201	2019-09-22	visible
0913991301	2022-09-17	visible
0913991401	2022-09-17	not visible
0921410201	2023-09-24	visible
0921410301	2024-04-07	visible

Table 2.2 summarises all downloaded observations relevant to this study. The "visible" and "not visible" tags indicate whether the source appeared within the EPIC field of view after preliminary inspection of the raw event lists and attitude files. Observations marked as "not visible" were excluded from further analysis due to source position falling outside the detector area. The remaining datasets form the basis of all timing and spectral analyses presented in the subsequent sections of this thesis. A detailed description of the data reduction, cleaning, and processing steps carried out using SAS is provided in Appendix A.

2.2 Neil Gehrels Swift Observatory

The Neil Gehrels Swift Observatory is a space-based multi-wavelength telescope launched in 2004 with the primary goal of detecting and studying gamma-ray bursts (GRBs) and their afterglows. Over time, it has become a highly versatile observatory for investigating a wide range of transient and variable astrophysical sources, including magnetars, X-ray binaries, and active galactic nuclei.

A key strength of Swift is its rapid response capability and flexible scheduling, which allow it to observe transient events shortly after detection and to monitor sources over long timescales. This makes it particularly well suited for studying the temporal evolution of sources following outbursts.

Swift carries three co-aligned instruments that together cover a broad energy range, enabling simultaneous or complementary observations across multiple wavelengths. These instruments are the Burst Alert Telescope (BAT), the X-ray Telescope (XRT), and the Ultraviolet/Optical Telescope (UVOT). In this work, we primarily make use of data from the X-ray Telescope (XRT), which provides imaging, spectral, and timing information in the soft X-ray band.

2.2.1 Instrument Overview

Swift carries three co-aligned instruments that together enable observations across a wide range of energies.

Burst Alert Telescope (BAT): The BAT is a wide-field, coded-mask gamma-ray detector operating in the 15–150 keV energy range. It is primarily designed to detect gamma-ray bursts (GRBs) and other high-energy transients. Upon detection, the BAT determines the source position with an accuracy of a few arcminutes and triggers an autonomous slew of the spacecraft to rapidly point the narrow-field instruments toward the source.

X-ray Telescope (XRT): The XRT is a narrow-field X-ray telescope operating in the 0.2–10 keV energy range. It provides imaging, spectroscopy, and timing capabilities, and can localize sources with an accuracy of ∼3–5 arcseconds. With additional astrometric correction using UVOT data, the positional uncertainty can be improved to about 1.4 arcseconds (90% confidence level), Swift Science Center 2015.

Ultraviolet/Optical Telescope (UVOT): The UVOT is a 30 cm aperture ultraviolet/optical telescope sensitive to wavelengths in the range 1600–6000 Å. It provides precise source localization (up to ~0.5 arcseconds), generates finding charts, and performs broad-band imaging of transient sources such as GRB afterglows. In addition, UVOT is capable of obtaining low-resolution spectra using its grism modes in the 1700–2900 Å range Swift Science Center 2015.

In this work, we primarily use data from the X-ray Telescope (XRT), as it is best suited for studying the long-term X-ray evolution of the source. Unlike XMM-Newton, which offers high sensitivity but is limited to a few pointed observations, Swift enables dense temporal coverage over extended periods. This makes it especially useful for tracking the evolution of the source following the outburst, including changes in flux, spectral properties, and timing behaviour Swift Science Center 2015.

In this study, Swift observations complement XMM-Newton by filling the gaps between high-quality observations and allowing us to construct a more continuous picture of the source evolution over time.

2.2.2 Basic characteristics of XRT

The main characteristics of the Swift XRT instrument are summarized in Table 2.3 from Swift Science Center 2015.

Table 2.3: Key parameters of the Swift XRT instrument.

Parameter	Value
Energy Range	0.2–10 keV
Telescope	Wolter I
Detector	E2V CCD-22
Effective Area	120 cm^2 at 1.5 keV
Detector Operation	Photon-counting, imaging, and timing
Field of View	23.6×23.6 arcmin
Detector Elements	600×602 pixels
Pixel Scale	2.36 arcsec
Telescope PSF	18 arcsec (HPD) at 1.5 keV
Sensitivity	22 arcsec (HPD) at 8.1 keV

2.2.3 Data Archive and Acquisition

All Swift-XRT data used in this work were obtained from the publicly available *HEASARC* (High Energy Astrophysics Science Archive Research Center) archive maintained by NASA. The archive provides fully processed and calibrated datasets, along with the necessary auxiliary files required for scientific analysis.

The observations were selected to cover the long-term evolution of the source following its outburst, spanning the period from 2019 to 2025. These datasets were retrieved using the online data access tools provided by HEASARC, based on the source coordinates and observation identifiers (ObsIDs).

For each observation, the standard data products include event files, exposure maps, and auxiliary calibration files. These data were subsequently processed using the `HEASoft` software package, along with the latest calibration database (CALDB), following standard Swift-XRT data reduction procedures.

Table 2.4: Log of observations with ObsID and observation dates.

ObsID	Date
00031335006	08/02/2019
00031335007	15/02/2019
00031335008	22/02/2019
00031335009	02/03/2019
00031335010	08/03/2019
00031335011	13/03/2019
00031335012	15/03/2019
00031335013	22/03/2019
00031335014	29/03/2019
00031335015	05/04/2019
00031335016	12/04/2019
00031335017	17/04/2019
00031335018	19/04/2019
00031335021	03/05/2019
00031335023	17/05/2019
00031335024	24/05/2019

ObsID	Date
00031335025	30/05/2019
00031335026	01/06/2019
00031335027	09/06/2019
00031335028	25/06/2019
00031335029	26/06/2019
00031335031	30/06/2019
00031335032	03/07/2019
00031335033	09/07/2019
00031335034	12/07/2019
00031335035	22/07/2019
00031335036	25/07/2019
00031335038	13/08/2019
00031335039	23/08/2019
00031335040	31/08/2019
00031335041	05/09/2019
00031335042	10/09/2019

ObsID	Date
00031335043	17/09/2019
00031335044	25/09/2019
00031335045	06/10/2019
00031335046	15/10/2019
00031335047	25/10/2019
00031335048	18/03/2020
00031335049	20/06/2020
00031335050	21/06/2020
00031335051	26/06/2020
00031335052	28/06/2020
00031335053	02/07/2020
00031335054	14/07/2020
00031335055	15/07/2020
00031335056	28/07/2020
00031335057	11/08/2020
00031335058	25/08/2020
00031335059	11/02/2021
03110871001	12/02/2021
00031335060	12/02/2021
00031335061	18/02/2021
00031335062	11/03/2021
00031335063	11/04/2021
00031335064	11/05/2021
03110991001	12/05/2021
00031335067	17/06/2021
00031335068	11/07/2021
00031335069	11/08/2021
00031335070	11/09/2021
00031335071	13/10/2021
00031335072	06/11/2021
00014973002	10/03/2022
00014973003	10/04/2022
00014973004	10/05/2022
00014973005	10/06/2022

ObsID	Date
00014973006	10/07/2022
00014973007	10/08/2022
00014973008	10/09/2022
00014973009	11/09/2022
00014973011	15/10/2022
00014973013	14/02/2023
00014973014	13/03/2023
00014973015	27/03/2023
00014973016	14/04/2023
00014973017	14/05/2023
00014973018	14/06/2023
00014973019	14/07/2023
00014973020	14/08/2023
00014973021	14/09/2023
00014973022	14/10/2023
00016431001	11/02/2024
00016431002	11/03/2024
00016431003	11/04/2024
00016431004	12/04/2024
00016431005	16/04/2024
00016431006	20/04/2024
00016431007	11/05/2024
00016431008	11/06/2024
00016431009	11/07/2024
00016431011	11/08/2024
00016431012	11/10/2024
00016431014	10/02/2025
00016431015	13/02/2025
00016431016	10/04/2025
00016431017	10/06/2025
00016431019	10/08/2025
00016431020	13/08/2025

Chapter 3

Timing Properties

Temporal properties, such as pulse profiles and spin variations, offer a direct way to probe the behavior of XTE J1810−197. The pulsed emission carries information about both the rotation of the neutron star and the structure of its emitting regions. During outburst phases, magnetars are known to exhibit significant changes in their spin frequency, pulse shape, and modulation amplitude. By tracking these variations over time, we can follow the rotational evolution of the source, study how the pulse profile changes, and gain insight into the interplay between the neutron star surface and its magnetosphere.

In this chapter, we present a detailed X-ray timing analysis following its 2018 reactivation. We begin by generating light curves to examine long-term intensity variations. This is followed by a detailed search for periodicity to estimate the spin frequency. Then, the resulting pulse profiles are used to derive the fractional amplitude, pulsed fraction, and total fractional amplitude, which allows us to investigate how the degree of modulation evolves with time and energy.

3.1 Light Curves

3.1.1 Data Reduction

The raw data for XTE J1810−197 were obtained from the *XMM-Newton* Science Archive in the form of Observation Data Files (ODFs). These files contain the original, unprocessed detector data and must be calibrated before they can be used for scientific analysis. To achieve this, we used the *Science Analysis Software* (SAS), which converts the raw data into calibrated event files.

The observations include data from the EPIC detectors (PN and MOS1). In this work, we focus on the PN detector because of its superior timing resolution, which is better suited for studying pulsations. The calibration process involves generating the necessary calibration and summary files. These files allow the raw data to be transformed into a clean list of detected X-ray photons, including their arrival times and energies. These calibrated event files form the basis for all subsequent analysis. Further details of this process are provided in Appendix A.

Once the calibrated event file is obtained, we first examine the data for contamination from high-energy particle flares, which can increase the observed count rate. These flares are caused by charged particles, primarily from solar activity and the Earth's magnetosphere, interacting with the detector and producing spurious counts. To identify such intervals, a preliminary light curve is created and a sigma-clipping method is applied to determine a threshold above which the background is considered contaminated. The time intervals that satisfy this condition are then used to define Good Time Intervals (GTIs), which specify the periods of reliable data. These GTIs are applied to filter the event list, ensuring that only uncontaminated data is retained.

The filtered event list is then used to generate an X-ray image, which is inspected using `DS9`. Based on this image, regions corresponding to the source and background are selected. The source region contains photons from the target, while the background region provides an estimate of unrelated noise in the data.

To ensure accurate timing, the photon arrival times are corrected to the Solar System barycenter. This correction accounts for the motion of both the satellite and the Earth, effectively transforming the arrival times to those that would be measured by an observer at rest with respect

to the center of mass of the Solar System. This step is essential for precise timing analysis, as it removes Doppler shifts and time delays that would otherwise distort periodic signals such as pulsations. Light curves are then extracted for both the source and background regions. The background contribution is subtracted from the source, and the resulting light curve is corrected for instrumental effects such as dead time and exposure variations. The final, cleaned light curves represent the intrinsic X-ray variability of the source and are used for further timing analysis. To highlight long-term trends, we present all six XMM-Newton observations and a subset of Swift observations sampled at approximately yearly intervals. The resulting light curves are presented in the following section.

3.1.2 Light Curve plots

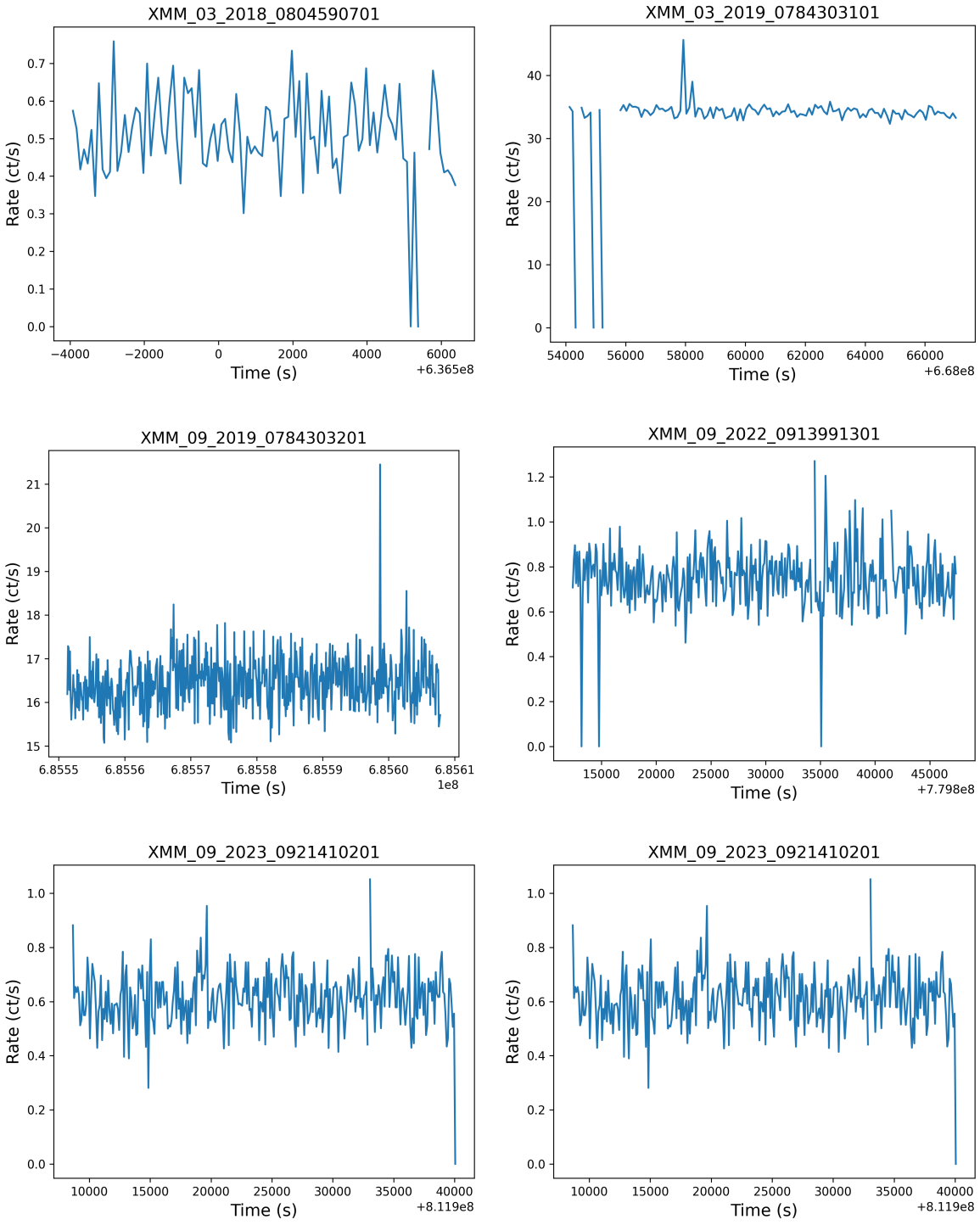


Figure 3.1: Light curve plots for all 6 XMM-NEWTON observations.

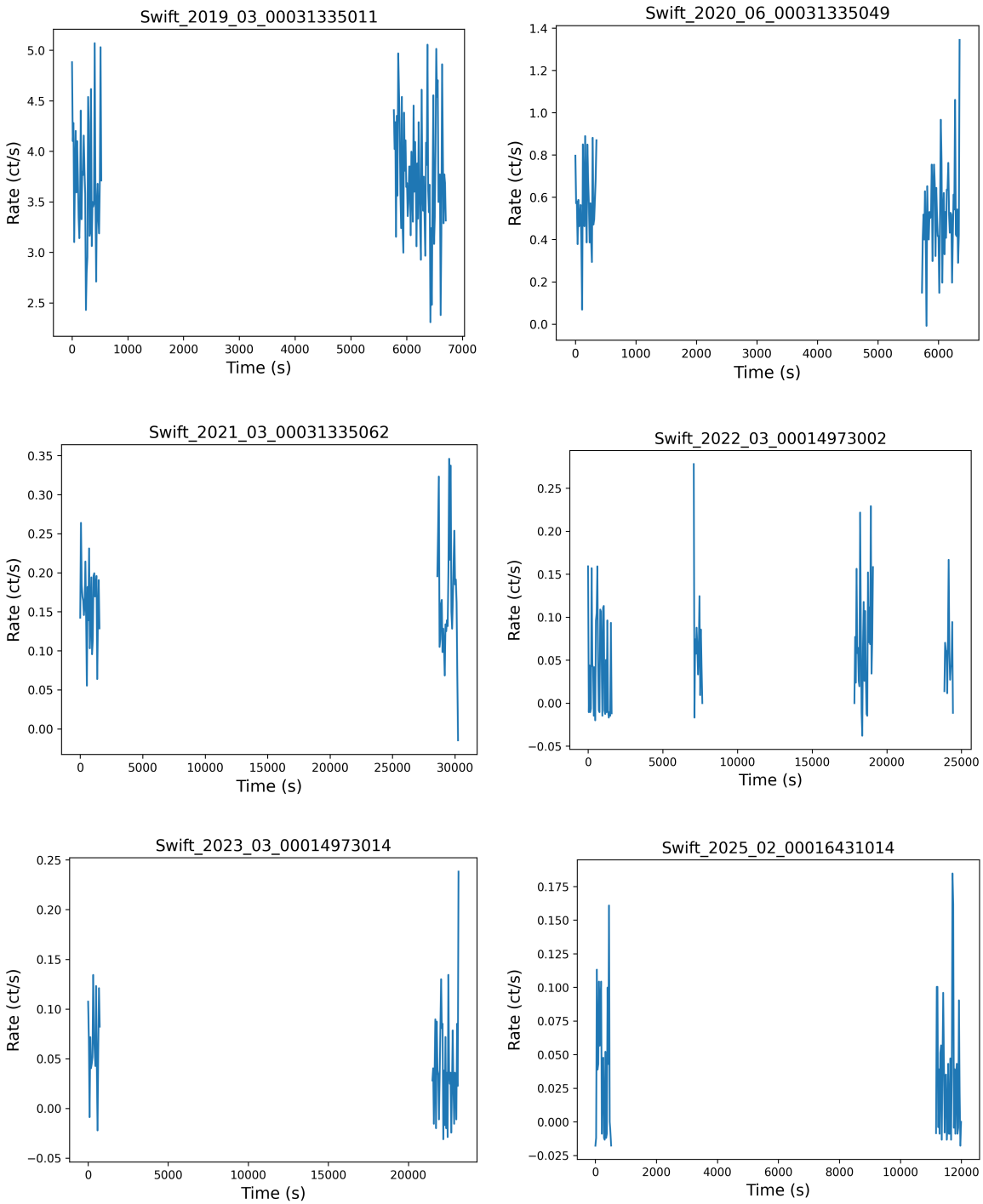


Figure 3.2: Light curve plots from selected Swift observations, sampled at approximately yearly intervals from the full dataset.

3.1.3 Post-outburst X-ray Flux Evolution

To investigate the long-term evolution of the source following the 2018 outburst, we constructed the X-ray light curve using *Swift-XRT* observations spanning multiple years. The background-subtracted count rate was extracted in the 0.3–10 keV energy range for all available observations.

The temporal evolution of the count rate is shown in Figure 3.3. The vertical dashed line marks the epoch of the 2018 outburst. Immediately after the outburst, the source exhibits a high count rate, which subsequently decreases rapidly over time.

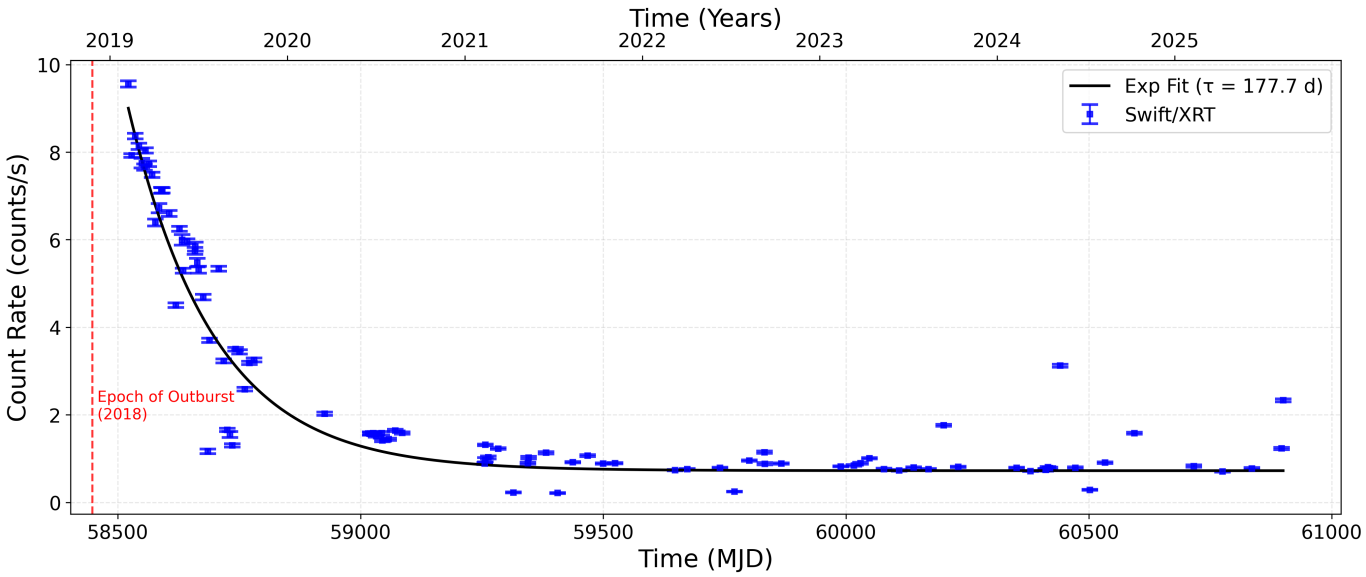


Figure 3.3: *Swift*-XRT count rate evolution of the source in the 0.3–10 keV band. The red dashed line marks the epoch of the 2018 outburst. The black curve represents the best-fit exponential decay model.

The decay of the count rate is well described by an exponential function of the form:

$$R(t) = R_0 e^{-t/\tau} + R_q \tag{3.1}$$

where R_0 represents the initial excess emission above the quiescent level, τ is the characteristic decay timescale, and R_q denotes the quiescent count rate.

From the light curves figure 3.1, figure 3.2 and fibure 3.3, we infer the following:

- **Long-term Outburst and Decay:** The light curves from *XMM-Newton* show a sharp increase in count rate after 2018. This indicates a major outburst between 2018 and 2019, with the flux rising by nearly two orders of magnitude. This is followed by a steady decline from 2019 to 2025 from the *Swift XRT*, consistent with post-outburst decay. Such behavior suggests cooling of the neutron star surface and gradual untwisting of the magnetosphere as the source returns to quiescence.

- **Short-timescale Variability:** Significant fluctuations and spikes are present across all epochs, indicating ongoing activity during the decay phase. Upward spikes likely arise from magnetospheric processes such as field line twisting and magnetic reconnection, which enhance X-ray emission. This persistent variability suggests that the source undergoes a gradual and dynamic relaxation rather than an abrupt transition to quiescence.

- **Post-outburst Flux Decay:** The X-ray count rate from the figure 3.3 exhibits a clear exponential decline following the 2018 outburst, characterized by a decay timescale of $\tau \sim 177$ days. This behavior indicates a gradual relaxation of the source after the outburst, likely driven by thermal cooling of the neutron star crust along with a progressive untwisting of the magnetosphere. This suggests that the magnetar is transitioning towards a quiescent emission state.

To further investigate the nature of the observed variability, we now examine the periodic modulations associated with the neutron star's rotation.

3.2 Estimation of Spin frequency and Pulse Profile plot

The spin frequency reflects how fast the magnetar rotates and is central to understanding its rotational evolution and magnetic activity. Changes in this frequency can provide important clues about variations in the external torque, which may arise from magnetic field reconfiguration or enhanced particle outflows. To estimate the spin frequency, we use timing analysis techniques that search for periodic modulations in the X-ray emission, produced as the emission beam sweeps across our line of sight. In the following sections, we describe the methods used to extract and model these periodic signals, starting with the construction and fitting of pulse profiles.

3.2.1 Construction of Background-Subtracted Pulse Profiles from XMM-Newton Observations

As mentioned in Chapter 1, pulse profiles capture how the observed emission from the source changes over its rotation. They are constructed by folding the barycenter-corrected photon arrival times using the best-fit spin period. However, the resulting folded profile includes not only the source emission but also contributions from the diffuse background. For faint or moderately bright X-ray pulsars and magnetars, the background level can be comparable to the off-pulse emission. This can lead to an underestimation of the pulsed fraction and may distort the intrinsic shape of the pulse profile. For this reason, background subtraction is necessary to recover the true rotational signal.

To obtain a background-subtracted pulse profile, we first estimate the background counts using an off-source region. This estimated background is then subtracted from each phase bin of the folded light curve, leaving a profile that reflects only the source emission. The subtraction is carried out in count space, with statistical uncertainties properly propagated to maintain the correct error distribution across the phase bins.

Pulse Profile fitting

By folding the observed photon arrival times with a trial frequency, one obtains a pulse profile. A comparison of this profile with a model helps us estimate the spin frequency.

First, a trial frequency is chosen. Let t_i denote the photon arrival times after applying barycentric correction. The rotational phase corresponding to each photon is then computed as

$$\phi_i = [\nu\,(t_i - t_0)] \bmod 1, \tag{3.2}$$

where ν is the trial frequency and t_0 is a chosen reference epoch. Finally, the photons are grouped into phase bins to construct a histogram of counts versus phase, which represents the pulse profile. This process is called folding of the photon arrival times. This is done over a range of trial frequencies to estimate the best frequency.

The observed profile $P(\phi)$ can be modelled as a sum of Fourier harmonics:

$$P(\phi) = A_0 + \sum_{k=1}^{N} A_k \sin\left(2\pi k\phi + \varphi_k\right), \tag{3.3}$$

where A_k and φ_k represent the amplitude and phase of the k-th harmonic. The fitting is performed by minimising the chi-square statistic between the observed and model profiles:

$$\chi^2(\nu) = \sum_{j=1}^{M} \frac{\left[P_{\rm obs}(\phi_j) - P_{\rm model}(\phi_j;\nu)\right]^2}{\sigma_j^2}. \tag{3.4}$$

Methodology

The first step in determining the spin frequency is to define a suitable range of trial frequencies around the expected value. For our source, with a spin period of $\sim$ 5.54 s, we scanned a narrow frequency range centered on the known pulsation frequency, corresponding approximately to periods between 5.44 s and 5.64 s. This range was chosen to ensure that the true frequency lies within the search window while avoiding unnecessary computational overhead.

The step size in frequency was selected based on the Fourier frequency resolution, which depends on the duration of each observation. For the longer *XMM-Newton* observations, a finer resolution of $\sim 10^{-5}$ Hz was adopted, while for the shorter *Swift* observations, a coarser resolution of $\sim 10^{-4}$ Hz was sufficient.

For each trial frequency, the barycenter-corrected photon arrival times were folded to compute pulse phases, and the resulting profiles were modelled using a single-harmonic sinusoidal fit. The fractional amplitude was then evaluated for each trial frequency and plotted as a function of frequency. The frequency corresponding to the maximum fractional amplitude was identified as the best estimate of the true pulsation frequency, as this is where the photon phases align most coherently, producing the strongest modulation. In contrast, folding at an incorrect frequency leads to phase smearing and a reduction in the observed modulation amplitude.

To illustrate this procedure, we present an example from the *XMM-Newton* observation with ObsID 0804590701. Figure 3.4 shows the fractional amplitude (ρ_0) as a function of trial frequency, exhibiting a clear and well-defined peak corresponding to the optimal spin frequency.

For this observation, the exposure time is $T = 10382$ s, which sets the Fourier frequency resolution as $\delta\nu \sim 1/T \approx 9.6 \times 10^{-5}$ Hz. This provides an estimate of the characteristic uncertainty in the measured spin frequency. Accordingly, the best-fit frequency is determined to be $\nu_{\rm best} = 0.18046 \pm 0.00009$ Hz.

Using this best-fit frequency, the barycenter-corrected event data were folded to construct the corresponding pulse profile. The resulting profile was then modelled using sinusoidal functions with multiple harmonics ($n = 1, 2, 3, 4$), as shown in Figure 3.5. The single-harmonic model captures the fundamental periodicity of the signal, while the inclusion of higher harmonics progressively improves the fit by accounting for finer pulse structure.

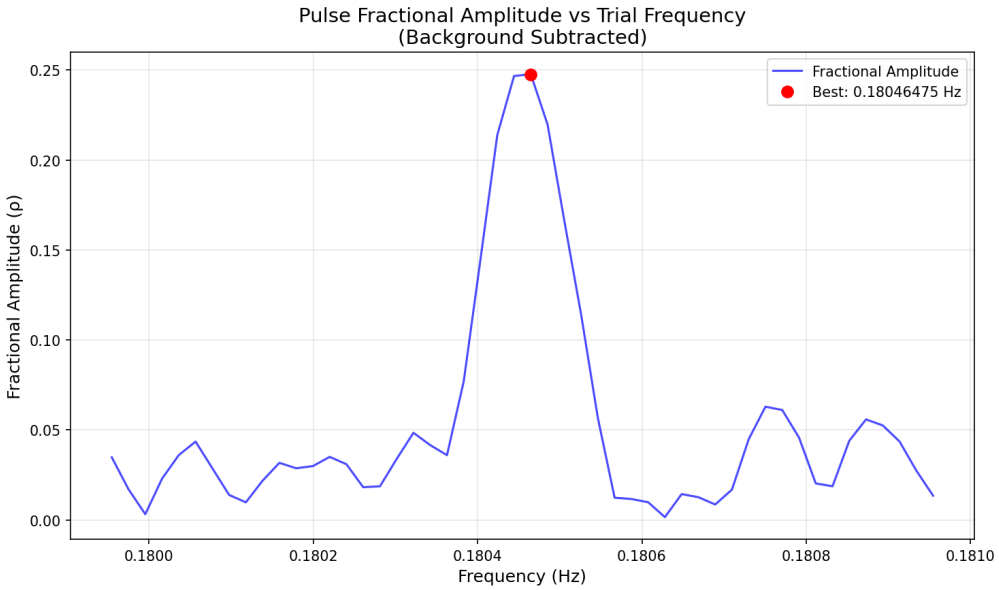


Figure 3.4: Frequency corresponding to maximum fractional amplitude for ObsID 0804590701. $f = 0.18046\,\text{Hz}$

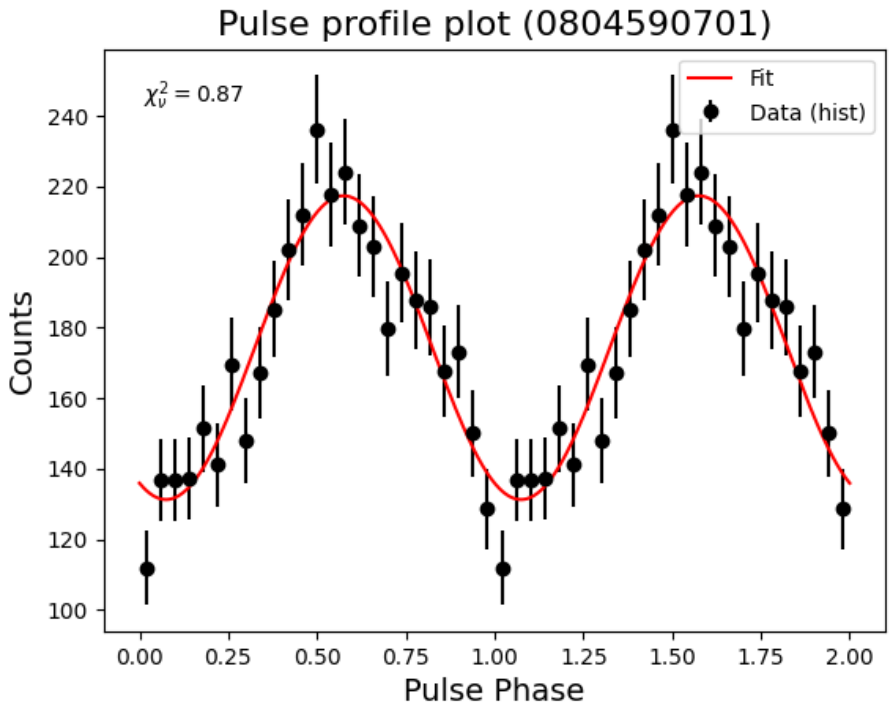


Figure 3.5: Pulse profile corresponding to the best-fit spin frequency $f = 0.18046\,\text{Hz}$ for ObsID 0804590701, along with the harmonic fit.

3.2.2 Temporal Evolution of Pulse Profiles from XMM-Newton Observations

The same analysis procedure described above was applied to the remaining five *XMM-Newton* observations. The resulting pulse profiles for all observations are presented below.

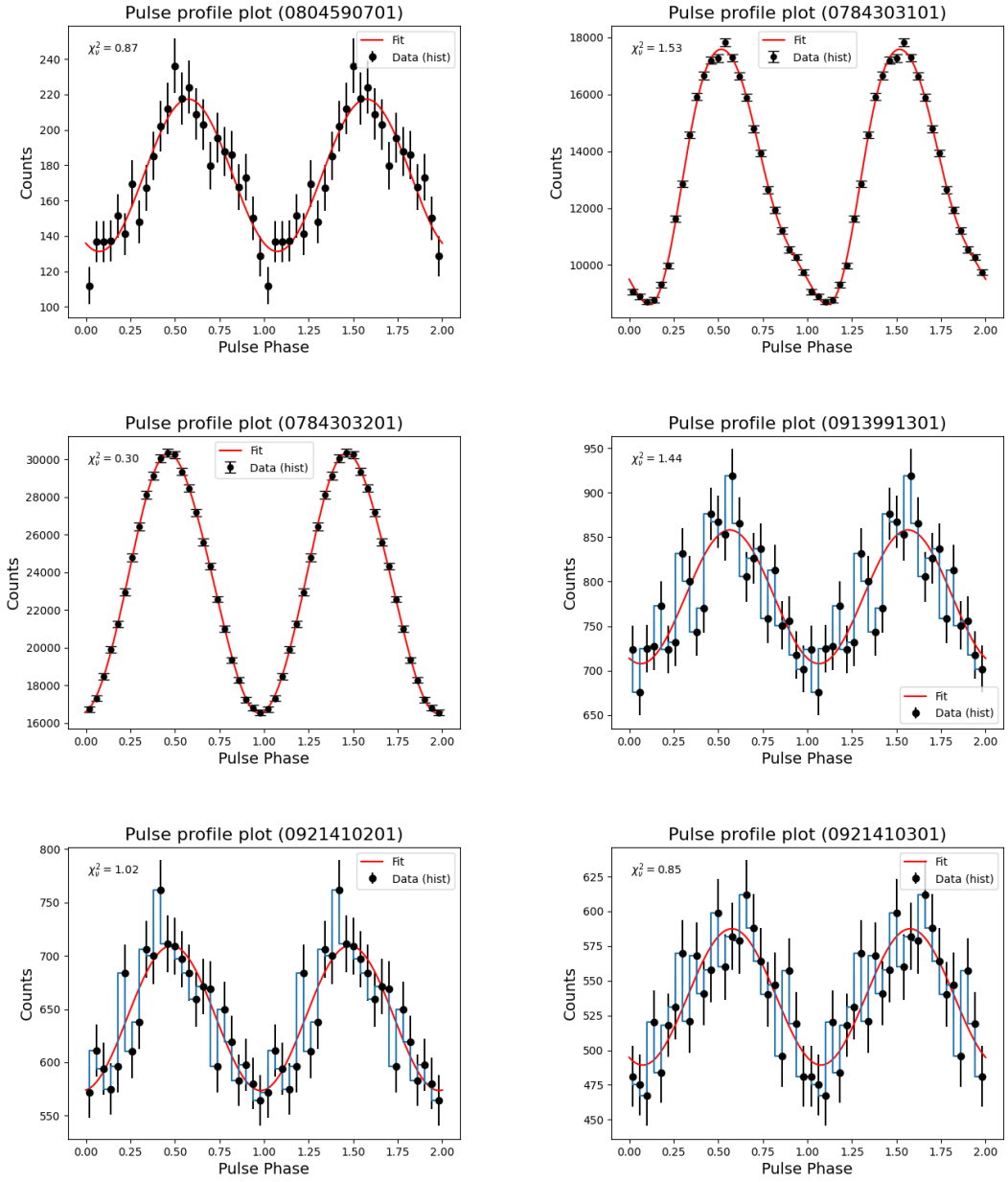


Figure 3.6: Best pulse profile fits for six observations (XMM-Newton). From left to right and top to bottom, (a) 0804590701 (03-03-2018), (b) 0784303101 (04-03-2019), (c) 0784303201 (22-09-2019), (d) 0913991301 (17-09-2022), (e) 0921410201 (24-09-2023), and (f) 0921410301 (07-04-2024).

3.2.3 Construction of Background-Subtracted Pulse Profiles from *Swift*-XRT Observations

Given the large number of *Swift* observations spanning multiple epochs, a representative subset of six datasets was selected for detailed pulse profile analysis. These datasets were chosen to sample different stages of the source evolution, including early post-outburst phases and later stages during the decay. In particular, the observations were selected such that they are approximately one year apart, enabling a systematic tracking of the long-term evolution of the pulse profile. The selection was further guided by data quality considerations, ensuring sufficient counts for reliable timing analysis.

The *Swift XRT* data were processed using the HEASoft software package following standard procedures. The raw data were reprocessed using the `xrtpipeline` task to generate cleaned and calibrated event files, applying standard screening criteria and producing exposure maps. Barycentric correction was then applied using the `barycorr` tool to account for the motion of the satellite and Earth, ensuring accurate timing analysis in the Solar System barycentric frame.

Source and background regions were defined using `ds9`. For Photon Counting (PC) mode data, a circular region centered on the source position was used to extract source events, while an annular region away from the source was selected for background estimation. For Window Timing (WT) mode, appropriate one-dimensional regions were chosen. In cases where pile-up was suspected (count rates exceeding ~0.6 cts s^{-1} in PC mode), corrections were applied by excluding the central region of the source.

Light curves and event files were extracted using `xrtproducts`, and background subtraction was verified using `lcmath`.

The cleaned and barycenter-corrected event files were used for timing analysis. The photon arrival times were folded over a range of trial frequencies around the expected spin frequency. For each trial frequency, a pulse profile was constructed and fitted with a sinusoidal model to estimate the fractional amplitude. The frequency corresponding to the maximum fractional amplitude was identified as the best estimate of the spin frequency, as it maximizes phase coherence of the signal.

To illustrate this procedure, we present an example from one of the selected *Swift* observations. Figure 3.7 shows the fractional amplitude

as a function of trial frequency, exhibiting a clear peak corresponding to the optimal spin frequency.

For this observation, the exposure time is $T = 1562$ s, which sets the Fourier frequency resolution as $\delta\nu \sim 1/T \approx 6 \times 10^{-4}$ Hz. This provides an estimate of the characteristic uncertainty in the measured spin frequency. Accordingly, the best-fit frequency is determined to be $\nu_{\rm best} = 0.1804 \pm 0.0006$ Hz.

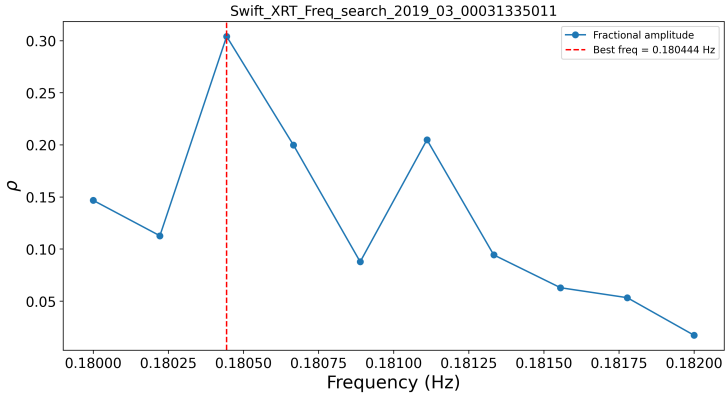


Figure 3.7: Fractional amplitude as a function of trial frequency for a representative *Swift* observation. The peak corresponds to the best-fit spin frequency where phase coherence is maximized.

Using this best-fit frequency, the event data were folded to construct the corresponding pulse profile. The resulting profile, along with its harmonic fit, is shown in Figure 3.8.

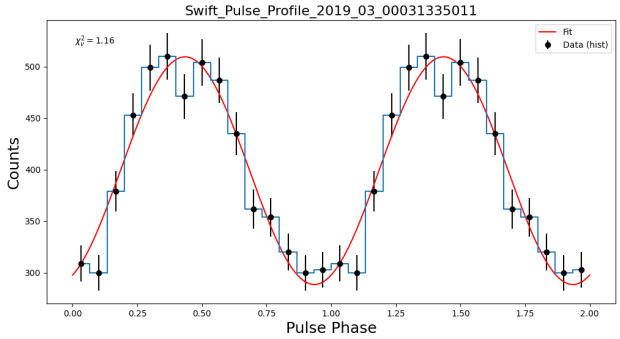


Figure 3.8: Pulse profile corresponding to the best-fit spin frequency $f = 0.18044$ Hz for ObsID 2019_03_00031335011, along with the harmonic fit.

3.2.4 Temporal Evolution of Pulse Profiles from *Swift*-XRT Observations

The same procedure was applied to the remaining selected *Swift* datasets. The resulting pulse profiles are presented below.

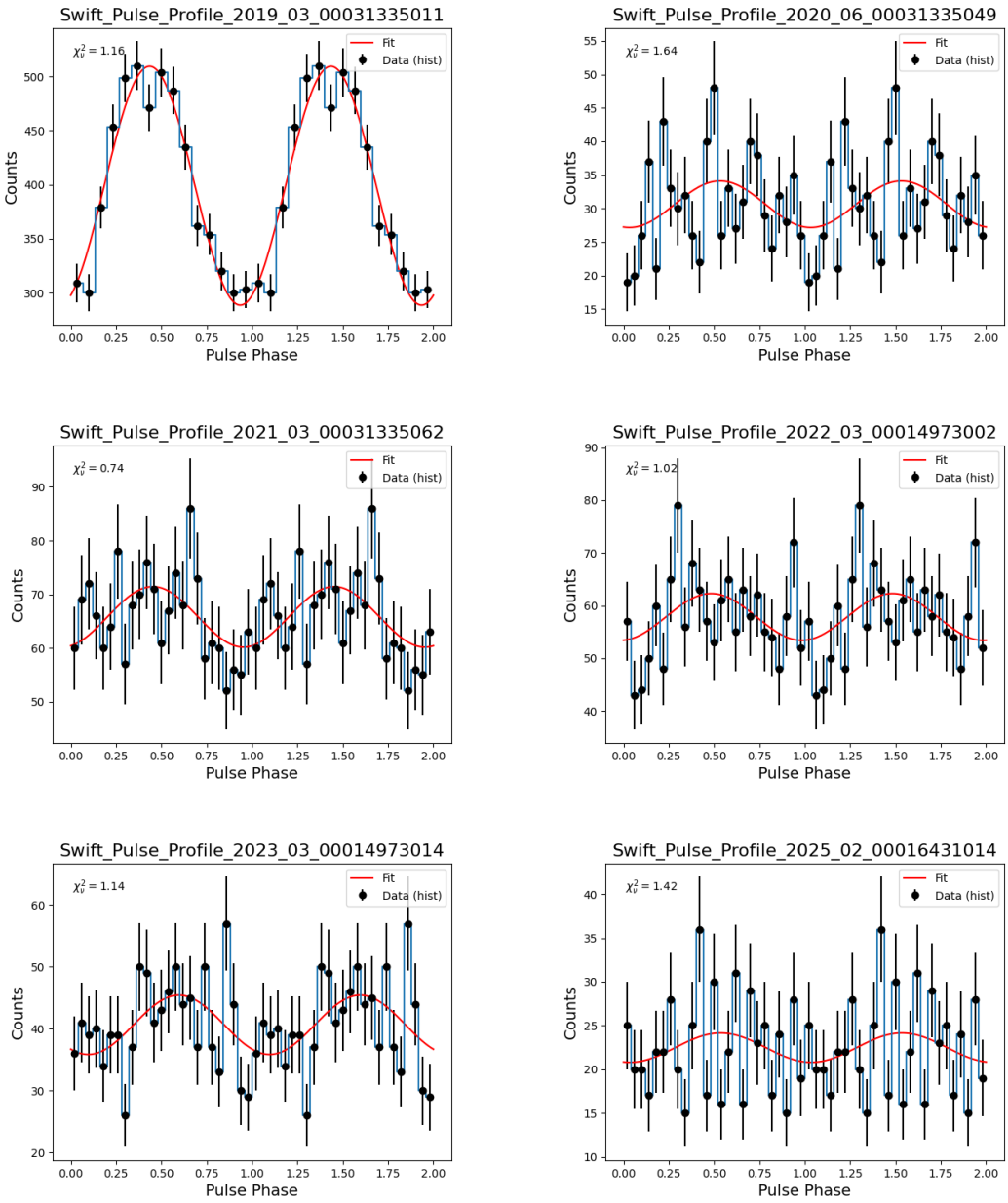


Figure 3.9: Pulse profiles obtained from selected *Swift XRT* observations spanning multiple epochs. Each profile is constructed using the best-fit frequency and corresponding number of harmonics (m) as listed in Table 3.1.

3.2.5 Spin frequency evolution

The spin frequencies for all analyzed *Swift* and *XMM-Newton* observations were determined using the procedure described above. The results are summarized in table 3.1

Table 3.1: Log of observations with estimated spin frequencies and associated harmonics.

Instrument	ObsID	Date	m	Frequency (Hz)
XMM	0804590701	03/03/2018	1	0.18046 ± 0.00009
Swift	00031335006	08/02/2019	1	0.1804 ± 0.0005
Swift	00031335007	15/02/2019	1	0.1804 ± 0.0002
Swift	00031335008	22/02/2019	1	0.1804 ± 0.0005
Swift	00031335009	02/03/2019	1	0.1804 ± 0.0007
Swift	00031335010	08/03/2019	1	0.1800 ± 0.0014
Swift	00031335011	13/03/2019	1	0.1804 ± 0.0007
XMM	0784303101	04/03/2019	3	0.18046 ± 0.00007
Swift	00031335012	15/03/2019	1	0.1804 ± 0.0005
Swift	00031335013	22/03/2019	2	0.1804 ± 0.0006
Swift	00031335014	29/03/2019	2	0.1804 ± 0.0005
Swift	00031335015	05/04/2019	1	0.1804 ± 0.0010
Swift	00031335016	12/04/2019	1	0.1811 ± 0.0017
Swift	00031335017	17/04/2019	1	0.1807 ± 0.0007
Swift	00031335018	19/04/2019	1	0.1804 ± 0.0005
Swift	00031335021	03/05/2019	1	0.1804 ± 0.0007
Swift	00031335023	17/05/2019	1	0.1804 ± 0.0006
Swift	00031335024	24/05/2019	2	0.1804 ± 0.0005
Swift	00031335025	30/05/2019	1	0.1802 ± 0.0024
Swift	00031335026	01/06/2019	2	0.1804 ± 0.0006
Swift	00031335027	09/06/2019	1	0.1804 ± 0.0005
Swift	00031335028	25/06/2019	2	0.1811 ± 0.0011
Swift	00031335029	26/06/2019	1	0.1800 ± 0.0018
Swift	00031335031	30/06/2019	1	0.1800 ± 0.0017
Swift	00031335032	03/07/2019	1	0.1800 ± 0.0012
Swift	00031335033	09/07/2019	1	0.1811 ± 0.0064
Swift	00031335034	12/07/2019	1	0.1804 ± 0.0009

Instrument	ObsID	Date	m	Frequency (Hz)
Swift	00031335035	22/07/2019	1	0.1811 ± 0.0022
Swift	00031335036	25/07/2019	1	0.1804 ± 0.0007
Swift	0031335038	13/08/2019	1	0.1804 ± 0.0006
Swift	00031335039	23/08/2019	1	0.1807 ± 0.0006
Swift	00031335040	31/08/2019	1	0.1803 ± 0.0008
Swift	00031335041	05/09/2019	1	0.1811 ± 0.0030
Swift	00031335042	10/09/2019	1	0.1811 ± 0.0011
Swift	00031335043	17/09/2019	1	0.1804 ± 0.0005
XMM	0784303201	22/09/2019	3	0.18044 ± 0.00001
Swift	00031335044	25/09/2019	1	0.1802 ± 0.0006
Swift	00031335045	06/10/2019	1	0.1804 ± 0.0006
Swift	00031335046	15/10/2019	1	0.1804 ± 0.0004
Swift	00031335047	25/10/2019	1	0.1804 ± 0.0006
Swift	00031335048	18/03/2020	1	0.1801 ± 0.0006
Swift	00031335049	20/06/2020	1	0.1804 ± 0.0010
Swift	00031335050	21/06/2020	1	0.1802 ± 0.0005
Swift	00031335051	26/06/2020	1	0.1804 ± 0.0007
Swift	00031335052	28/06/2020	1	0.1804 ± 0.0005
Swift	00031335053	02/07/2020	2	0.1804 ± 0.0003
Swift	00031335054	14/07/2020	1	0.1802 ± 0.0009
Swift	00031335055	15/07/2020	1	0.1804 ± 0.0007
Swift	00031335056	28/07/2020	1	0.1804 ± 0.0004
Swift	00031335057	11/08/2020	1	0.1804 ± 0.0003
Swift	00031335058	25/08/2020	1	0.1804 ± 0.0004
Swift	00031335059	11/02/2021	1	0.1799 ± 0.0006
Swift	03110871001	12/02/2021	1	0.1803 ± 0.0002
Swift	00031335060	12/02/2021	1	0.1803 ± 0.0026
Swift	00031335061	18/02/2021	1	0.1810 ± 0.0010
Swift	00031335062	11/03/2021	1	0.1790 ± 0.0003
Swift	00031335063	11/04/2021	1	0.1790 ± 0.0004
Swift	00031335064	11/05/2021	1	0.1803 ± 0.0005
Swift	03110991001	12/05/2021	1	0.1811 ± 0.0010
Swift	00031335067	17/06/2021	1	0.1798 ± 0.0005
Swift	00031335068	11/07/2021	1	0.1804 ± 0.0004

Instrument	ObsID	Date	m	Frequency (Hz)
Swift	00031335069	11/08/2021	1	0.1809 ± 0.0003
Swift	00031335070	11/09/2021	1	0.1822 ± 0.0004
Swift	00031335071	13/10/2021	1	0.1807 ± 0.0003
Swift	00031335072	06/11/2021	1	0.1802 ± 0.0003
Swift	00014973002	10/03/2022	1	0.1806 ± 0.0002
Swift	00014973003	10/04/2022	1	0.1806 ± 0.0002
Swift	00014973004	10/05/2022	1	0.1815 ± 0.0003
Swift	00014973005	10/06/2022	1	0.1797 ± 0.0004
Swift	00014973006	10/07/2022	1	0.1820 ± 0.0003
Swift	00014973007	10/08/2022	1	0.1808 ± 0.0003
Swift	00014973008	10/09/2022	1	0.1808 ± 0.0005
Swift	00014973009	11/09/2022	1	0.1812 ± 0.0006
XMM	0913991301	17/09/2022	1	0.18042 ± 0.00003
Swift	00014973011	15/10/2022	1	0.1802 ± 0.0003
Swift	00014973013	14/02/2023	1	0.1801 ± 0.0003
Swift	00014973014	13/03/2023	1	0.1803 ± 0.0004
Swift	00014973015	27/03/2023	1	0.1803 ± 0.0006
Swift	00014973016	14/04/2023	1	0.1802 ± 0.0003
Swift	00014973017	14/05/2023	1	0.1820 ± 0.0005
Swift	00014973018	14/06/2023	1	0.1801 ± 0.0004
Swift	00014973019	14/07/2023	1	0.1794 ± 0.0003
Swift	00014973020	14/08/2023	1	0.1799 ± 0.0002
Swift	00014973021	14/09/2023	1	0.1805 ± 0.0003
XMM	0921410201	24/09/2023	1	0.18042 ± 0.00003
Swift	00014973022	14/10/2023	1	0.1807 ± 0.0003
Swift	00016431001	11/02/2024	1	0.1809 ± 0.0003
Swift	00016431002	11/03/2024	1	0.1813 ± 0.0003
XMM	0921410301	07/04/2024	1	0.18040 ± 0.00002
Swift	00016431003	11/04/2024	1	0.1803 ± 0.0008
Swift	00016431004	12/04/2024	1	0.1792 ± 0.0007
Swift	00016431005	16/04/2024	1	0.1801 ± 0.0004
Swift	00016431006	20/04/2024	1	0.1817 ± 0.0008
Swift	00016431007	11/05/2024	1	0.1792 ± 0.0003

Instrument	ObsID	Date	m	Frequency (Hz)
Swift	00016431008	11/06/2024	1	0.1802 ± 0.0007
Swift	00016431009	11/07/2024	1	0.1792 ± 0.0003
Swift	00016431011	11/08/2024	1	0.1812 ± 0.0005
Swift	00016431012	11/10/2024	1	0.1809 ± 0.0003
Swift	00016431014	10/02/2025	1	0.1802 ± 0.0007
Swift	00016431015	13/02/2025	1	0.1808 ± 0.0004
Swift	00016431016	10/04/2025	1	0.1797 ± 0.0003
Swift	00016431017	10/06/2025	1	0.1805 ± 0.0004
Swift	00016431019	10/08/2025	1	0.1801 ± 0.0005
Swift	00016431020	13/08/2025	1	0.1808 ± 0.0005

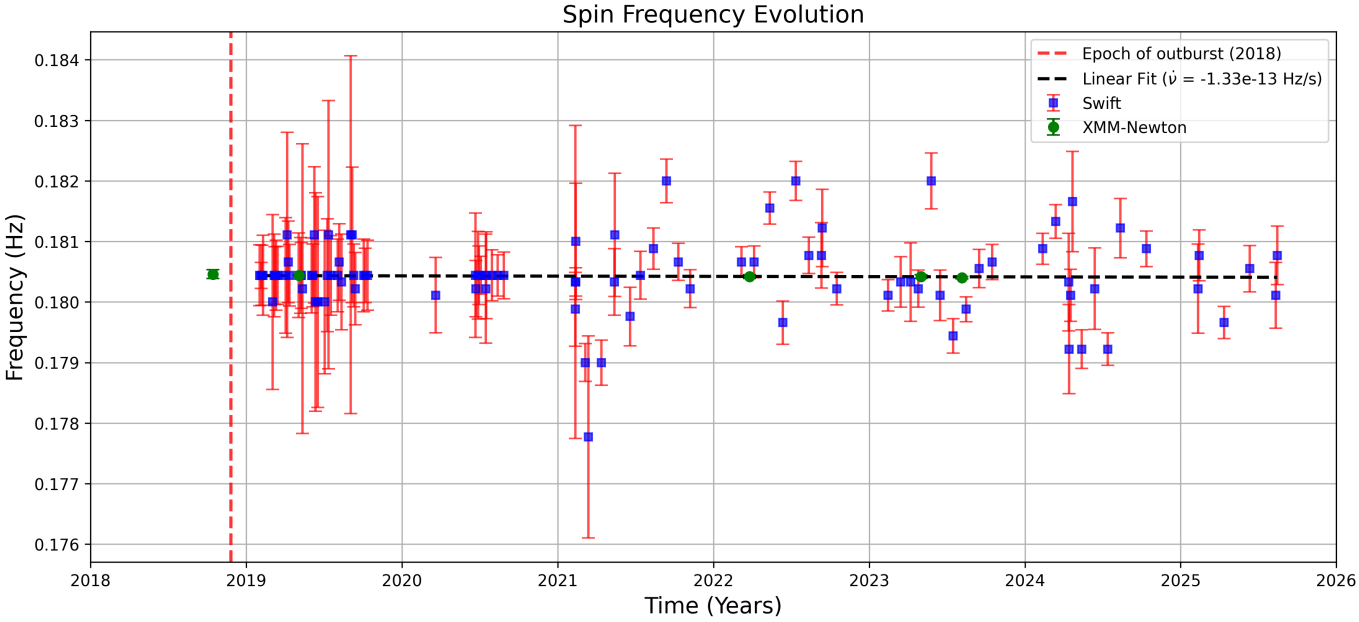


Figure 3.10: Spin frequency evolution pre and post outburst.

The pulse profile evolution (Figures 3.6 and 3.9) together with the spin frequency evolution (Figure 3.10) reveals the following:

Pulse profile plots

- **Emission Geometry:** The pulse profiles from both *XMM-Newton* and *Swift XRT* observations show predominantly double-peaked structures, indicating emission from multiple hot regions on the neutron star surface. This is consistent with thermal emission from magnetically confined hot spots, shaped by the viewing geometry and magnetic field configuration Alford and Halpern 2016.

- **Profile Complexity and Temporal Evolution:** The overall pulse morphology remains broadly consistent across epochs, although variations in amplitude and smoothness are observed. The *XMM-Newton* profiles appear smoother due to higher photon statistics, while *Swift* profiles are noisier but retain the same underlying structure. This suggests that the global emission geometry remains stable, while the emitting regions evolve gradually during the post-outburst decay.

- **Pulse Amplitude Evolution:** A gradual reduction in pulse amplitude is observed at later epochs, indicating a decrease in the contrast between hot and cooler regions on the neutron star surface. This is consistent with thermal cooling of the hot spots and a decline in magnetospheric activity as the source evolves towards quiescence.

Spin frequency

- **Long-term Spin Evolution:** The spin frequency remains nearly constant around ~ 0.1804 Hz over multiple years, with only small variations. This indicates a gradual spin-down of the magnetar, consistent with rotational energy loss due to strong magnetic braking.

- **Variation in External Torque:** Small changes in the measured frequency reflect variations in the external torque acting on the neutron star. These variations are likely associated with magnetospheric processes such as magnetic field reconfiguration and enhanced particle outflows during the post-outburst phase.

- **Measured Spin-down Rate:** The linear fit gives a spin-down rate of $\dot{\nu} \approx -1.33 \times 10^{-13}$ Hz s^{-1}, indicating a steady long-term loss of rotational energy likely consistent with magnetic braking and post-outburst torque evolution.

Having examined the temporal evolution of both the pulse profile and spin frequency, it is important to study energy dependence of the pulse morphology.

3.3 Evolution of Pulse profile in different energy bands

Energy-resolved pulse profiles help us know which part of the emission comes from the surface or magnetosphere due to magnetospheric scattering. In this subsection, we present pulse profiles in multiple energy ranges to investigate how the magnetar's emission structure responds across the X-ray spectrum during and after the 2018 active phase.

However, a detailed quantitative analysis of the energy-dependent pulse morphology could not be performed from *Swift* XRT observations. This is primarily due to the limited photon statistics in individual energy bands. When the data are divided into narrower energy ranges, the count rate becomes too low to reliably constrain pulse shape parameters or perform harmonic decomposition with statistical significance.

Below are the plots showcasing pulse profile, for each of the 6 observations of *XMM-Newton*, in different energy bands.

0804590701 (03-03-2018)

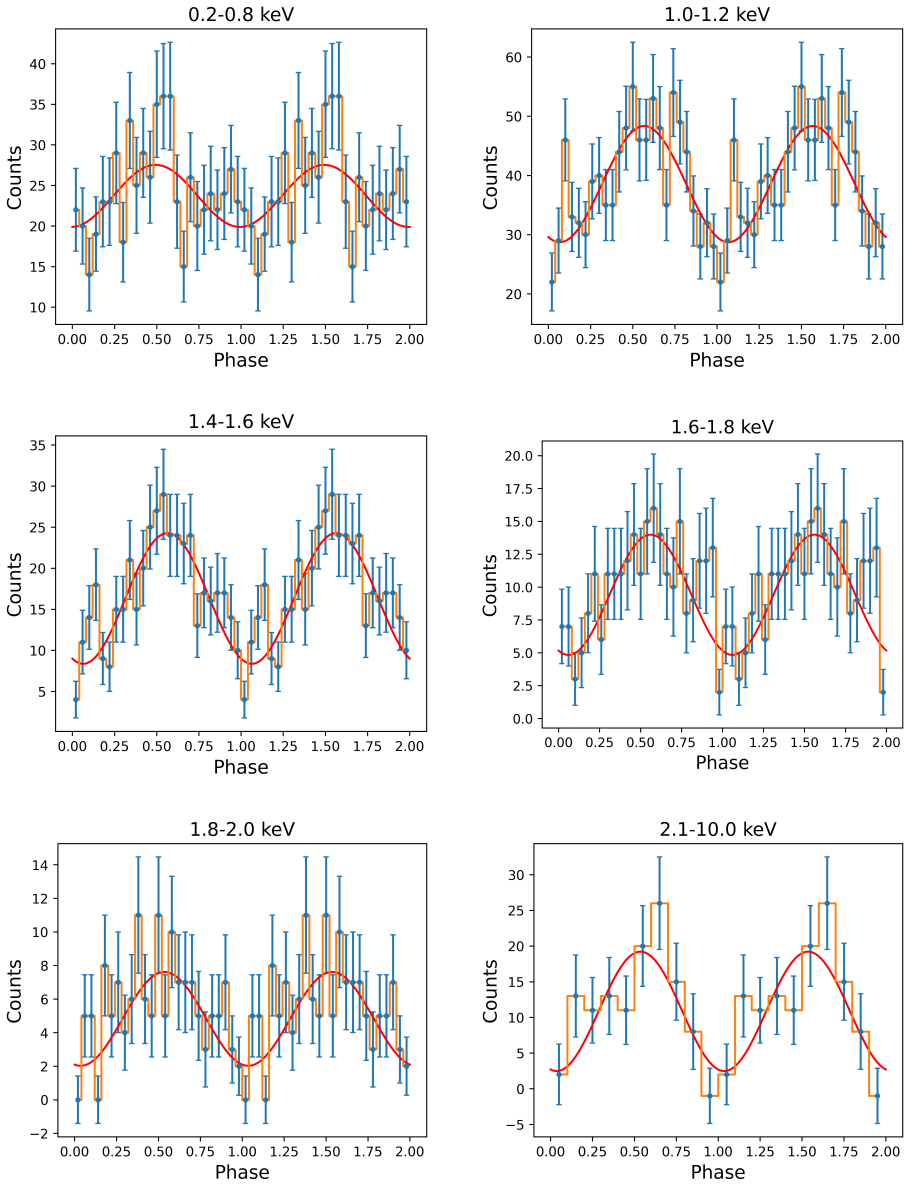


Figure 3.11: Best-fit pulse profiles for energy bands 0.2–0.8 keV, 1.0–1.2 keV, 1.4–1.6 keV, 1.8–2.0 keV, 3.0–4.0 keV, and 4.8–10.0 keV. All profiles are modeled using a single harmonic component.

0784303101 (04-03-2019)

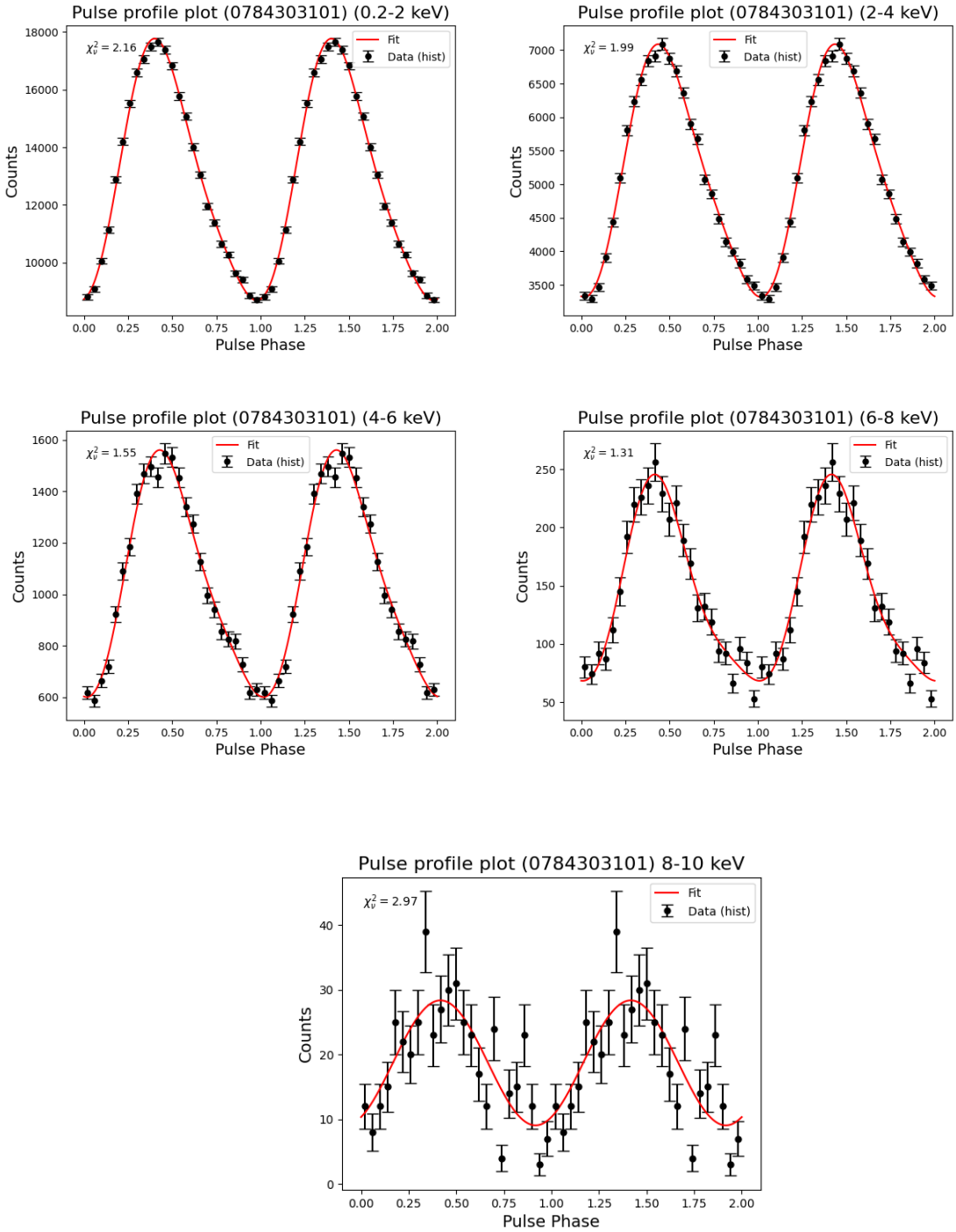


Figure 3.12: Best fit pulse profile plots for energy bands: 0.2 -2 keV, 2-4 keV, 4-6 keV, 6-8 keV, 8-10 keV, respectively. No. of harmonics used (from left to right and top to bottom): 2,2,2,2,1 respectively.

0784303201 (22-09-2019)

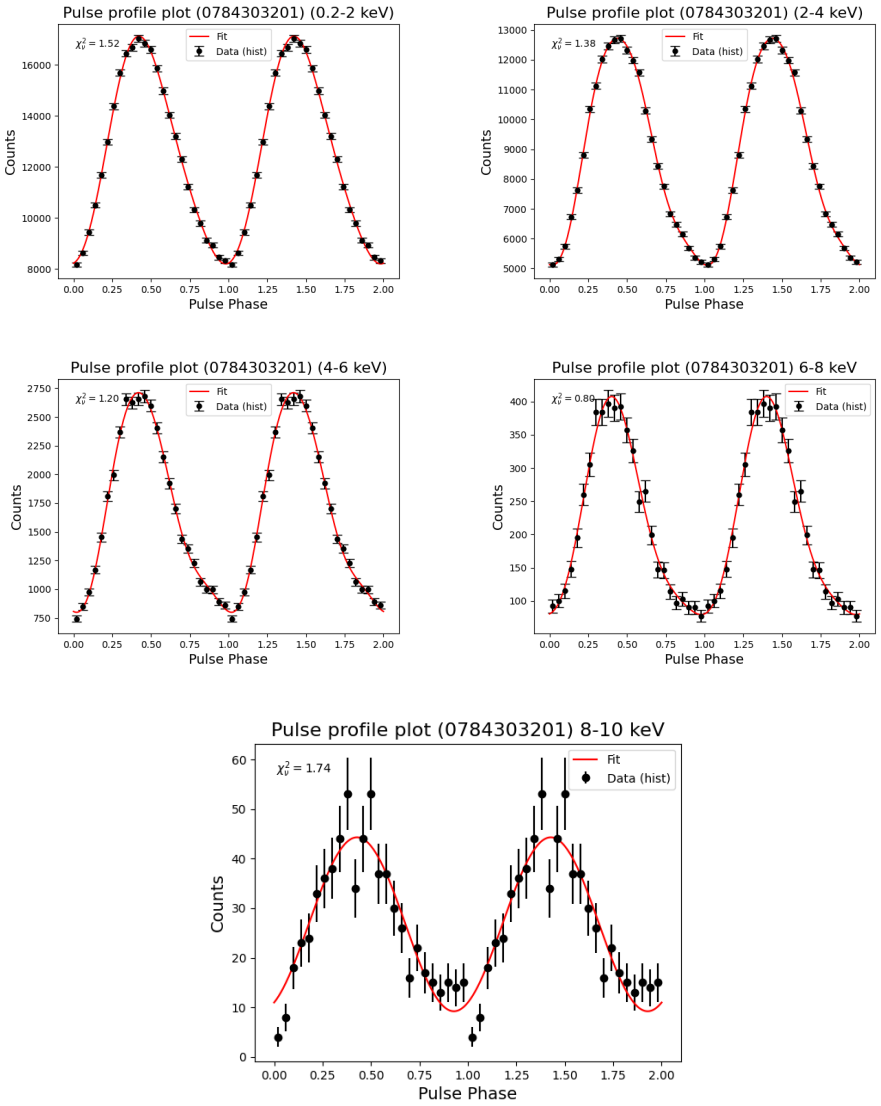


Figure 3.13: Best-fit pulse profiles for energy bands 0.2–2 keV, 2–4 keV, 4–6 keV, 6–8 keV, and 8–10 keV. The number of harmonics used (left to right and top to bottom) are 2, 3, 3, 2, and 1, respectively.

0913991301 (17-09-2022)

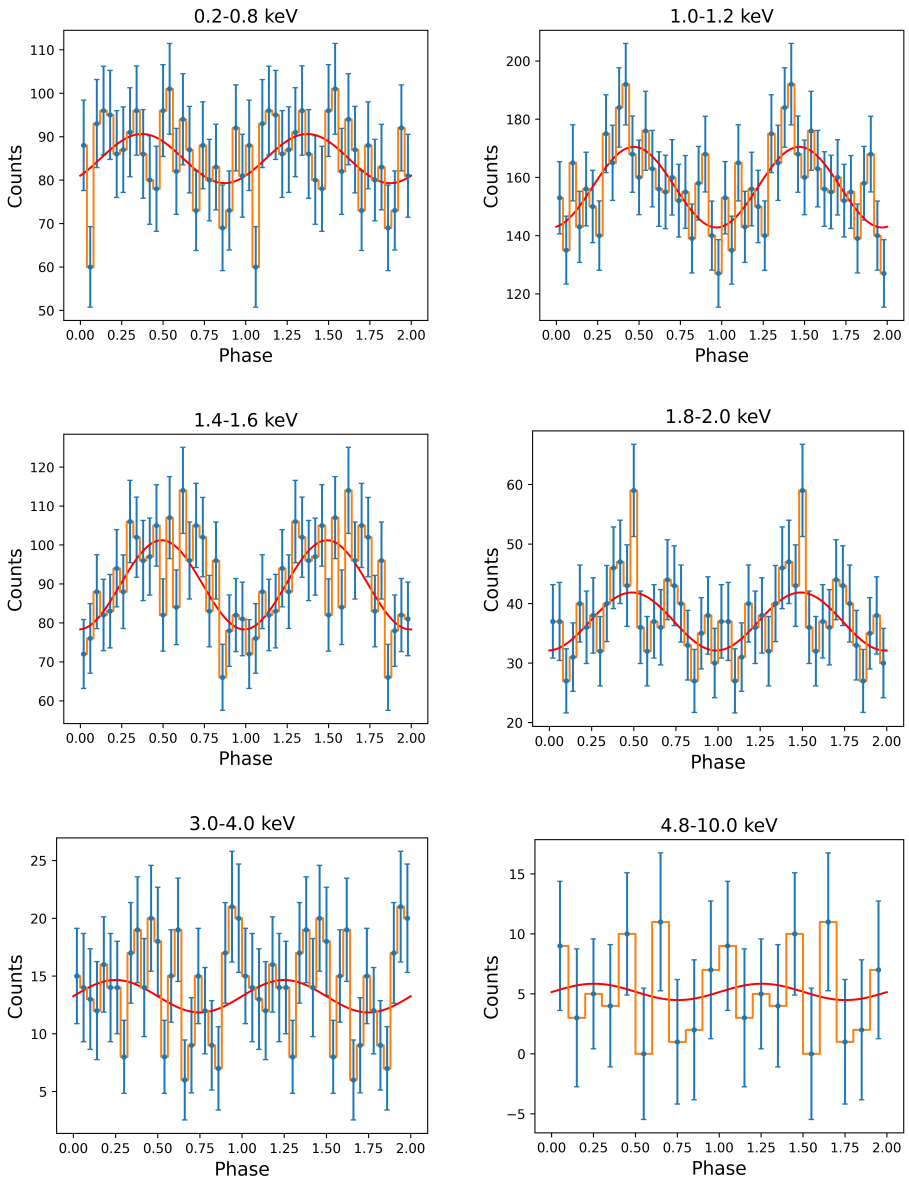


Figure 3.14: Best-fit pulse profiles for energy bands 0.2–0.8 keV, 1.0–1.2 keV, 1.4–1.6 keV, 1.8–2.0 keV, 3.0–4.0 keV, and 4.8–10.0 keV. All profiles are modeled using a single harmonic component.

0921410201 (24-09-2023)

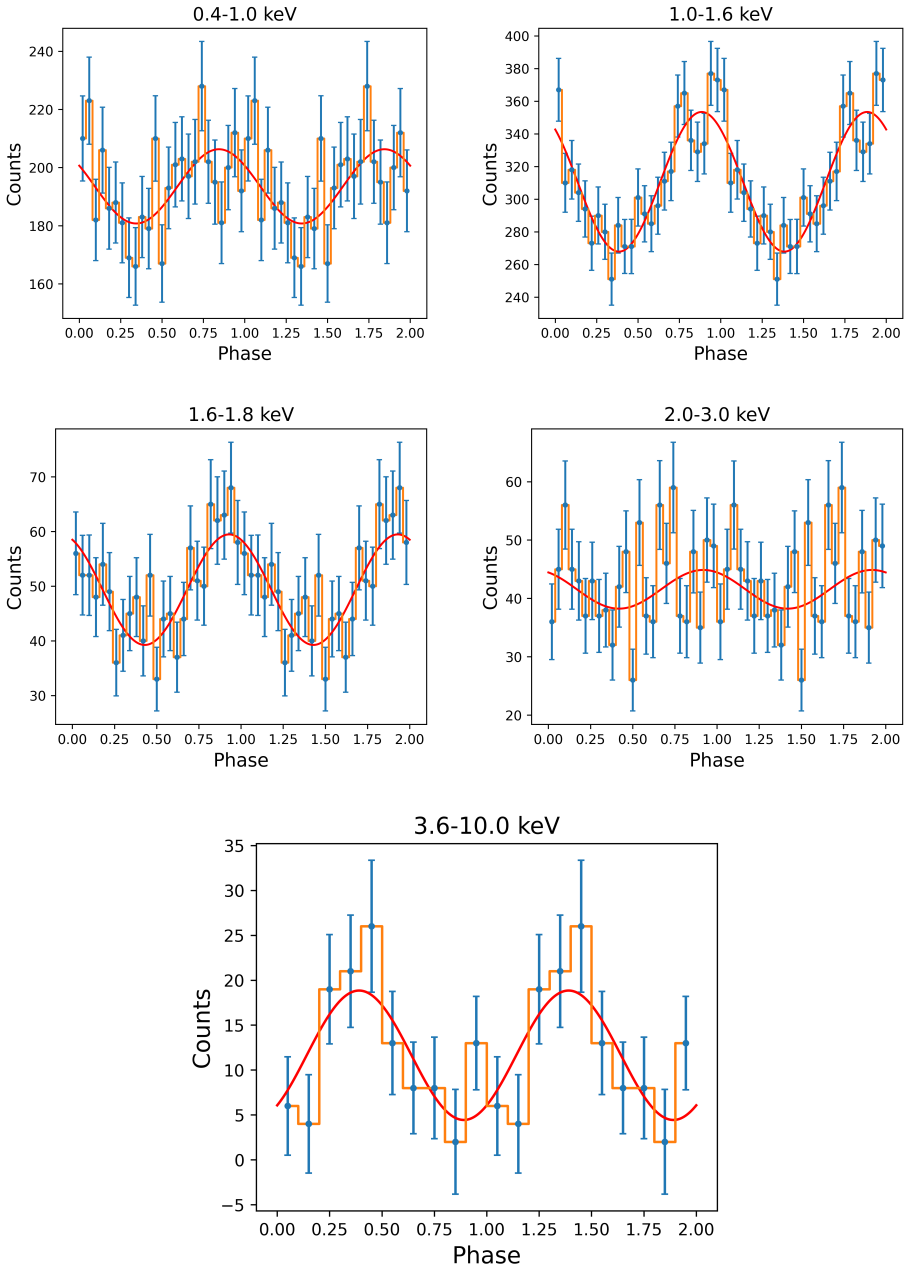


Figure 3.15: Best-fit pulse profiles for energy bands 0.4–1.0 keV, 1.0–1.6 keV, 1.6–1.8 keV, 2.0–3.0 keV, and 3.6–10.0 keV. All profiles are modeled using a single harmonic component.

0921410301 (07-04-2024)

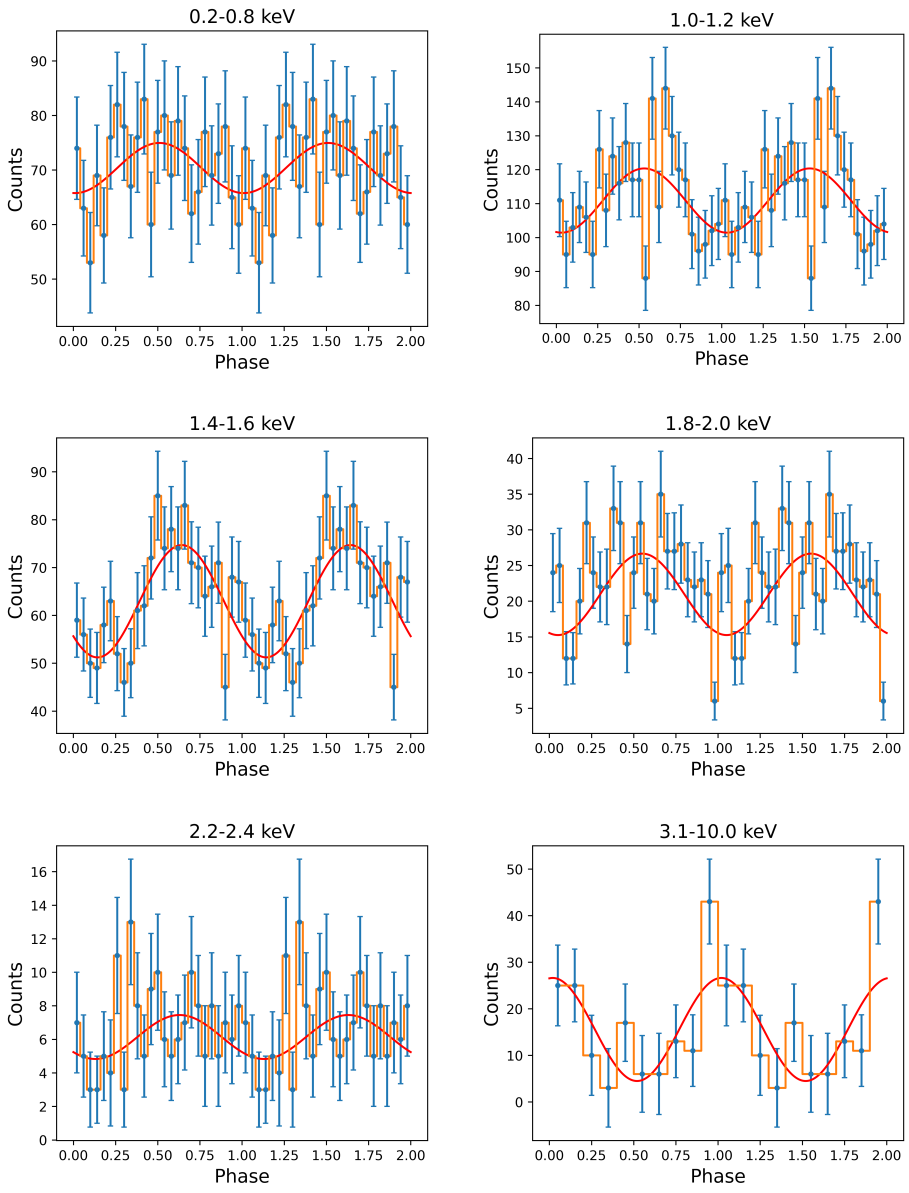


Figure 3.16: Best-fit pulse profiles for energy bands 0.2–0.8 keV, 1.0–1.2 keV, 1.4–1.6 keV, 1.8–2.0 keV, 2.2–2.4 keV, and 3.1–10.0 keV. All profiles are modeled using a single harmonic component.

We infer the following from the pulse profile plots in different energy bands:

- **Energy Dependence of Pulse Modulation:** The pulse profiles show a clear dependence on energy across the observations (ObsIDs 0804590701 and 0784303101). In the softer X-ray bands (0.2–2 and 2–4 keV), the pulses are strong and well structured, with distinct features such as double peaks, particularly in the post-outburst phase. As we move to higher energies (above 4 keV), the profiles gradually flatten and become noisier, indicating a noticeable reduction in the strength of modulation.

- **Origin of Emission Components:** This energy-dependent behaviour suggests that the pulsed emission is largely driven by a soft thermal component, most likely originating from thermal hot region on the neutron star surface. On the other hand, the harder X-ray emission appears to be less strongly modulated, which may indicate a more uniform origin, such as magnetospheric emission or scattering effects.

- **Long-term Spectral Evolution:** At later epochs (post-2020), the pulse profiles show that most of the detectable modulation is confined to the softer energy bands. The higher-energy bands are increasingly dominated by noise due to low count rates. This trend points to a gradual fading of the hard X-ray component that was enhanced during the outburst, suggesting that the source is steadily returning to a quiescent state characterized by softer and more uniform emission.

While these trends show how the pulse shape changes with energy and time, we can now examine how much each harmonic contributes to the overall pulse profile. This can provide deeper insight into the underlying emission geometry and how the pulse profile evolves. To do this, we compute the fractional amplitudes of individual harmonics, which serve as a measure of the modulation strength associated with each component.

3.4 Fractional Amplitude of subpeaks

Once we obtain the pulse profile, as mentioned in Chapter 1, we can examine how the subpeaks evolve with time. By subpeaks, we refer to the contribution of each harmonic, or equivalently, the evolution of the fractional amplitude of each harmonic as a function of time, as described in equation (3.5).

3.4.1 Evolution of fractional amplitude with time

Let us first look at the evolution of fractional amplitude with time. Below is the table showcasing observation details with frequencies and m harmonics.

Table 3.2: Log of observations with measured fractional amplitudes and harmonics.

Instrument	ObsID	Date	m	Fractional Amplitude (%)
XMM	0804590701	03/03/2018	1	1^{st} = 24.67 ± 1.38
Swift	00031335006	08/02/2019	1	1^{st} = 28.41 ± 0.92
Swift	00031335007	15/02/2019	2	1^{st} = 17.05 ± 0.81 2^{nd} = 0.76 ± 0.80
Swift	00031335008	22/02/2019	1	1^{st} = 27.92 ± 0.91
Swift	00031335009	02/03/2019	1	1^{st} = 29.92 ± 1.72
Swift	00031335010	08/03/2019	1	1^{st} = 13.09 ± 2.34
Swift	00031335011	13/03/2019	1	1^{st} = 27.28 ± 1.38
XMM	0784303101	04/03/2019	3	1^{st} = 34.04 ± 0.23 2^{nd} = 5.19 ± 0.23 3^{rd} = 1.66 ± 0.22
Swift	00031335012	15/03/2019	2	1^{st} = 14.58 ± 1.16 2^{nd} = 4.55 ± 1.16
Swift	00031335013	22/03/2019	2	1^{st} = 28.14 ± 0.93 2^{nd} = 6.89 ± 0.92
Swift	00031335014	29/03/2019	2	1^{st} = 26.13 ± 1.12 2^{nd} = 3.34 ± 1.10
Swift	00031335015	05/04/2019	1	1^{st} = 24.74 ± 1.80
Swift	00031335016	12/04/2019	1	1^{st} = 20.95 ± 1.43
Swift	00031335017	17/04/2019	1	1^{st} = 19.52 ± 0.95
Swift	00031335018	19/04/2019	1	1^{st} = 26.18 ± 1.43
Swift	00031335021	03/05/2019	1	1^{st} = 31.00 ± 1.52
Swift	00031335023	17/05/2019	1	1^{st} = 27.06 ± 2.22
				2^{nd} = 6.37 ± 2.18
Swift	00031335024	24/05/2019	1	1^{st} = 31.34 ± 0.97
Swift	00031335025	30/05/2019	1	1^{st} = 32.90 ± 3.02

Instrument	ObsID	Date	m	Fractional Amplitude
Swift	00031335026	01/06/2019	2	1^{st} = 29.00 ± 1.66 2^{nd} = 8.83 ± 1.63
Swift	00031335027	09/06/2019	2	1^{st} = 31.98 ± 1.73 2^{nd} = 4.47 ± 1.69
Swift	00031335028	25/06/2019	1	1^{st} = 23.38 ± 1.31
Swift	00031335029	26/06/2019	1	1^{st} = 26.86 ± 2.77
Swift	00031335031	30/06/2019	1	1^{st} = 28.95 ± 1.763
Swift	00031335032	03/07/2019	1	1^{st} = 22.82 ± 2.14
Swift	00031335033	09/07/2019	1	1^{st} = 23.86 ± 6.03
Swift	00031335034	12/07/2019	1	1^{st} = 31.33 ± 1.75
Swift	00031335035	22/07/2019	1	1^{st} = 26.71 ± 8.62
Swift	00031335036	25/07/2019	1	1^{st} = 28.02 ± 2.37
Swift	00031335038	13/08/2019	1	1^{st} = 36.08 ± 2.26 2^{nd} = 5.65 ± 2.19
Swift	00031335039	23/08/2019	1	1^{st} = 19.50 ± 2.24
Swift	00031335040	31/08/2019	1	1^{st} = 22.15 ± 3.45
Swift	00031335041	05/09/2019	1	1^{st} = 26.10 ± 5.45
Swift	00031335042	10/09/2019	1	1^{st} = 23.61 ± 4.30
Swift	00031335043	17/09/2019	1	1^{st} = 6.41 ± 1.49
XMM	0784303201	22/09/2019	3	1^{st} = 29.39 ± 0.10 2^{nd} = 0.79 ± 0.09 3^{rd} = 0.35 ± 0.09
Swift	00031335044	25/09/2019	1	1^{st} = 22.09 ± 1.47
Swift	00031335045	06/10/2019	1	1^{st} = 13.94 ± 2.29
Swift	00031335046	15/10/2019	1	1^{st} = 18.20 ± 1.96
Swift	00031335047	25/10/2019	1	1^{st} = 19.37 ± 1.80
Swift	00031335048	18/03/2020	1	1^{st} = 13.98 ± 2.91
Swift	00031335049	20/06/2020	1	1^{st} = 12.19 ± 4.05
Swift	00031335050	21/06/2020	1	1^{st} = 16.05 ± 1.17
Swift	00031335051	26/06/2020	1	1^{st} = 13.02 ± 2.39
Swift	00031335052	28/06/2020	1	1^{st} = 12.55 ± 2.06
Swift	00031335053	02/07/2020	1	1^{st} = 15.54 ± 2.00
Swift	00031335054	14/07/2020	1	1^{st} = 13.78 ± 1.64
Swift	00031335055	15/07/2020	1	1^{st} = 5.90 ± 2.31
Swift	00031335056	28/07/2020	1	1^{st} = 15.18 ± 1.98

Instrument	ObsID	Date	m	Fractional Amplitude
Swift	00031335057	11/08/2020	1	1^{st} = 9.62 ± 1.23
Swift	00031335058	25/08/2020	1	1^{st} = 15.01 ± 2.96
Swift	00031335059	11/02/2021	1	1^{st} = 11.18 ± 2.35
Swift	03110871001	12/02/2021	1	1^{st} = 20.58 ± 8.92
Swift	00031335060	12/02/2021	1	1^{st} = 12.97 ± 3.09
Swift	00031335061	18/02/2021	1	1^{st} = 3.97 ± 2.29
Swift	00031335062	11/03/2021	1	1^{st} = 8.42 ± 1.68
Swift	00031335064	11/05/2021	1	1^{st} = 11.25 ± 3.67
Swift	03110991001	12/05/2021	1	1^{st} = 16.33 ± 2.99
Swift	00031335067	17/06/2021	1	1^{st} = 4.94 ± 2.58
Swift	00031335068	11/07/2021	1	1^{st} = 8.97 ± 3.18
Swift	00031335069	11/08/2021	1	1^{st} = 8.79 ± 3.00
Swift	00031335070	11/09/2021	1	1^{st} = 5.76 ± 1.93
Swift	00031335071	13/10/2021	1	1^{st} = 5.33 ± 3.35
Swift	00031335072	06/11/2021	1	1^{st} = 10.80 ± 1.75
Swift	00014973002	10/03/2022	1	1^{st} = 6.95 ± 2.89
Swift	00014973003	10/04/2022	1	1^{st} = 4.37 ± 1.35
Swift	00014973004	10/05/2022	1	1^{st} = 5.02 ± 1.99
Swift	00014973005	10/06/2022	1	1^{st} = 14.01 ± 1.95
Swift	00014973006	10/07/2022	1	1^{st} = 7.88 ± 1.92
Swift	00014973007	10/08/2022	1	1^{st} = 9.37 ± 1.89
Swift	00014973008	10/09/2022	1	1^{st} = 3.95 ± 3.18
Swift	00014973009	11/09/2022	1	1^{st} = 13.28 ± 3.58
XMM	0913991301	17/09/2022	1	1^{st} = 9.61 ± 0.86
Swift	00014973011	15/10/2022	1	1^{st} = 10.02 ± 1.97
Swift	00014973013	14/02/2023	1	1^{st} = 7.14 ± 2.11
Swift	00014973014	13/03/2023	1	1^{st} = 12.47 ± 2.83
Swift	00014973015	27/03/2023	1	1^{st} = 12.23 ± 4.94
Swift	00014973016	14/04/2023	1	1^{st} = 7.20 ± 1.18
Swift	00014973017	14/05/2023	1	1^{st} = 12.18 ± 3.29
Swift	00014973018	14/06/2023	1	1^{st} = 9.75 ± 2.15
Swift	00014973019	14/07/2023	1	1^{st} = 10.69 ± 3.29
Swift	00014973020	14/08/2023	1	1^{st} = 2.37 ± 3.60
Swift	00014973021	14/09/2023	1	1^{st} = 3.28 ± 1.10
XMM	0921410201	24/09/2023	1	1^{st} = 10.60 ± 0.81

Instrument	ObsID	Date	m	Fractional Amplitude
Swift	00014973022	14/10/2023	1	1^{st} = 3.85 ± 1.19
Swift	00016431001	11/02/2024	1	1^{st} = 3.21 ± 1.92
Swift	00016431002	11/03/2024	1	1^{st} = 4.59 ± 3.76
XMM	0921410301	07/04/2024	1	1^{st} = 9.12 ± 0.80
Swift	00016431003	11/04/2024	1	1^{st} = 16.54 ± 2.23
Swift	00016431004	12/04/2024	1	1^{st} = 9.82 ± 2.31
Swift	00016431005	16/04/2024	1	1^{st} = 8.45 ± 2.10
Swift	00016431006	20/04/2024	1	1^{st} = 22.76 ± 3.87
Swift	00016431007	11/05/2024	1	1^{st} = 5.84 ± 1.63
Swift	00016431008	11/06/2024	1	1^{st} = 7.84 ± 4.26
Swift	00016431009	11/07/2024	1	1^{st} = 5.42 ± 1.27
Swift	00016431011	11/08/2024	1	1^{st} = 4.97 ± 2.00
Swift	00016431012	11/10/2024	1	1^{st} = 5.25 ± 2.13
Swift	00016431014	10/02/2025	1	1^{st} = 7.81 ± 3.52
Swift	00016431016	10/04/2025	1	1^{st} = 4.81 ± 1.96
Swift	00016431017	10/06/2025	1	1^{st} = 14.40 ± 2.32
Swift	00016431019	10/08/2025	1	1^{st} = 10.83 ± 2.26
Swift	00016431020	13/08/2025	1	1^{st} = 3.48 ± 1.84

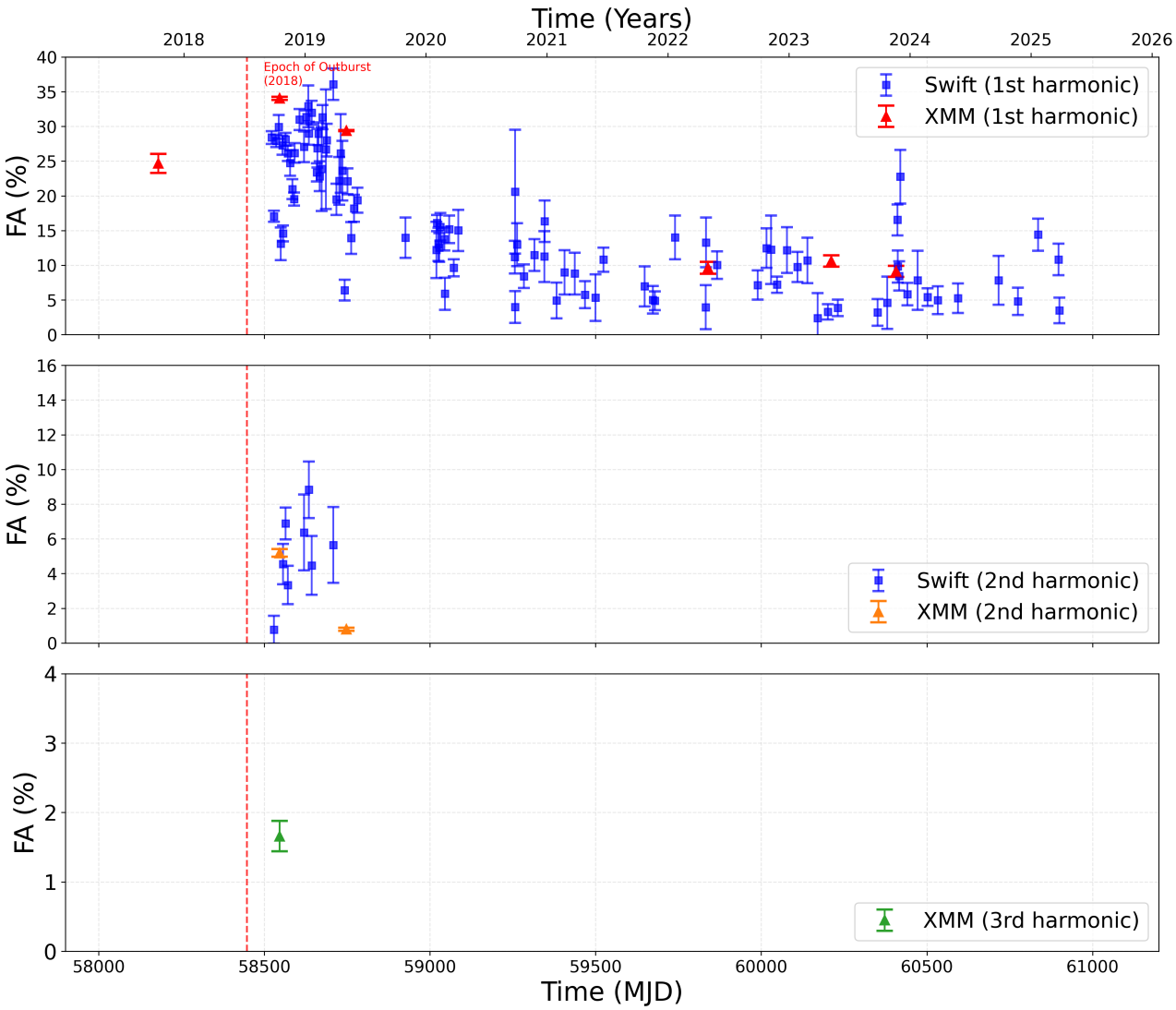


Figure 3.17: Evolution of fractional amplitude.

Referring to Fig 3.17, it can be seen how each harmonic evolves over time.

- **Post-outburst Enhancement in Pulse Amplitude:** Following the 2018 outburst (indicated by the vertical dashed line), the fractional amplitude increases, especially for the first harmonic. This suggests that the emission becomes more anisotropic immediately after the outburst, likely due to the formation of hot spots on the neutron star surface and enhanced magnetospheric activity.

- **Gradual Decline in Amplitude:** From 2019 onwards, the fractional amplitude shows an overall decline with time, despite some short-term variations. This trend is consistent with the cooling of the neutron star surface and a gradual relaxation of the magnetosphere as the source moves back toward its quiescent state.

- **Dominance of the First Harmonic:** The first harmonic remains stronger than the second, which appears weaker and more scattered throughout the observations. This indicates that the pulse profile is largely dominated by the fundamental component, pointing to a relatively simple emission geometry with broad emission regions.

3.4.2 Evolution of fractional amplitude in different energy bands

To further investigate the emission behaviour, we examine the evolution of the fractional amplitude across different energy bands in the 0.2–10 keV range. In magnetars, lower-energy photons are typically dominated by thermal surface emission, while higher-energy photons often carry a stronger magnetospheric contribution. Thus, tracing how the fractional amplitude changes with energy provides insight into the relative roles of these components during the post-outburst phase.

This analysis is performed using only *XMM-Newton* observations, as they provide higher signal-to-noise ratio and good spectral resolution compared to *Swift*-XRT. The limited photon statistics and narrower effective area of *Swift*-XRT make it less suitable for a detailed energy-resolved study of fractional amplitude, particularly when dividing the data into multiple energy bands.

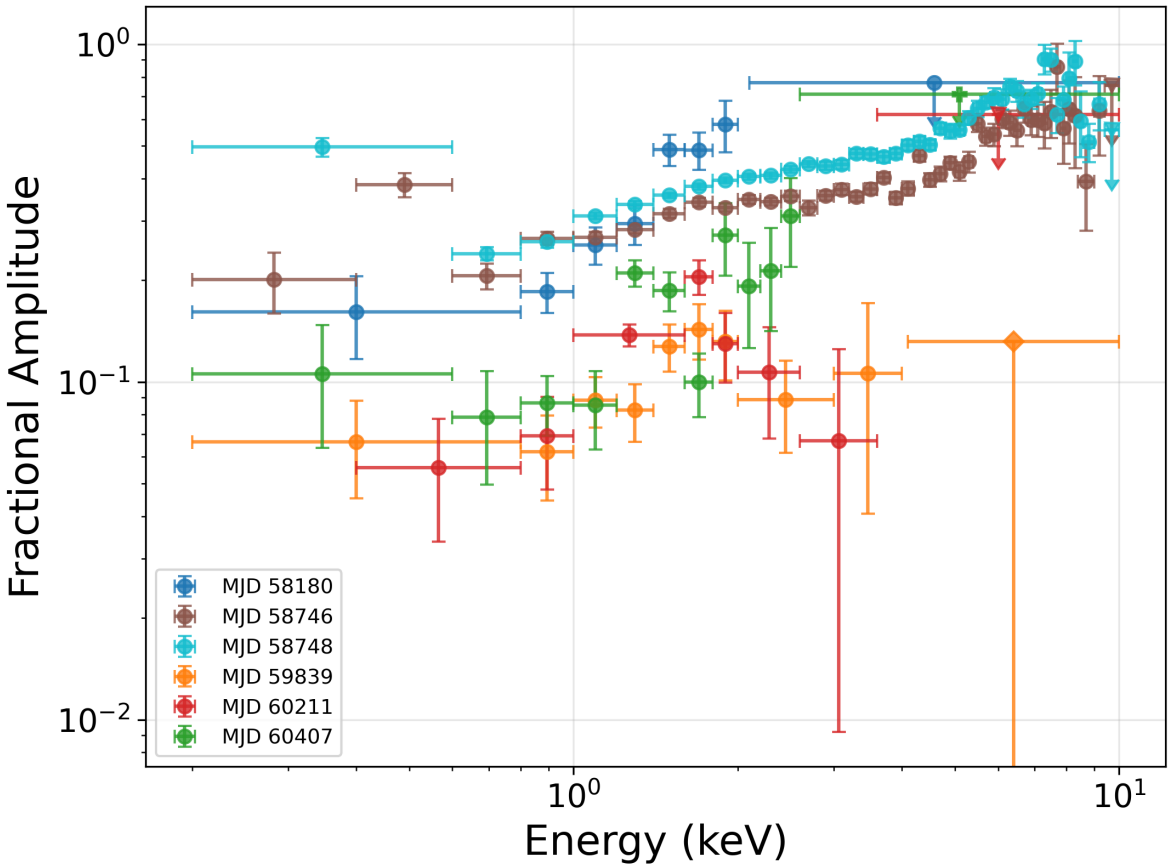


Figure 3.18: Energy-dependent fractional amplitude for all *XMM-Newton* observations, shown on logarithmic scales for both axes.

From the plot 3.18, we infer the following.

- **Increase of Amplitude with Energy:** Across all epochs, the fractional amplitude shows a clear increase with energy, starting from lower values below ~1 keV and rising toward higher energies. This suggests that the higher-energy emission is more strongly modulated, likely originating from more localized or anisotropic regions.

- **Variation Across Epochs:** The overall amplitude also changes with time. Earlier observations tend to show higher fractional amplitudes, while later epochs exhibit weaker modulation. This points to a more anisotropic emission geometry shortly after the outburst, gradually becoming more uniform as the neutron star cools and the emission redistributes.

- **Similar Behaviour at High Energies:** At higher energies, the fractional amplitudes from different epochs become consistent

within uncertainties. This suggests that the high-energy emission component—likely linked to magnetospheric processes—maintains relatively stable modulation properties, even as the softer thermal emission evolves over time.

3.4.3 Evolution of Fractional Amplitude with Energy for Each Observation

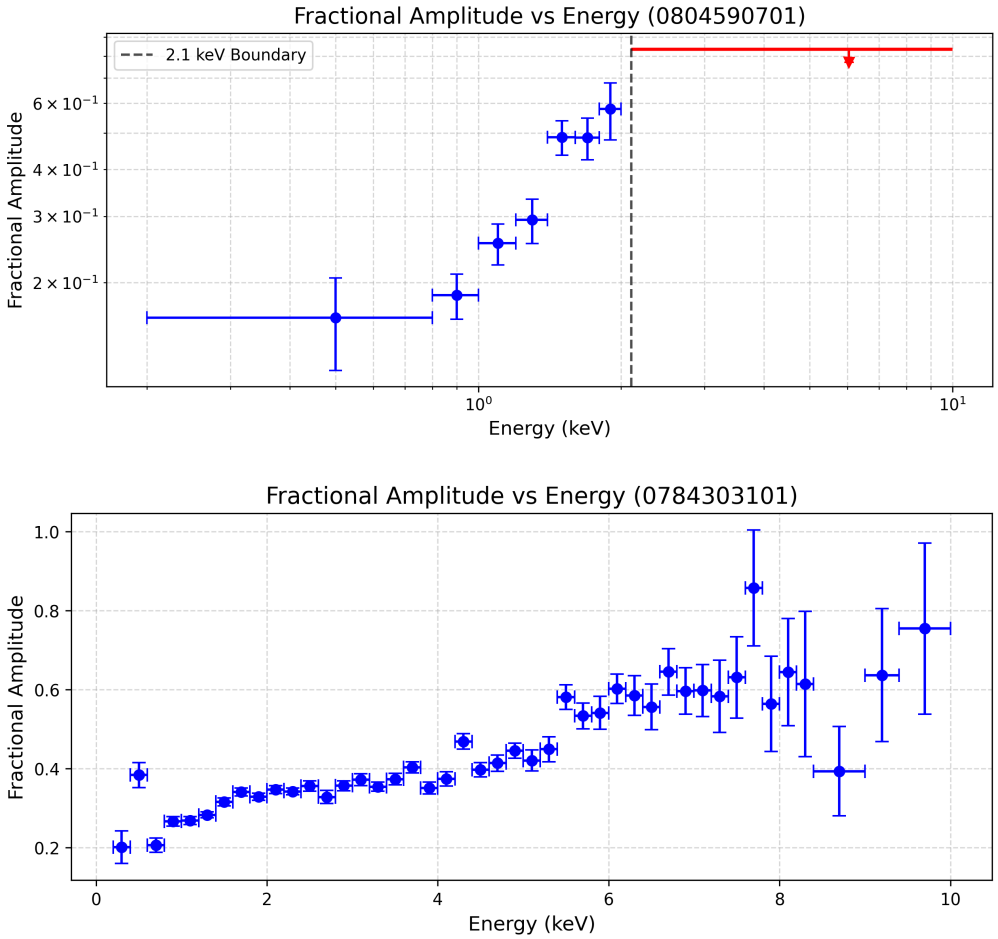


Figure 3.19: Energy dependence of the fractional amplitude for *XMM-Newton* observations. The top panel is shown in log–log scale, while the bottom panel is plotted in linear scale.

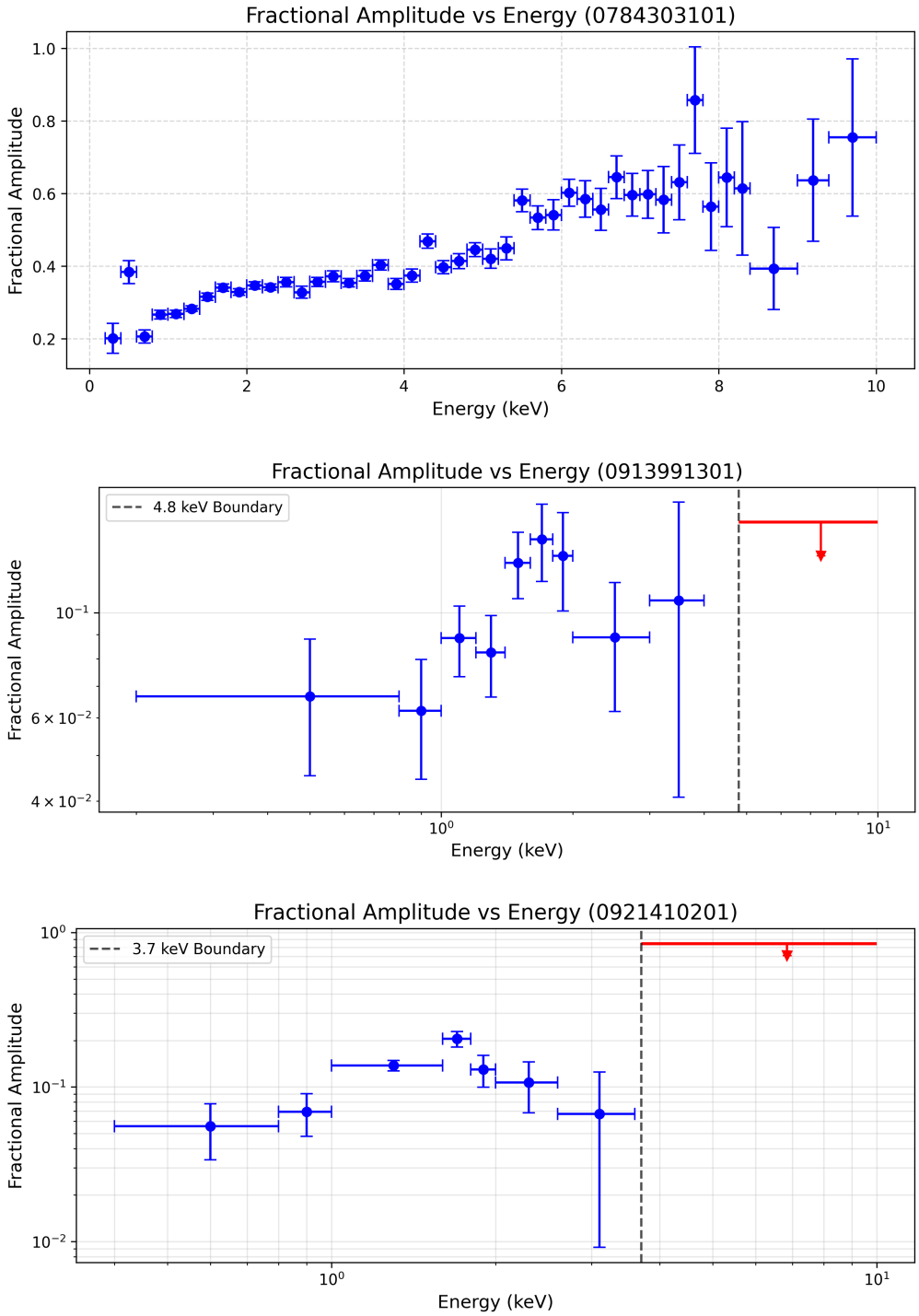


Figure 3.20: Energy dependence of the fractional amplitude for *XMM-Newton* observations. The top panel is plotted in linear scale, while the remaining panels are shown in log–log scale.

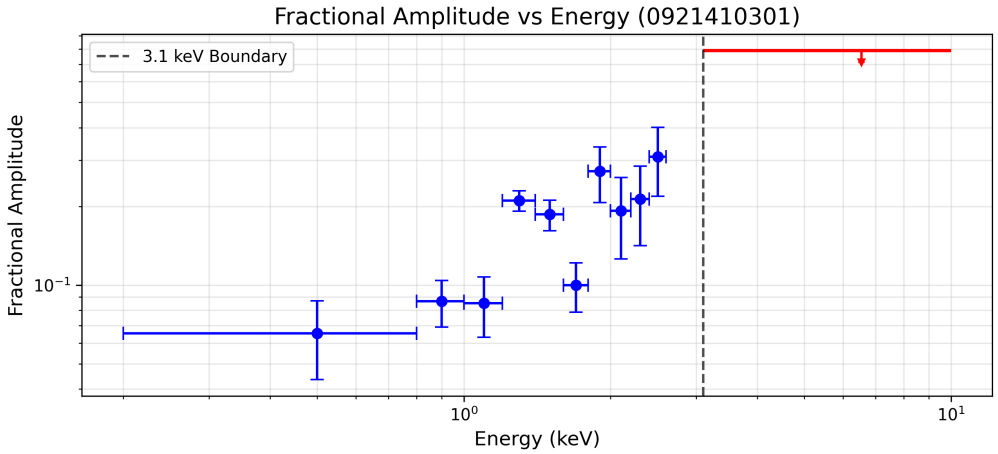


Figure 3.21: Energy dependence of the fractional amplitude for the final *XMM-Newton* observation, shown in log–log scale.

From the above plots, we infer that

- **Increase of Fractional Amplitude with Energy:** Across most observations, the fractional amplitude generally increases with energy. It starts off relatively low in the soft X-ray band ($\lesssim$2–3 keV) and becomes noticeably higher at harder energies. This suggests that the higher-energy emission is more anisotropic, likely coming from thermal hot regions or magnetospheric processes, while the softer emission is more evenly spread across the neutron star surface.

- **Stronger Energy Dependence in Early Epochs:** In the early observations following the outburst, this increase with energy is much more pronounced. The fractional amplitude reaches significantly higher values at energies above ~5 keV. This indicates that, shortly after the outburst, the emission was dominated by hotter thermal regions, leading to stronger modulation at higher energies.

- **Reduced Amplitude at Later Epochs:** At later times, the overall fractional amplitude decreases, and its dependence on energy becomes weaker and flatter. This behaviour is consistent with the cooling of the neutron star surface and a reduction in temperature contrast between different emitting regions. At the same time, the magnetosphere likely relaxes, resulting in a more uniform and less strongly modulated emission pattern.

While the energy-resolved fractional amplitude provides insight into the spectral dependence of the variability, it is also useful to quantify the overall modulation strength of the source in a single parameter. To this end, we define the total fractional amplitude as a combination of the contributions from multiple harmonics of the pulse profile. This allows us to track the global variability of the emission independent of energy.

3.5 Total Fractional amplitude

Building on the Fourier decomposition of the pulse profile defined in 3.5, where the emission is expressed as a sum of harmonic components, we can quantify the overall strength of modulation by combining the contributions from individual harmonics. This leads to the definition of the total fractional amplitude as

$$\mathrm{FA}_{\mathrm{total}} = \frac{\sqrt{\sum_{n=1}^{N} b_n^2}}{A} \tag{3.5}$$

where b_n represents the amplitude of the n-th harmonic component and A denotes the mean count rate.

The temporal evolution of the total fractional amplitude is shown in Figure 3.22.

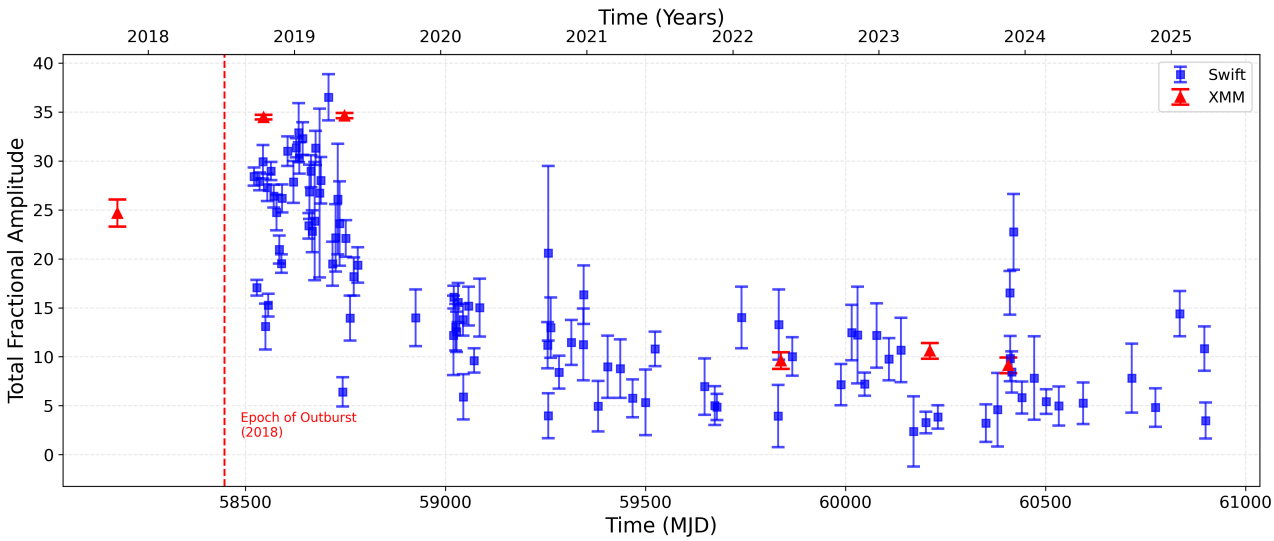


Figure 3.22: Evolution of the total fractional amplitude as a function of time.

From the above plot, we infer that:

- **Enhanced variability in the early post-outburst phase:** In the immediate aftermath of the 2018 outburst, the total fractional amplitude reaches relatively high values (~25–35%), pointing to strongly anisotropic emission. This is likely due to the presence of hot regions on the neutron star surface, along with increased magnetospheric activity, both of which contribute to a highly modulated pulse profile.

- **Gradual reduction in modulation strength:** Over time, the fractional amplitude shows a clear overall decline, eventually settling at lower levels (~5–10%). This trend suggests a progressive decrease in temperature contrast across the surface, accompanied by a relaxation of the magnetosphere, leading to a more uniform emission geometry.

- **Instrumental consistency with short-term variability:** While the Swift/XRT measurements display greater scatter—primarily due to differences in observational cadence and photon statistics—the XMM-Newton data provide more precise constraints. Despite this, both datasets consistently trace the same long-term decline in variability. The short-term fluctuations observed may be indicative of intermittent magnetospheric activity.

The temporal evolution of the total fractional amplitude provides insight into the global modulation of the emission, it does not capture how this variability depends on energy. To further probe the emission geometry and disentangle the contributions from different spectral components, it is essential to examine the energy dependence of the pulsed fraction. In the following section, we investigate the evolution of the pulsed fraction as a function of energy and its implications for the underlying emission mechanisms.

3.6 Pulsed Fraction

3.6.1 Evolution of Pulsed Fraction with energy

To investigate the energy dependence of the pulsations, we examine the variation of the pulsed fraction (PF), defined as in Equation (1.1), as a function of energy across multiple observational epochs. Figure 3.23 shows the fractional amplitude measured in different energy bands for all selected observations, allowing a direct comparison of their behavior over a broad energy range.

This analysis is also carried out using only XMM-Newton observations, as they provide higher signal-to-noise ratio and superior spectral resolution compared to *Swift*-XRT. In contrast, the relatively lower photon statistics and smaller effective area of *Swift*-XRT limit its suitability for detailed energy-resolved studies of the fractional amplitude, particularly when the data are divided into multiple energy bins.

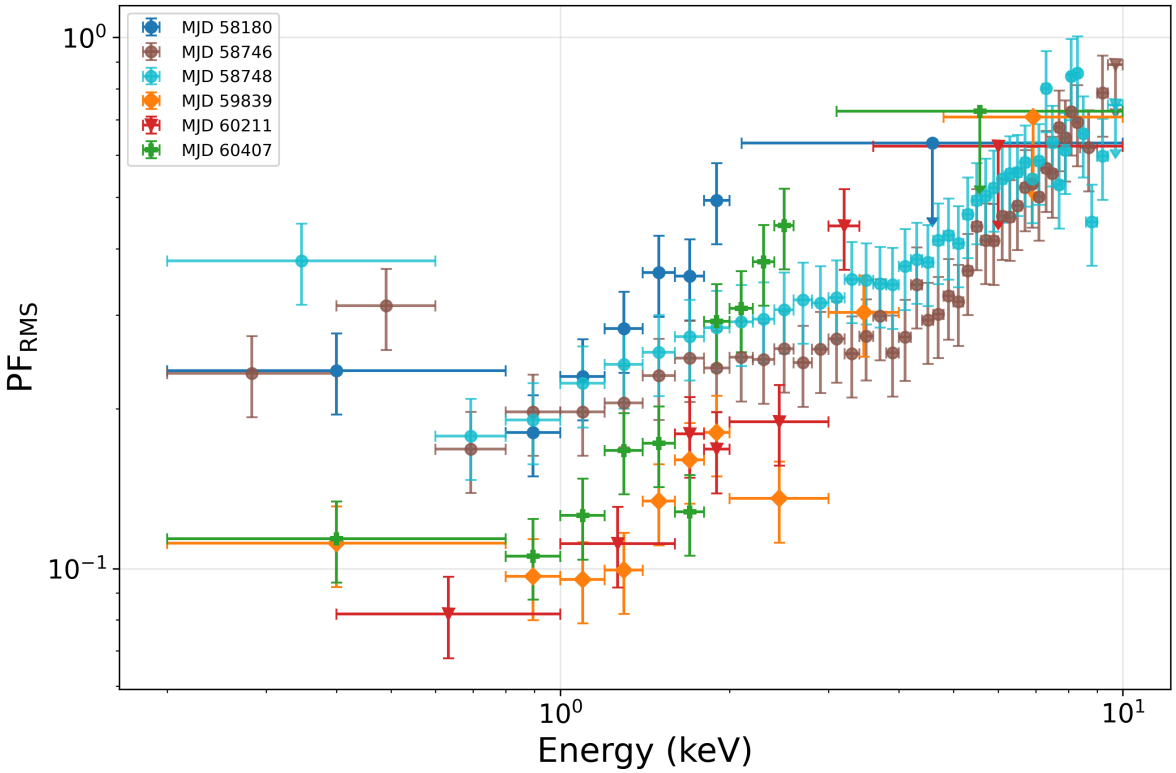


Figure 3.23: Energy-dependent pulsed fraction for all *XMM-Newton* observations, shown on logarithmic scales for both axes.

We infer the following from the plot:

- **Increase of Pulsed Fraction with Energy:** Across all epochs, the pulsed fraction generally increases with energy. It is lower in the soft X-ray band and becomes significantly higher at harder energies. This suggests that the higher-energy emission is more strongly modulated, likely originating from more localized or anisotropic regions.

- **Variation Across Epochs:** The overall level of pulsed fraction changes with time. Earlier observations show higher values, while later epochs exhibit weaker modulation. This indicates that the emission was more anisotropic soon after the outburst, and gradually becomes more uniform as the source evolves toward quiescence.

- **Similar Behaviour at High Energies:** At higher energies ($\gtrsim$5–7 keV), the pulsed fraction values from different epochs tend to lie within a relatively narrow range, even though the uncertainties are larger. This suggests that the high-energy emission component—likely linked to magnetospheric processes—maintains fairly stable modulation properties, even as the softer thermal emission continues to evolve.

3.6.2 Evolution of Pulsed Fraction with energy for each observation

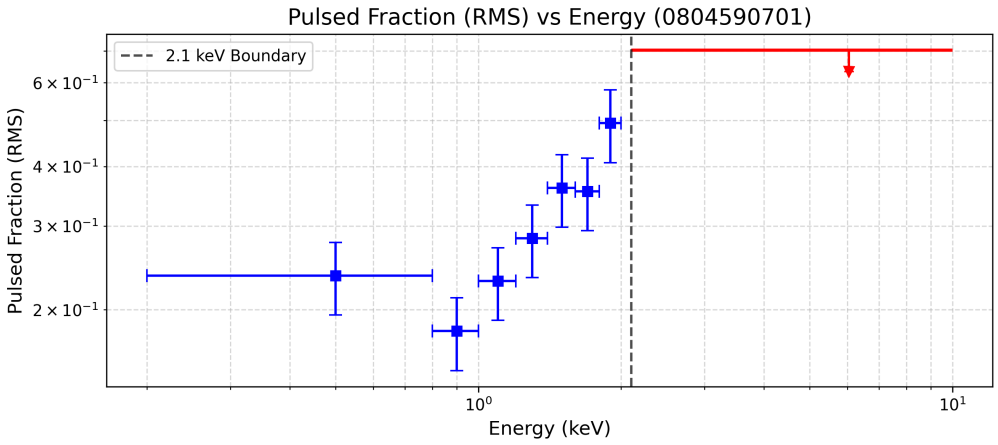


Figure 3.24: Energy dependence of the pulsed fraction for the first *XMM-Newton* observation, shown in linear and log–log scales to highlight behaviour across different energy ranges.

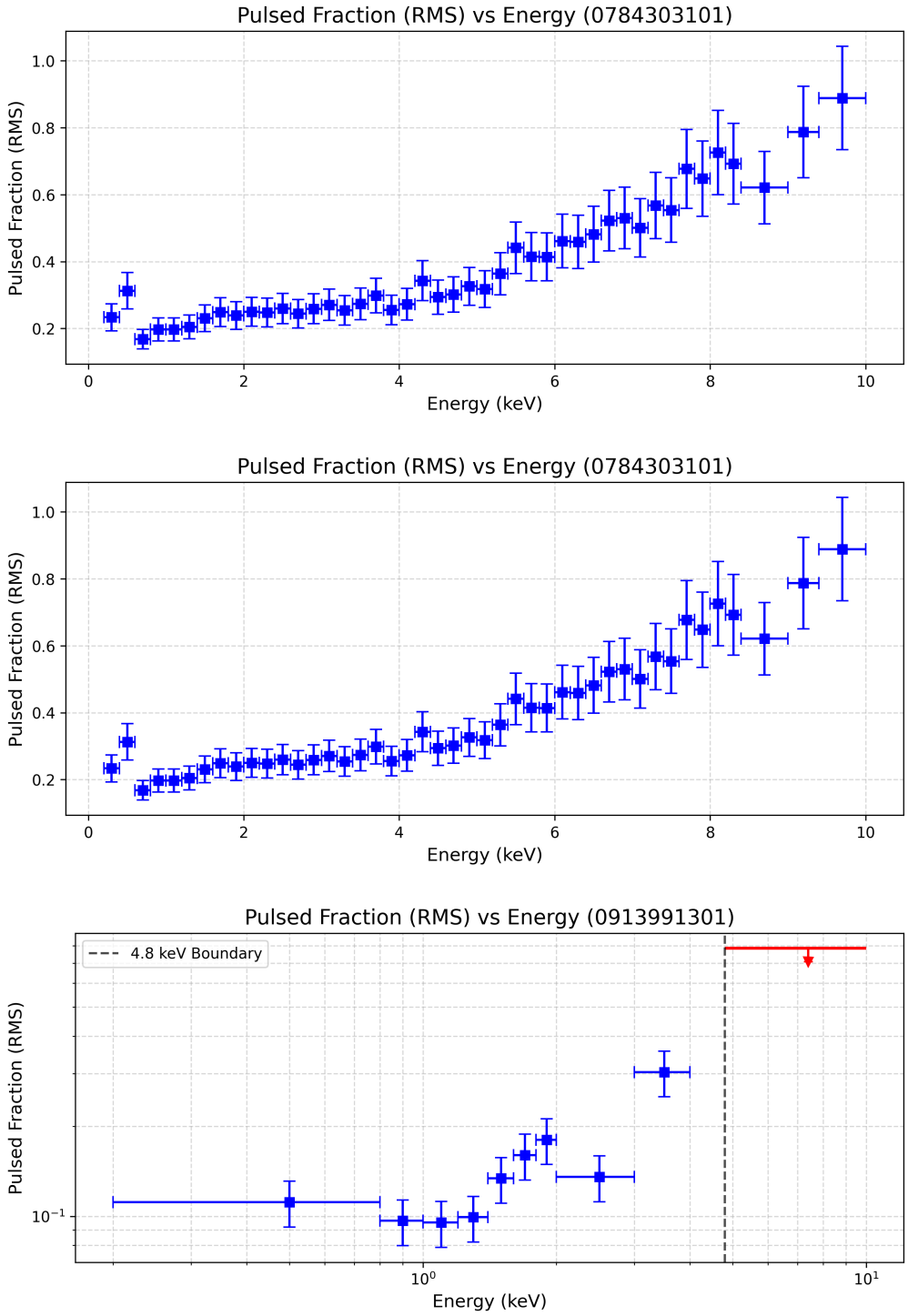


Figure 3.25: Energy dependence of the pulsed fraction for selected *XMM-Newton* observations. The first two panels are shown in linear scale, while the third panel is presented in log–log scale.

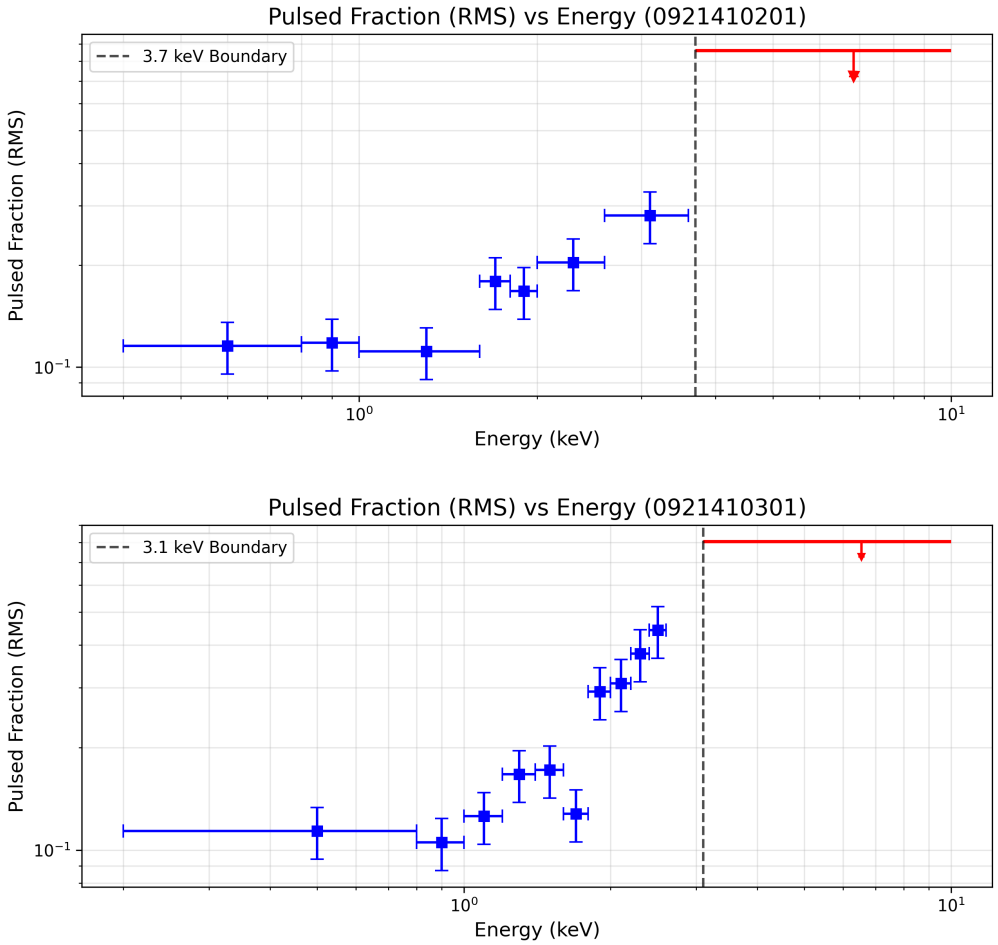


Figure 3.26: Energy dependence of the pulsed fraction for *XMM-Newton* observations, shown in log–log scale.

We can infer the following from the plots:

- **Increase of Pulsed Fraction with Energy:** In all observations, the pulsed fraction steadily increases with energy. It starts off lower in the soft X-ray band and becomes significantly higher at harder energies. This suggests that the higher-energy emission is more strongly modulated, likely arising from hot regions or magnetospheric processes.
- **Stronger Energy Dependence in Early Epochs:** In the early post-outburst observations, this increase with energy is more pronounced, with the pulsed fraction reaching higher values above ~5–6 keV. This indicates that the emission was more anisotropic during the initial stages, possibly due to enhanced magnetospheric activity and stronger temperature contrasts across the neutron star surface.

- **No Clear Saturation at High Energies:** Within the observed energy range, the pulsed fraction continues to increase without showing a clear sign of saturation. This suggests that the higher-energy emission remains strongly anisotropic and is not dominated by a uniform component. Such behaviour is consistent with a significant contribution from magnetospheric scattering processes, which can sustain strong modulation even at higher energies.

3.7 Correlation between X-ray pulsed fraction and radio flux density

In this section, we compare the evolution of the X-ray pulsed fraction with the radio flux density to investigate any possible correlation between the two. Figure 3.27 shows that the pulsed fraction is initially high, indicating strongly anisotropic emission from a hot region on the neutron star surface. As time progresses, the pulsed fraction decreases significantly, which is consistent with the cooling and possible expansion of the emitting region.

In contrast, the radio emission appears at later epochs and exhibits variability that does not show a clear correlation with the X-ray pulsed fraction. This suggests that the X-ray and radio emissions are governed by distinct physical processes. While the X-ray pulsed fraction reflects the geometry and thermal structure of the neutron star surface, the radio flux density traces magnetospheric activity. The observed behavior is consistent with a scenario in which the magnetosphere evolves following the outburst, becoming capable of sustaining radio emission as the surface hot spot cools. This points to a complex interplay between surface thermal emission and magnetospheric processes, rather than a direct one-to-one coupling between the two.

Taken together, the timing analysis provides a clear picture of the source evolution following the outburst. The decrease in pulsed fraction, along with changes in the pulse profile and its energy dependence, suggests a gradual shift from a strongly anisotropic emission pattern to a more uniform one. This is consistent with the cooling of hot regions on the neutron star surface and the gradual relaxation of the magnetosphere.

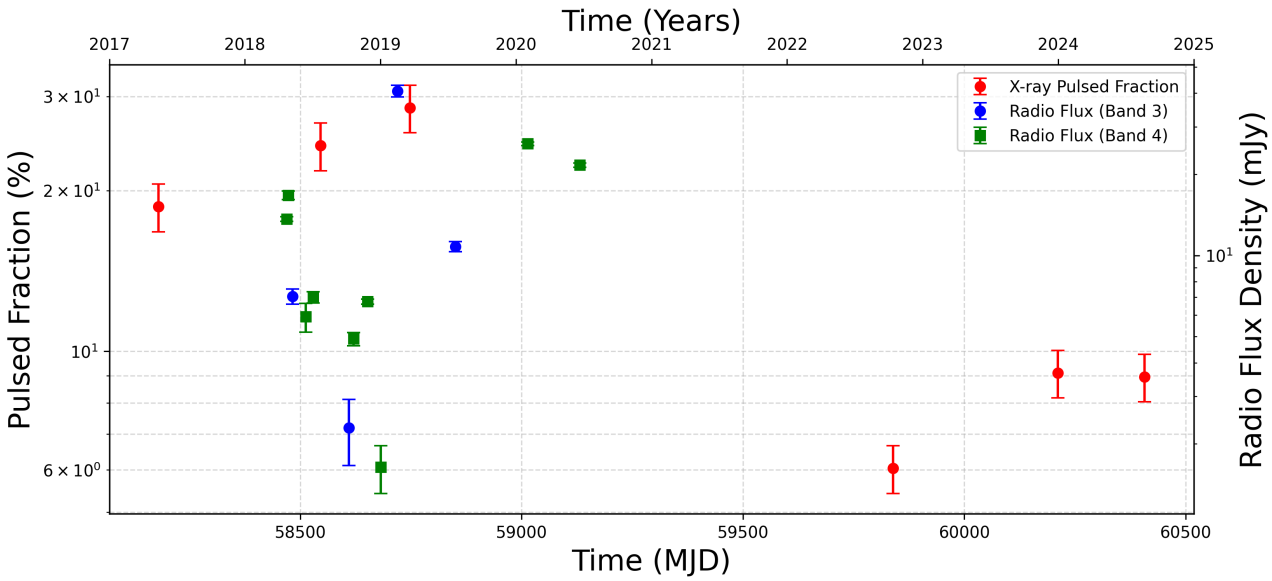


Figure 3.27: Evolution of X-ray Pulsed Fraction and Radio Flux density.

At the same time, timing analysis alone cannot fully separate the contributions from thermal surface emission and magnetospheric processes. To better understand the physical origin of the emission and how it evolves, we examine the spectral properties of the source. In the following chapter, we carry out a detailed spectral analysis to study the evolution of the underlying emission components.

Chapter 4

Spectral Properties

Spectral analysis is one of the most effective ways to understand the physical conditions and emission processes in compact objects. While timing studies help us uncover periodicities and rotational behavior, spectral analysis tells us how the emitted energy is distributed across different photon energies. This, in turn, allows us to probe the underlying physical mechanisms responsible for the observed radiation.

During outbursts, the X-ray emission is typically characterized by a combination of thermal and non-thermal components. The thermal emission, usually modeled as a blackbody, originates from heated regions on the neutron star surface. As the outburst begins, both the temperature and the emitting area can increase significantly, indicating energy injection into the crust. As the source evolves back toward quiescence, this heated region gradually cools, and its evolution can be tracked through changes in these spectral parameters. Alongside this, a non-thermal component, which is described by a power-law, is often present, arising from processes in the magnetosphere such as resonant cyclotron scattering. The evolution of this component during the decay phase provides valuable insight into changes in the magnetospheric structure, including the gradual untwisting of magnetic field lines and the dissipation of currents.

The change in temperature, flux and emitting radii can tell us the initial energy release and subsequent relaxation of the source. Taken together, the evolution of these spectral components offers a coherent picture of the physical processes governing the outburst. In this chapter, we focus on the spectral properties of the source during its active phase. We begin with the extraction of spectra from the observational data, followed by detailed modeling using physically motivated components.

We then examine the temporal evolution of key spectral parameters to better understand the behavior of the source throughout and beyond the outburst.

4.1 Spectral Extraction

The spectral extraction was performed using the Science Analysis System (SAS) for XMM-Newton EPIC-PN observations. The analysis began with the preparation of the data by setting the appropriate environment variables, namely `SAS_ODF` and `SAS_CCF`, which define the observation data files and calibration index files required for the processing.

Cleaned and filtered event files were used for spectral extraction. Source and background regions were defined using `ds9`, ensuring that the source region encompassed the maximum signal while avoiding contamination, and that the background region was selected from a nearby source-free area on the same detector.

Spectra were extracted using the `evselect` task, applying standard filtering criteria of `FLAG==0` and `PATTERN<=4` to retain only high-quality single and double pixel events. For imaging mode observations, circular regions were used to define the source and background extraction areas. In timing mode observations, rectangular regions in detector coordinates (`RAWX`) were used instead, appropriate for the one-dimensional spatial information in this mode.

Following the extraction, the `backscale` task was applied to both source and background spectra to compute the scaling factors corresponding to the extraction regions. Instrumental response files were then generated: redistribution matrix files (RMFs) were created using `rmfgen`, and ancillary response files (ARFs) were produced using `arfgen`, accounting for the effective area and detector response.

To prepare the spectra for fitting, the extracted spectra were grouped using the `specgroup` task. A minimum of 50 counts per bin was imposed to ensure the validity of χ^2 statistics during spectral fitting, and an oversampling factor of 3 was used to avoid over-resolving the instrumental response.

The final output of this procedure consists of grouped source spectra, corresponding background spectra, and the associated response files (RMF and ARF), which together form the inputs for subsequent spectral modeling.

4.2 Spectral Modelling

The extracted spectra were modeled using the XSPEC spectral fitting package. The primary objective of the spectral modelling is to characterize the observed X-ray emission in terms of physically meaningful parameters and to understand the underlying emission processes.

Magnetar spectra are typically described by a combination of thermal and non-thermal components, reflecting contributions from the neutron star surface and its magnetosphere. During outburst phases, these components evolve significantly, making spectral modelling an essential tool for probing the physical changes occurring in the system.

In this work, we model the spectra to quantify these components and to investigate their evolution across different observations. The specific models used and the fitting procedures are described in the following sections.

4.2.1 Blackbody and Power-law Spectral Components

The X-ray spectra of magnetars are typically characterized by a combination of thermal and non-thermal emission components, reflecting contributions from both the neutron star surface and its magnetosphere. In this work, the spectral continuum is modeled using an absorbed blackbody plus power-law model, implemented in XSPEC as `tbabs*(bbodyrad + powerlaw)`.

The `tbabs` component accounts for interstellar absorption along the line of sight, parameterized by the equivalent hydrogen column density ($N_{\rm H}$). This absorption predominantly affects the low-energy part of the spectrum and must be properly accounted for in order to recover the intrinsic source emission.

The thermal emission is described using the `bbodyrad` component, which represents blackbody radiation from the neutron star surface. This component is characterized by a temperature (kT) and a normalization that is related to the effective emitting radius. During magnetar outbursts, this thermal emission is associated with heating of the neutron star crust, leading to the formation of hot spots. The evolution of the temperature and emitting area provides important insight into the cooling of the crust as the source returns to quiescence.

In addition to the thermal emission, a non-thermal component is often required to adequately describe the high-energy tail of the spectrum.

This is modeled using a power-law, characterized by a photon index (Γ) and normalization. The power-law component is generally interpreted as arising from magnetospheric processes, such as resonant cyclotron scattering of thermal photons by charged particles. The evolution of this component during the outburst decay phase reflects changes in the magnetospheric configuration, including the untwisting of magnetic field lines and the dissipation of currents.

The combined blackbody and power-law model thus provides a phenomenological description of magnetar emission, capturing both surface heating and magnetospheric contributions. By fitting this model to the observed spectra, key physical parameters can be extracted and used to study the behavior of the source during and after the outburst.

4.2.2 Model Selection and Goodness of Fit

To determine the most appropriate spectral model, the extracted spectra were fitted using multiple models, including a single blackbody (1BB), a blackbody plus power-law (1BB+PL), and a two-blackbody model (2BB). The comparison of these models allows us to assess the relative contributions of thermal and non-thermal emission components and to identify the model that best describes the observed data.

Spectral fitting was performed using the XSPEC package over the energy range where the instrument response is well calibrated. The spectra were grouped to ensure a sufficient number of counts per bin, enabling the use of χ^2 minimization.

The fitting procedure involved initially allowing all model parameters to vary freely, followed by iterative refinement based on the quality of the fit. In some cases, the hydrogen column density ($N_{\rm H}$) was fixed or tied across observations to reduce parameter degeneracy and improve the stability of the fits.

The goodness of fit was evaluated using the reduced χ^2 statistic, along with a visual inspection of the residuals. Significant systematic deviations in the residuals indicate that the model is inadequate and requires additional components. A successful model is characterized by a reduced χ^2 value close to unity and residuals that do not show any systematic trends.

By comparing the statistical quality of the fits and the physical plausibility of the models, the most appropriate model was selected for each

observation. This ensures that the derived spectral parameters are both statistically robust and physically meaningful. The spectral fits for each observation are presented in the following figures and tables.

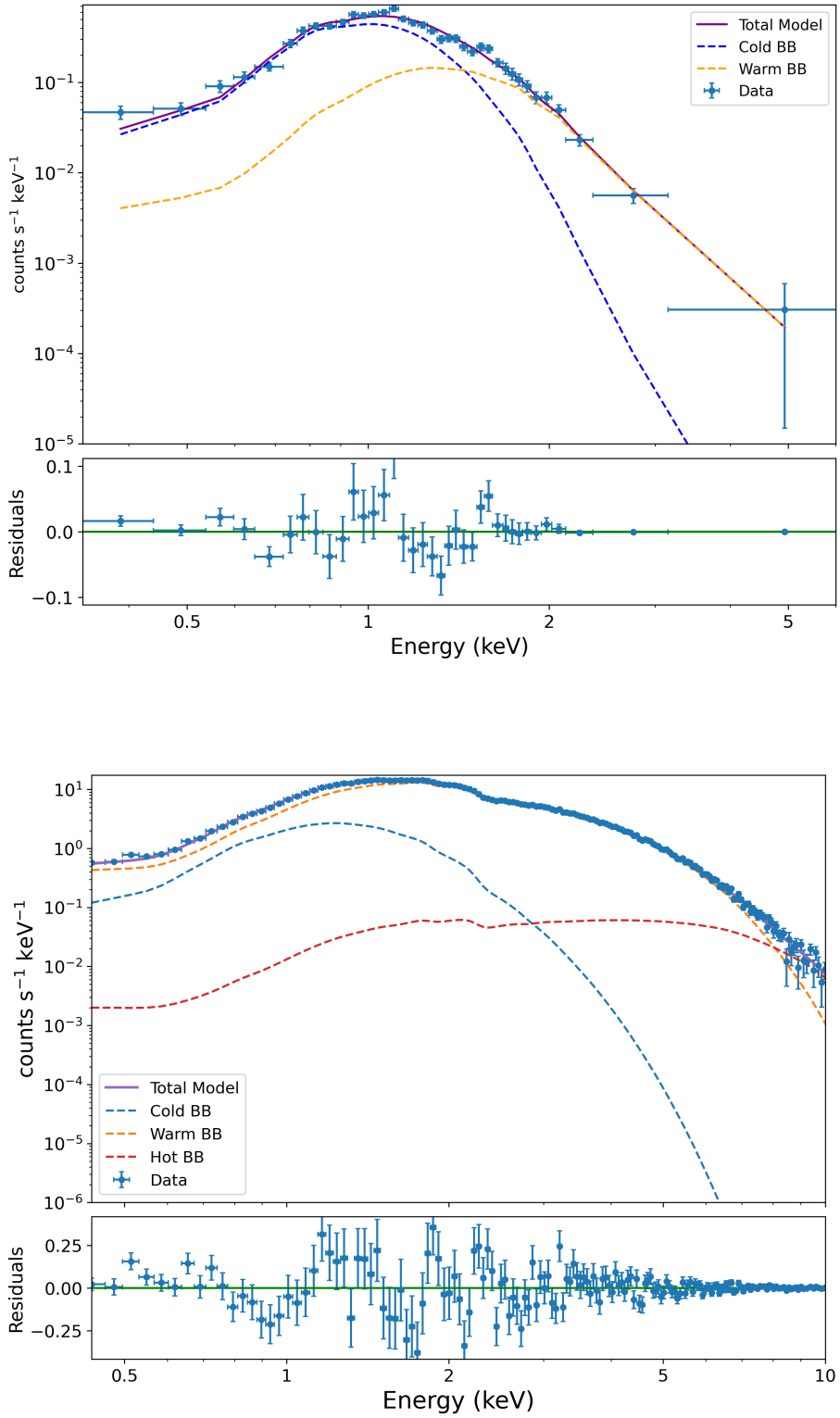


Figure 4.1: Best fit XMM-Newton spectra for pre 0804590701 (top, 2BB) and peak of the outburst 0784303101 (bottom, 3BB).

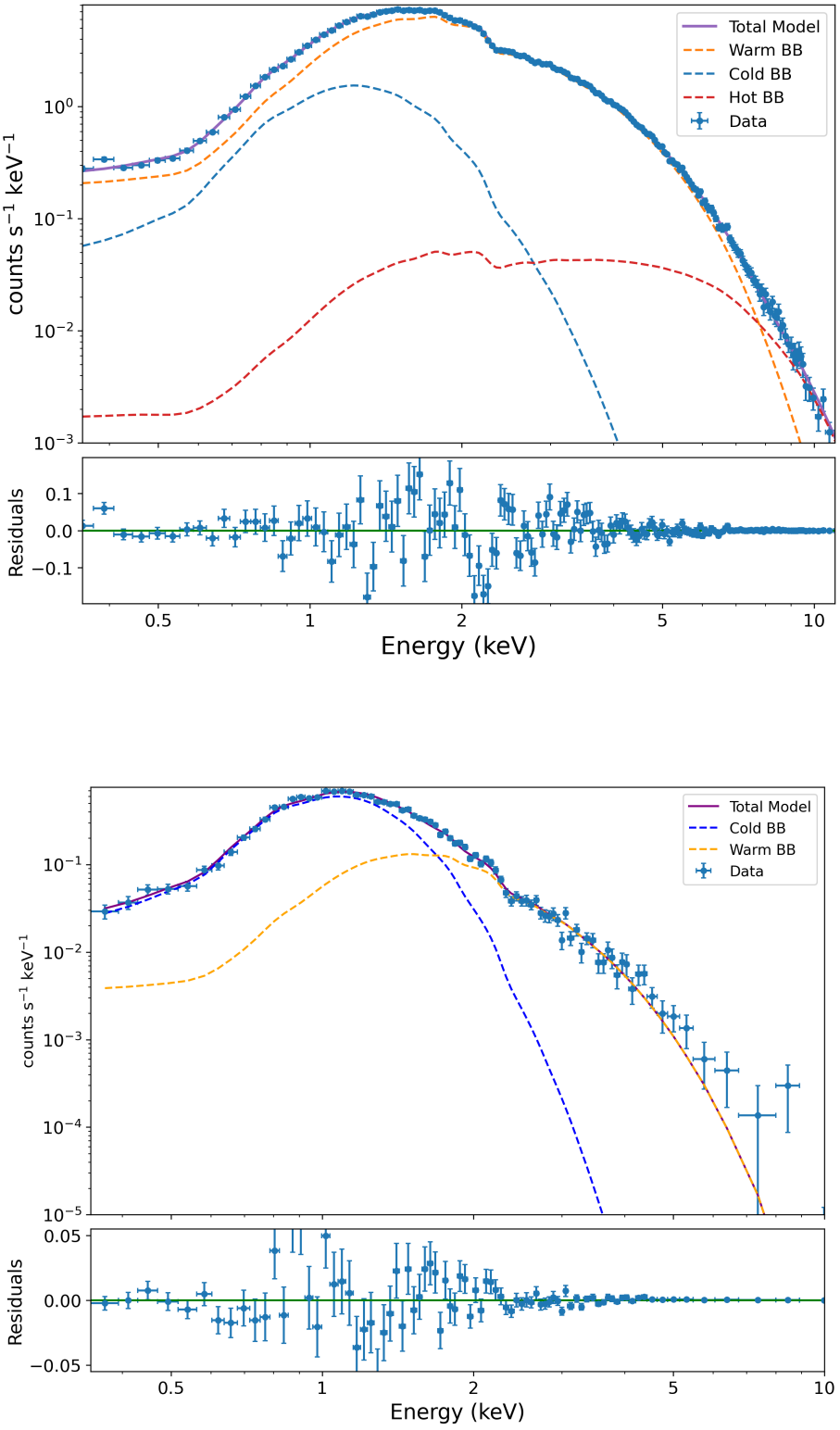


Figure 4.2: Best-fit XMM-Newton spectra showing spectral evolution from peak of the outburst 0784303201 (22-09-2019) and the later phase of the outburst 0913991301 (17-09-2022). The peak of the outburst has been fitted with 3BB components, and the later phase of the outburst has been fitted with 2BB components.

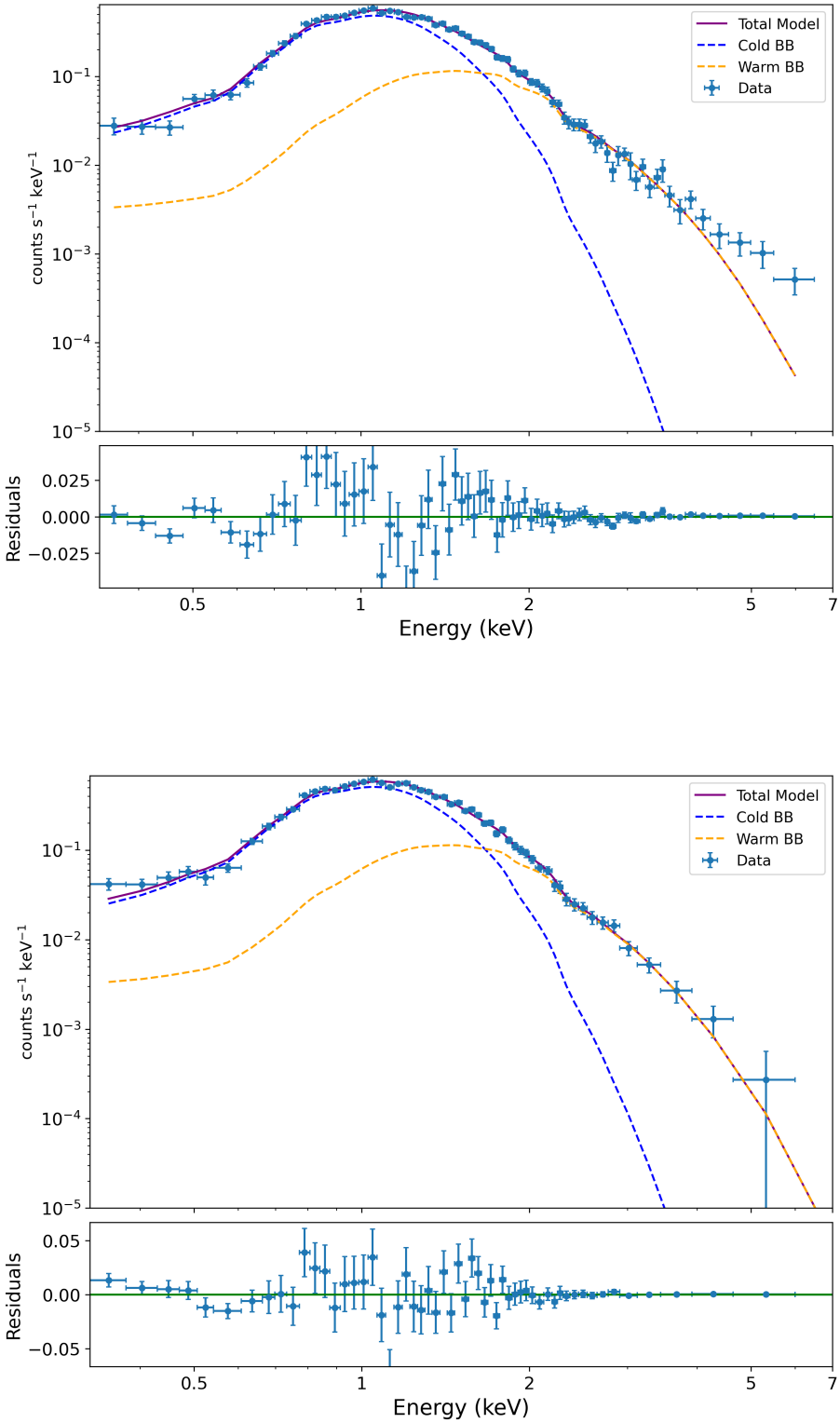


Figure 4.3: Best-fit XMM-Newton spectra showing spectral evolution at the later phases of the outburst 0921410201 (24-09-2023) and 0921410301 (07-04-2024). Both of the spectra has been fitted with 2BB components.

4.3 Temporal Evolution of spectral parameters

We now examine the temporal evolution of the spectral parameters obtained from the spectral fitting. This allows us to track how the emission properties of the source change over time following the outburst.

From Table 4.1, given in the next page, the spectral parameters show a clear evolution across the observations. The lower-temperature component (kT_1) remains relatively stable over time, indicating that the cooler emission region is not strongly affected by the outburst decay. Its corresponding emitting radius (R_1) is comparatively large, of the order of several kilometers, and shows only modest variation, suggesting that this component likely originates from a broader region of the neutron star surface.

In contrast, the higher-temperature component (kT_2) exhibits a gradual decrease with time, accompanied by a reduction in its emitting radius (R_2). This behavior is consistent with the cooling and shrinking of a hot spot formed during the outburst, as the deposited energy is radiated away and the heated region contracts.

Additionally, a third, higher-temperature component is present in the earlier observations but is absent in later epochs. This suggests that the thermal structure of the emission is more complex during the initial stages of the outburst and gradually simplifies as the source evolves. Overall, these trends are consistent with the cooling of heated regions on the neutron star surface following the outburst.

Table 4.1: Blackbody temperatures, normalizations, and inferred emitting radii assuming a source distance of 3.5 kpc.

Epoch	$N_{\rm H}$ (10^{22} cm^{-2})	kT_1 (keV)	R_1 (km)	kT_2 (keV)	R_2 (km)	kT_3 (keV)	R_3 (km)	χ^2/dof
0804590701	0.77 ± 0.18	0.16 ± 0.15	6.59 ± 5.49	0.23 ± 0.07	2.73 ± 6.74	–	–	82.10/32
0784303101	0.83 ± 0.02	0.27 ± 0.01	6.01 ± 0.98	0.71 ± 0.005	2.56 ± 0.71	2.56 ± 0.71	0.04 ± 0.02	212.33/158
0784303201	0.79 ± 0.01	0.28 ± 0.01	4.34 ± 0.47	0.69 ± 0.005	1.84 ± 0.03	1.92 ± 0.26	0.05 ± 0.01	325.11/165
0913991301	0.97 ± 0.03	0.17 ± 0.005	10.55 ± 1.20	0.47 ± 0.01	0.48 ± 0.04	–	–	119.57/82
0921410201	0.96 ± 0.04	0.17 ± 0.006	10.19 ± 1.42	0.41 ± 0.01	0.58 ± 0.07	–	–	126.73/71
0921410301	0.95 ± 0.04	0.16 ± 0.007	11.09 ± 1.86	0.38 ± 0.01	0.68 ± 0.12	–	–	115.76/70

Radius uncertainties are propagated from normalization errors.

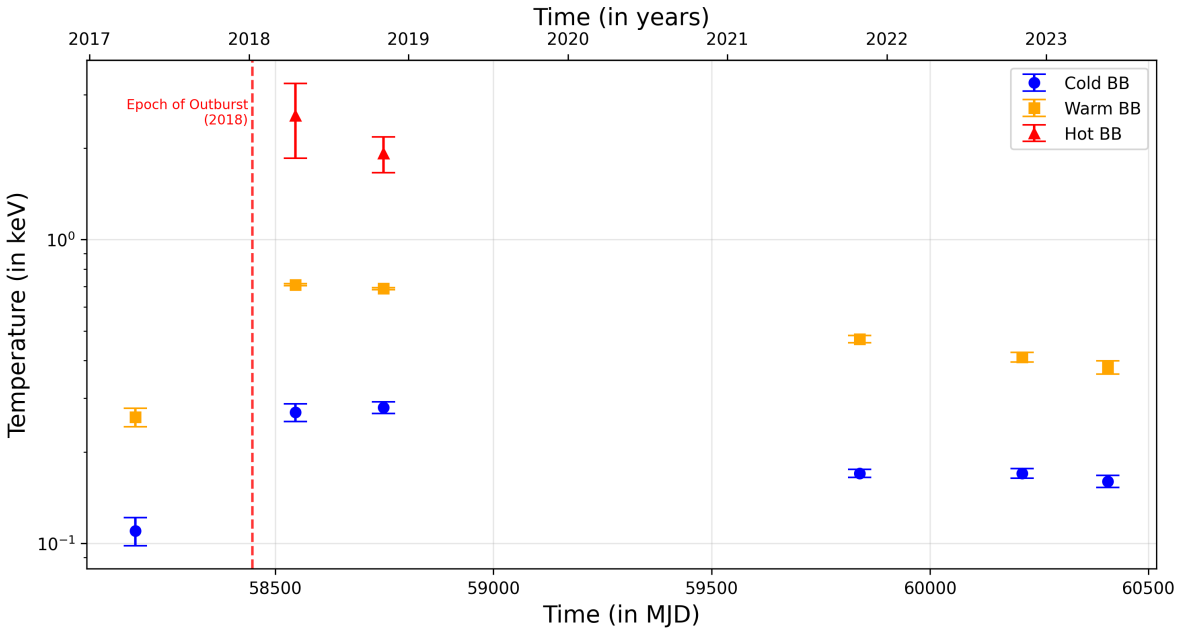


Figure 4.4: Temperature evolution.

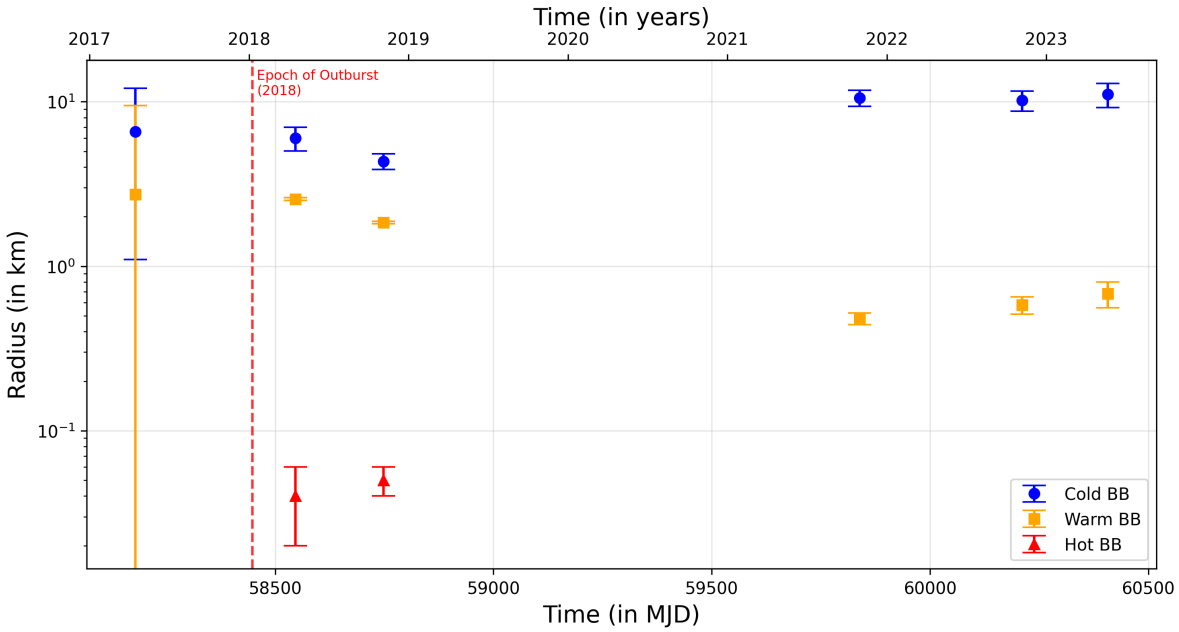


Figure 4.5: Radius evolution. The y-axis is in log scale.

4.3.1 Flux Evolution

Following the spectral analysis, we now examine the evolution of the X-ray flux across different observations. The flux values are derived from the best-fit spectral models and represent the total emission, along with contributions from individual blackbody components.

The measured fluxes for each observation are listed in Tables 4.2, including the total flux and the corresponding contributions from the cold, warm, and hot blackbody components. This decomposition allows us to track how different emission regions evolve over time during the outburst decay.

Table 4.2: Flux measurements from spectral fits

Epoch	Final Flux*	Cold BB Flux*	Warm BB Flux*	Hot BB Flux*
0804590701	$3.63^{+1.11}_{-0.89}$	$1.74^{+0.83}_{-0.56}$	–	$3.41^{+1.57}_{-1.08}$
0784303101	$15.40^{+0.05}_{-0.05}$	$1.92^{+0.20}_{-0.18}$	$14.70^{+0.06}_{-0.06}$	$0.38^{+0.05}_{-0.04}$
0784303201	$8.19^{+0.02}_{-0.02}$	$1.08^{+0.06}_{-0.06}$	$6.88^{+0.02}_{-0.02}$	$0.23^{+0.02}_{-0.02}$
0913991301	$0.98^{+0.07}_{-0.07}$	$0.876^{+0.076}_{-0.071}$	–	$0.106^{+0.004}_{-0.004}$
0921410201	$0.83^{+0.09}_{-0.08}$	$0.757^{+0.077}_{-0.070}$	–	$0.087^{+0.005}_{-0.005}$
0921410301	$0.90^{+0.14}_{-0.12}$	$0.817^{+0.099}_{-0.090}$	–	$0.088^{+0.007}_{-0.007}$

* Flux is reported in units of 10^{-11} erg cm^{-2} s^{-1}.

The flux evolution of the spectral components reveals a clear cooling trend following the outburst. The hot blackbody component dominates the emission at early epochs, indicating the presence of a thermal region on the neutron star surface. However, its flux decreases rapidly with time, suggesting efficient cooling of this confined hot spot. In contrast, the cold blackbody component remains comparatively stable across all observations, consistent with emission from a larger, cooler region that is less affected by the outburst. The transient appearance of an intermediate (warm) component in one epoch may indicate a phase of heat redistribution across the stellar surface or reflect model degeneracy during spectral fitting.

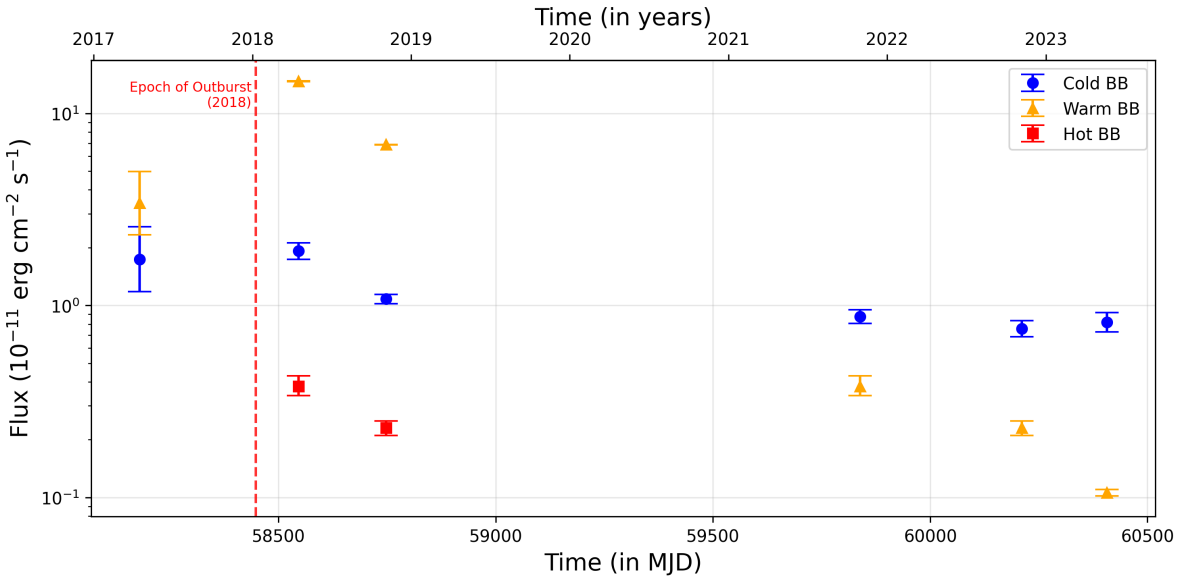


Figure 4.6: Flux evolution of each Blackbody components

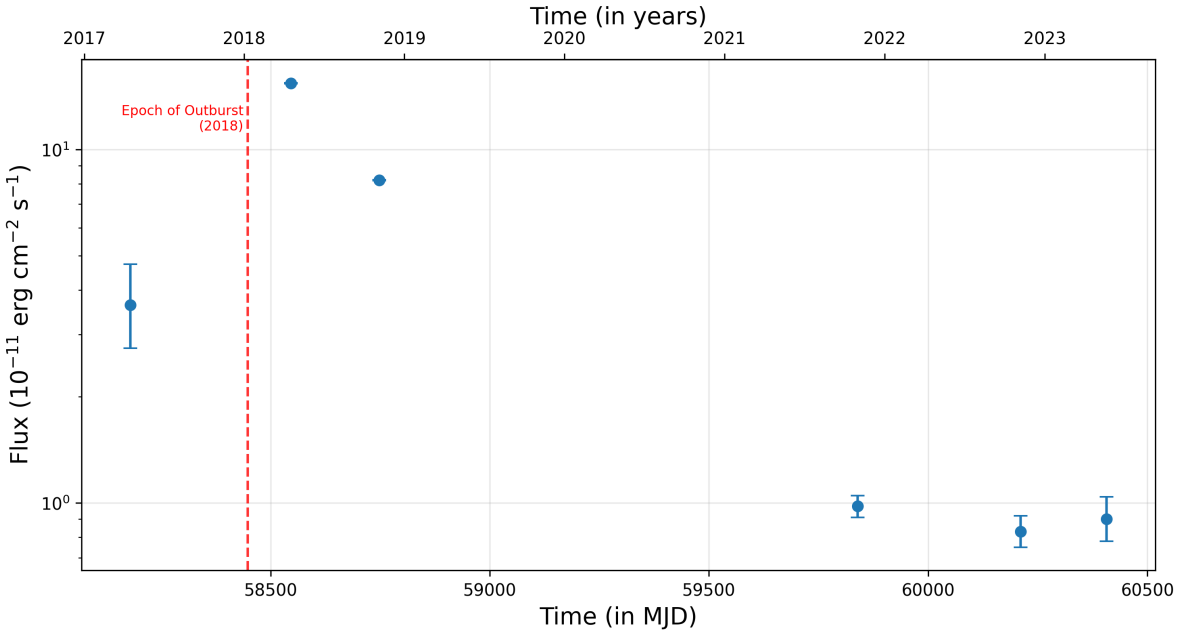


Figure 4.7: Final flux evolution

Chapter 5

Summary and Discussion

This chapter summarizes the key timing and spectral results of XTE J1810−197 following its 2018 reactivation, integrating pulse-profile evolution, thermal surface structure, and timing–spectral correlations to construct a unified physical picture of the source's outburst, magnetospheric reconfiguration, and long-term relaxation.

Timing properties

The timing evolution of XTE J1810−197 after its 2018 reactivation reflects how the neutron star's surface and magnetosphere physically changed as the outburst progressed. The timing parameters, such as pulse profile morphology, fractional amplitude (FA), total fractional amplitude (TFA), and pulsed fraction (PF), together reveal how the energy released during the outburst was distributed across the stellar surface and how that distribution evolved.

The gradual change in the pulse profile, shown in Figures 3.6 and 3.9, along with the decline in both FA and TFA (Figures 3.22 and 3.17), suggests that the source was initially dominated by small, unevenly heated surface regions. These were likely formed through intense crustal heating and magnetic field reconfiguration during the onset of the 2018 outburst. Similar behavior was also observed during the 2003 outburst, when early *XMM-Newton*, *Chandra*, and *RXTE* observations showed strong pulse modulation, complex pulse profiles, and enhanced thermal emission, suggesting surface heating and significant magnetospheric activity (Ibrahim et al. 2004; Gotthelf, Halpern, Buxton, et al. 2004; Bernardini et al. 2009). Following the 2018 reactivation, early NICER and XMM-Newton studies by (Borghese et al. 2018) and (Güver

et al. 2019) also reported strong pulse variability and evolving pulse structures. These were interpreted as signs of rapidly changing surface emission geometry. The similar behavior observed during both major outbursts suggests that each reactivation of this transient magnetar may repeatedly produce hot surface regions and significant changes in its external magnetic field structure. Over time, the decreasing pulse strength suggests that these initially small, intensely heated regions gradually cool and become less dominant, while emission from a larger portion of the neutron star surface becomes more important. This leads to a smoother and more uniform overall emission pattern. The relatively rapid decline of higher-order harmonics also suggests that smaller and more complex hotspot structures disappear earlier, while the broader large-scale surface emission remains stable for a longer time. Together, these trends support a picture in which the outburst initially generates surface heating and significant magnetospheric distortion. This is followed by gradual crustal cooling and untwisting of the external magnetic field. As proposed by (Beloborodov 2009), such behavior is broadly consistent with magnetothermal relaxation and untwisting magnetosphere models.

The strong variation of both FA and PF with energy, shown in Figures 3.18 and 3.23, suggests that different X-ray energy bands likely originate from different emission components or surface regions on the neutron star. The stronger modulation at higher energies is consistent with harder X-ray emission arising from smaller, hotter, and more unevenly heated surface regions. This suggests that temperature differences may increase rotational variability. On the other hand, softer X-rays likely contain a larger contribution from cooler, more extended surface regions, producing comparatively smoother modulation. A similar energy-dependent timing behavior was already observed during the 2003 outburst decay, where early *XMM-Newton*, *Chandra*, and *RXTE* studies found that PF increased with energy and that higher-energy emission was associated with stronger modulation, consistent with hotter regions superimposed on broader cooler surface emission (Gotthelf, Halpern, Buxton, et al. 2004; Bernardini et al. 2009). Spectral studies of the 2003 outburst also supported the presence of multiple thermal emission components, showing that the source evolved from smaller, hotter regions to broader and cooler surface emission as the outburst gradually faded (Bernardini et al. 2009; Alford and Halpern 2016). Likewise, in the 2018 reactivation, (Borghese

et al. 2018; Güver et al. 2019) reported distinct thermal surface zones and evolving pulse structures, again suggesting the presence of multiple heated regions with different temperatures and geometries. Taken together, the recurrence of this energy-dependent modulation across both major outbursts supports a common physical picture in which magnetar outbursts are associated with hot surface regions superimposed on a cooler large-scale stellar surface. This is most likely driven by crustal energy injection and magnetospheric reconfiguration. From this perspective, energy-resolved timing analysis becomes especially powerful, as it can provide indirect evidence for thermal stratification and surface complexity even before detailed spectral fitting is performed.

An equally important layer of interpretation emerges when these X-ray timing properties are compared with the source's radio behavior. This was already seen during the 2003 discovery outburst, when XTE J1810−197 became the first magnetar observed to exhibit transient pulsed radio emission following its X-ray brightening (Halpern et al. 2005; Camilo, Ransom, et al. 2006). They demonstrated that radio emission emerged following the major X-ray outburst and exhibited highly variable flux and pulse morphology. Following the 2018 reactivation, the renewed appearance of radio pulsations reported by (Camilo, Reynolds, et al. 2018) suggested that radio activity was associated with magnetospheric reconfiguration accompanying the outburst. Our results, as shown in 3.27, support this broader recurring picture. While the X-ray modulation appears to be governed primarily by the evolving thermal geometry of the neutron star surface, the radio variability is more likely reflecting broader changes in magnetospheric structure. The absence of a strict one-to-one correspondence between X-ray timing evolution and radio flux therefore suggests that radio activation is not determined solely by surface thermal evolution. Instead, previous studies have suggested that radio activation in magnetars may depend more sensitively on the magnetospheric state and whether magnetic field geometry remains favorable for sustaining coherent radio emission (Camilo, Ransom, et al. 2006; Beloborodov 2009). The repeated emergence of this pattern across both the 2003 and 2018 outbursts reinforces the idea that magnetar outbursts simultaneously trigger crustal heating and external magnetic restructuring, while these thermal and magnetospheric components may subsequently evolve semi-independently on different physical timescales.

Spectral Properties

The spectral evolution of XTE J1810−197 completes the picture of how the neutron star's thermal surface structure changes as the source gradually relaxes after outburst. By tracking the evolution of temperature, emitting radius, and flux across multiple blackbody components, the spectral behavior suggests that the 2018 reactivation did not produce purely uniform surface heating. Instead, it was associated with a thermally stratified surface composed of multiple emitting regions with distinct temperatures and spatial scales.

As shown in our analysis and referring to figure 4.5, the temperature evolution indicates that, during the early post-outburst phase, the neutron star surface can be described by at least three thermally distinct components: a very hot and compact component, an intermediate warm region, and a broader cooler surface component. This is broadly consistent with early XMM-Newton and NICER studies by (Borghese et al. 2018), which likewise identified a multi-component thermal structure and interpreted it as evidence for crustal heating superimposed on more widespread surface warming. A similar spectral evolution was also observed during the 2003 outburst, where early XMM-Newton analyses found that the spectrum was best described by multiple thermal components, including hotter regions that faded more rapidly than broader cooler emission as the source relaxed (Bernardini et al. 2009; Alford and Halpern 2016). In our analysis, the hottest component disappears relatively quickly and becomes undetectable at later epochs, while the warm and cool components persist over much longer timescales. This behavior suggests that the most intense heating immediately after reactivation was relatively short-lived and was likely caused by concentrated magnetic energy being deposited in small surface regions. By contrast, the longer persistence of the warm and cool components implies that broader surface heating relaxes more gradually through sustained crustal cooling and thermal diffusion. This evolution supports a physical picture in which magnetar outbursts initially deposit energy into small, intensely heated surface patches, followed by progressive cooling and redistribution of heat through the crust as the neutron star evolves toward a more stable thermal state.

Also, the evolution of the inferred emitting radii, shown in figure 4.4 provides important insight into how the surface geometry changes over time. The hottest component is associated with a very small emitting

area, consistent with compact hotspots or heated regions on the neutron star surface. In contrast, the cooler component covers a much larger area and gradually becomes the dominant source of emission at later epochs. This suggests that the star is not simply cooling uniformly. Instead, the spectral evolution reflects a transition from an early phase dominated by small, intensely heated hotspots to a later phase in which broader, large-scale thermal emission from the surface becomes increasingly important. This interpretation aligns naturally with the timing results. As compact hotspots fade and larger, cooler regions begin to dominate, the surface emission becomes progressively less anisotropic, which would naturally contribute to the observed decline in PF and FA.

The flux evolution of the three blackbody components, shown in figure 4.6, defined here as the hot (highest temperature), warm (intermediate temperature), and cold (lowest temperature) thermal regions, also provides an important physical view of how the outburst energy was distributed across different surface zones. In the early post-outburst phase, the warm component contributes the largest share of the total X-ray luminosity, implying that a substantial fraction of the released magnetic energy was deposited not only into very compact hotspots but also across broader intermediate-temperature regions. At the same time, the hot component declines rapidly, indicating that most of the heating fades relatively quickly. By contrast, the cooler component evolves more gradually and remains detectable throughout later observations. This layered pattern of flux decay indicates that the outburst affected the neutron star surface across multiple thermal zones, producing distinct emitting regions that cool on different physical timescales. A broadly similar spectral evolution was also reported during the 2003 outburst, where early XMM-Newton and Chandra studies found hotter components decayed more rapidly while broader cooler components persisted longer as the source relaxed toward quiescence (Gotthelf, Halpern, Buxton, et al. 2004; Bernardini et al. 2009; Alford and Halpern 2016). Likewise, early studies of the 2018 reactivation by (Borghese et al. 2018; Güver et al. 2019) also supported a multi-component thermal structure with evolving surface heating geometry. This multi-stage cooling behavior provides a plausible explanation for the timing evolution: stronger high-energy modulation during early epochs likely reflects compact hotter regions, while the declining modulation observed later is consistent with the

growing dominance of broader, cooler surface emission.

Finally, the evolution of the total flux, shown in Figure 4.7, reflects the overall energy release and gradual relaxation of the source following the outburst. The sharp rise in luminosity immediately after the 2018 reactivation shows that the source entered a highly energetic state. This was likely caused by the rapid release of stored magnetic energy, which was converted into thermal and radiative emission. Over time, this initial energetic phase was followed by gradual thermal cooling and magnetospheric relaxation. A broadly similar large-scale luminosity evolution was also observed during the 2003 discovery outburst. During that event, XTE J1810−197 showed a dramatic rise in X-ray luminosity, followed by a gradual long-term flux decay over several years as the source slowly returned toward quiescence (Ibrahim et al. 2004; Gotthelf, Halpern, Buxton, et al. 2004; Bernardini et al. 2009; Alford and Halpern 2016). A similar pattern was seen after the 2018 reactivation. Early studies by (Borghese et al. 2018; Güver et al. 2019; Gotthelf, Halpern, and Alford 2019) reported enhanced luminosity, spectral hardening, and evolving thermal structure immediately after reactivation, followed by continued long-term softening and flux decay. In both outbursts, the bright early phase likely reflects significant magnetic energy release and intense surface heating. The latter decline is consistent with gradual crustal cooling and relaxation of the external magnetic field. Our results are broadly consistent with this broader recurring framework, suggesting that the 2018 outburst, much like the 2003 event, triggered both intense short-term crustal heating and a prolonged period of residual thermal and magnetospheric relaxation.

Correlation between timing and spectral parameters

The combined evolution of timing and spectral properties provides a far more complete physical picture of XTE J1810−197 than either analysis alone, because together they directly connect thermal surface structure with observed emission geometry.

An important correlation is seen between hotspot temperature evolution and timing modulation strength. In the early post-outburst phase, the source shows hotter compact spectral components along with larger PF, stronger FA, and more structured pulse profiles. This indicates that hotter emitting regions play a major role in producing strong X-ray modulation.

As these hotter components gradually cool and their flux contribution decreases, PF and FA also decline. This suggests that as the temperature contrast between the hotspots and the surrounding surface becomes weaker, the observed rotational modulation also decreases. In this way, the long-term reduction in timing modulation is not driven only by geometric changes, but is also closely linked to thermal evolution, as cooling hotspots gradually lose their dominance over the pulse profile.

The evolution of the emitting radii also shows a clear connection with pulse morphology. Smaller inferred radii for the hotter components are associated with stronger pulse modulation and more complex harmonic structure. This indicates that compact thermal regions are more likely to produce sharper and more uneven emission patterns. As the broader cooler components gradually become more dominant, the pulse profiles become flatter and simpler. This correlation suggests that changes in spectral radius and the simplification of pulse structure are closely linked, and together they reflect the broader post-outburst relaxation of the source.

The evolution of harmonic structure provides additional insight into changes in the neutron star's surface geometry. A pulse profile dominated mainly by a single harmonic is often consistent with one dominant hotspot or one broad asymmetric emitting region. In contrast, the presence of multiple harmonics is often associated with more complex surface temperature distributions or emission geometries. This complexity may arise from multiple heated regions, irregular hotspot structures, or additional magnetospheric distortion. During the early stages of reactivation, the stronger second and third harmonics suggest that the surface likely contained multiple emitting zones or more complex hotspot configurations formed during the outburst. As these higher harmonics gradually weaken or disappear, the pulse profile becomes simpler over time. This likely reflects either a reduction in small-scale surface asymmetry or a decrease in temperature contrast between different emitting regions. Therefore, harmonic complexity can serve as an indirect indicator of hotspot multiplicity and surface geometric complexity. However, the exact number or arrangement of hotspots cannot be uniquely determined without detailed geometric modeling.

Chapter 6

Future directions

1. **Phase-Resolved Spectroscopy:** We primarily focused on phase-averaged spectral evolution; future phase-resolved spectroscopy would provide a much more direct probe of how different thermal components vary across rotational phase. By tracking temperature, radius, and flux as a function of pulse phase, it would become possible to identify whether individual pulse peaks correspond to distinct emitting regions.

2. **SWIFT Spectral Analysis** A comprehensive spectral analysis of the SWIFT/XRT observations will extend the temporal baseline beyond the discrete XMM-Newton epochs, enabling a much denser study of the long-term post-outburst evolution of XTE J1810−197. By tracking the evolution of spectral parameters such as blackbody temperatures, emitting areas, and flux decay across multiple SWIFT observations, this analysis will help bridge observational gaps between major XMM epochs and provide a more continuous picture of the source's thermal and magnetospheric evolution.

3. **Expanded Multi-Mission Monitoring with NICER:** A natural next step is to extend this work using NICER's high time resolution and dense monitoring capability to better capture the short-timescale timing evolution, particularly during the earliest post-outburst phase and later low-flux decay stages. Combining NICER with XMM-Newton and Swift would significantly improve temporal coverage, allowing more precise tracking of pulse-profile evolution, harmonic transitions, and long-term thermal relaxation.

Chapter 7

Appendix

7.1 XMM NEWTON data reduction using SAS

In order to start data analysis with XMM-Newton data using the **Science Analysis System (SAS)**, we first need to calibrate the data and then clean it. The calibration ensures that the observation data is properly associated with instrument response files and current calibration files (CCF), which is critical for accurate scientific analysis.

7.1.1 Calibrating the Data

Setting SAS Environment Variables

Before running any SAS task, it is important to define environment variables that point to the correct directories:

```
export SAS_ODF=path/to/source/ODF
export SAS_CCFPATH=path/to/source/CCF
```

- `SAS_ODF`: Specifies the location of the Observation Data Files (ODF) which contain raw event and housekeeping data from XMM-Newton.
- `SAS_CCFPATH`: Defines the directory containing the Current Calibration Files (CCF). These files provide essential information such as gain corrections, energy calibrations, and detector response matrices.

It is important to set these variables to the correct path, otherwise the calibration may be incorrect, resulting in unreliable scientific results.

Generate Calibration File (`ccf.cif`)

The calibration index file (`ccf.cif`) is created using the command:

```
cd path/to/ODF
cifbuild
```

This command scans the ODF directory, checks for required calibration files, and creates an index file (`ccf.cif`) that links the observation with appropriate calibration data.

Create Summary Files (.SAS)

Next, we define the location of the calibration file and generate a summary of the ODF content:

```
export SAS_CCF=path/to/ODF/ccf.cif
odfingest
```

The `odfingest` command generates summary files (with the extension `.SAS`) which contain structured information about the observation such as instrument modes, exposure times, and pointing information. These files are essential for further processing as they allow SAS to understand the observation structure.

Create Event Lists (.ds files)

Now, calibrated event lists is generated for each instrument (EPIC MOS and PN). This is done using:

```
export SAS_ODF=/path/to/ODF/(SummaryFile).SAS


emproc   # For EPIC MOS data
epproc   # For EPIC PN data
```

- `emproc`: Processes the raw ODF files for EPIC MOS detectors and creates event lists (with extension `.ds`).
- `epproc`: Processes the raw ODF files for EPIC PN detector and generates event lists.

These calibrated event lists are the starting point for scientific analysis, including light curve extraction, spectral analysis, and imaging.

7.2 Cleaning the Data and Plotting the light curve

After calibration, the next step is to clean the data by removing high-background intervals (also called **flares**) and creating Good Time Intervals (GTIs). This process ensures that only scientifically useful data is included in the analysis. The following steps describe the procedure:

7.2.1 Generate a Light Curve for Background Check

A light curve is generated from the calibrated event list to identify high-background flares:

```
evselect table=4456_0921410301_EPN_S003_ImagingEvts.ds \
withrateset=Y rateset=rate_EPN_evt.fits \
maketimecolumn=Y timebinsize=100 makeratecolumn=Y \
expression='#XMMEA_EP && (PI>10000) && (PATTERN==0)'
```

Explanation:

- `table`: The input calibrated event list (EPIC-pn in this case).
- `withrateset=Y` and `rateset`: Creates an output FITS file containing the light curve.
- `maketimecolumn=Y`: Adds a TIME column to the light curve.
- `timebinsize=100`: Bins the data in 100-second intervals.
- `makeratecolumn=Y`: Creates a RATE column for counts per second.
- `expression='#XMMEA_EP && (PI>10000) && (PATTERN==0)'`: Selects valid events based on:
  - `#XMMEA_EP`: Standard event filtering for EPIC-pn.
  - `PI>10000`: Uses high-energy photons (above 10 keV), which are mostly due to particle background and not astrophysical sources.
  - `PATTERN==0`: Selects only single-pixel events for accurate background estimation.

This light curve will help identify intervals of high background that need to be removed.

7.2.2 Plot the Light Curve

To check for background flares, the following command is used:

```
fplot rate_EPN_evt.fits TIME RATE - /XW offset=yes
```

Explanation:

- `fplot`: Plots the light curve from the FITS file.
- The columns `TIME` and `RATE` are plotted against each other.
- This helps us identify intervals with abnormally high count rates (background flares).

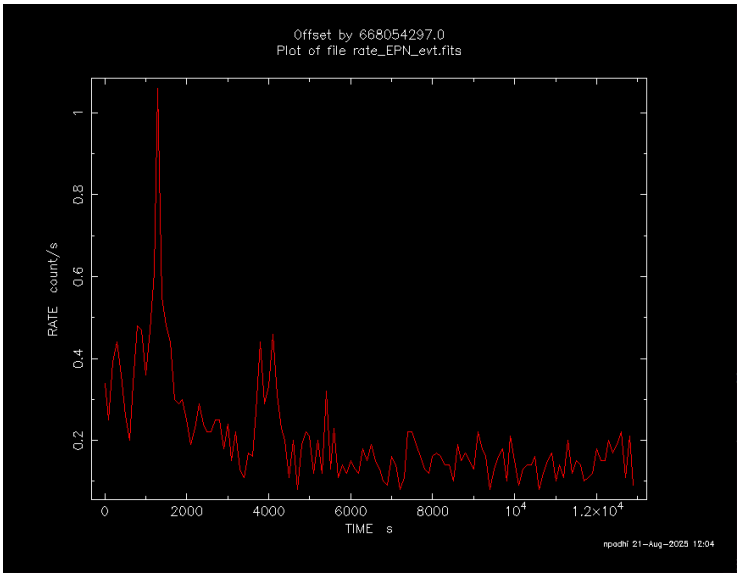


Figure 7.1: Preliminary Light curve to check for background flares. A spike can be clearly seen.

7.2.3 Determine Background Threshold using Sigma Clipping

To find a threshold for filtering flares, sigma clipping method is applied. The code in Python is as follows:

```
import numpy as np
from astropy.io import fits
from astropy.stats import sigma_clip
import matplotlib.pyplot as plt
```

```
with fits.open("rate_EPN_evt.fits") as hdul:
    data = hdul[1].data
    time = data["TIME"]
    rate = data["RATE"]

clipped_rate = sigma_clip(rate, sigma=3, maxiters=None)

median = np.median(clipped_rate)
std = np.std(clipped_rate)
threshold = median + 3 * std



plt.plot(time, rate, 'k.', alpha=0.5, label="Original")
plt.plot(time, clipped_rate, 'r.', alpha=0.8,
            label="Sigma-clipped")
plt.axhline(threshold, color="blue", linestyle="--",
            label=f"Threshold={threshold:.2f}")
plt.xlabel("Time (s)")
plt.ylabel("Rate (cts/s)")
plt.legend()
plt.show()

print(f"Suggested RATE threshold for tabgtigen:
            {threshold:.3f} counts/s")
```

Explanation:

- **Sigma clipping:** Removes outliers beyond a given standard deviation from the mean (here 3σ).
- **Threshold calculation:** The threshold is set as `median + 3`σ, which ensures that only high-background periods are excluded.

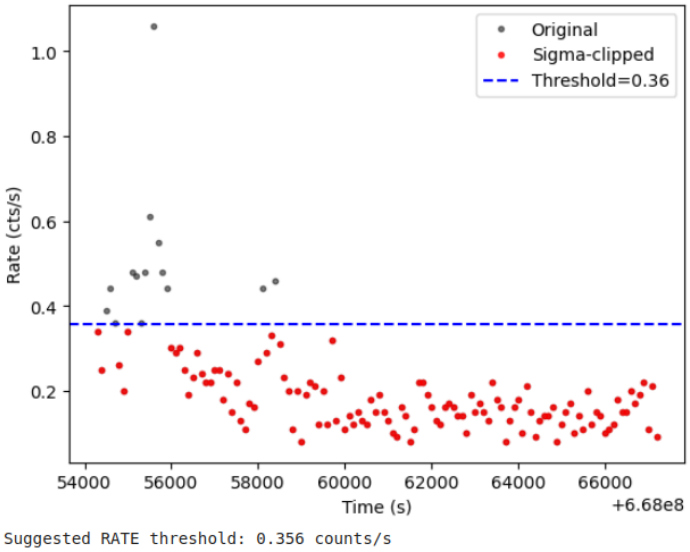


Figure 7.2: Plot depicting threshold to remove background flares.

7.2.4 Filter the Event File using GTI

After finding the threshold from sigma clipping method, it is evident to filter the event list to exclude intervals with high background:

```
evselect table=4456_0921410301_EPN_S003_ImagingEvts.ds \
withfilteredset=Y filteredset=clean_EPN_evt.fits \
destruct=Y keepfilteroutput=T \
expression='#XMMEA_EP && gti(GTI_EPN_evt.fits,TIME) && (PI>150)'
```

Explanation:

- `withfilteredset=Y` and `filteredset`: Creates a new filtered event file.
- `gti(GTI_EPN_evt.fits,TIME)`: Applies the Good Time Interval (GTI) filter to remove flared periods.
- `(PI>150)`: Rejects very low-energy events (below 150 eV), which are often noise.

7.2.5 Create a Cleaned Image from the Filtered Event List

Finally, create an image using the cleaned event file:

```
evselect table=clean_EPN_evt.fits imagebinning=binSize \
imageset=Image_clean_EPN_evt.fits withimageset=yes \
xcolumn=X ycolumn=Y ximagebinsize=80 yimagebinsize=80
```

Explanation:

- `xcolumn, ycolumn`: Use detector coordinates X and Y.
- `imagebinning=binSize`: Creates an image with a given bin size.
- `ximagebinsize, yimagebinsize=80`: Controls the resolution of the image.

This produces a cleaned X-ray image of the source, free from background contamination.

After filtering high background intervals and cleaning the event file, the next steps involves barycentric correction, and extracting the source and background light curves.

7.2.6 Display the Clean Image in DS9

```
ds9 Image_clean_EPN_evt.fits &
```

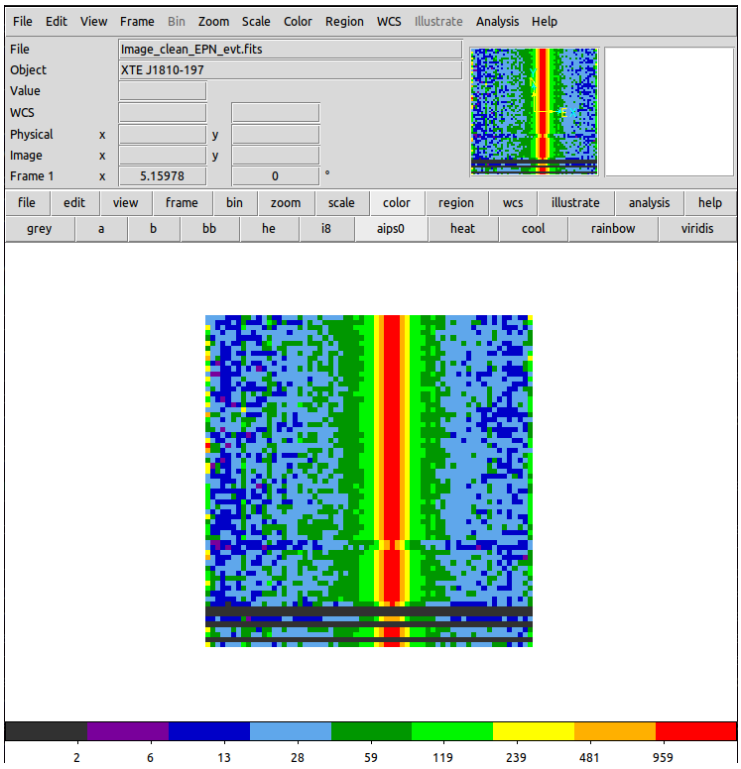


Figure 7.3: DS9 image for ObsID 0784303101 after filtering. This image is in Timing mode.

Explanation: This command opens the cleaned image in `DS9`, an astronomical imaging and data visualization tool. This allows us to visually inspect the cleaned image, verify the presence of the source, and identify the background region for extraction.

7.2.7 Apply Barycentric Correction

```
barycen withtable=yes table=clean_EPN_evt.fits:EVENTS \
        srcra=272.462862 srcdec=-19.731092
```

Explanation: The `barycen` task corrects the photon arrival times to the Solar System Barycentre using the given source coordinates (`srcra`, `srcdec`). This correction accounts for the motion of the XMM-Newton spacecraft and the Earth, which is essential for timing analysis (e.g., pulsar studies).

7.2.8 Extract the Source Light Curve

```
evselect table=clean_EPN_evt.fits \
expression='#XMMEA_EP && (PATTERN<=4) && \
((X,Y) IN circle(x,y,radius))' \
withrateset=yes rateset='lightcurve_EPN_evt_raw.lc' \
timebinsize=100 maketimecolumn=yes makeratecolumn=yes
```

Explanation: This command uses `evselect` to extract the source light curve from the cleaned event file:

- `#XMMEA_EP`: Selects good EPIC-pn events.
- `PATTERN<=4`: Includes single and double events (good for EPIC-pn).
- `(X,Y) IN circle(...)`: Extracts events within a circular region around the source.
- `timebinsize=100`: Bins light curve into 100s intervals.

This provides the raw light curve of the source region.

7.2.9 Extract the Background Light Curve

```
evselect table=clean_EPN_evt.fits \
         expression='#XMMEA_EP && (PATTERN<=4) &&
         ((X,Y) IN circle(23658.188,26912.801,642.40447))' \
         withrateset=yes rateset='bkg_lightcurve_EPN_evt_raw.lc'\
         timebinsize=100 maketimecolumn=yes makeratecolumn=yes
```

Explanation: This is similar to Step 8, but the extraction region is a background region (free of sources). Background subtraction is required to correct the source light curve for instrumental and cosmic background noise.

7.2.10 Apply Light Curve Corrections

```
epiclccorr srctslist=lightcurve_EPN_evt_raw.lc \
eventlist=clean_EPN_evt.fits outset=final_EPN.lc \
bkgtslist=bkg_lightcurve_EPN_evt_raw.lc \
withbkgset=yes applyabsolutecorrections=yes
```

Explanation: The `epiclccorr` task applies various corrections to the raw light curve:

- Background subtraction.
- Dead time correction.
- Exposure correction.
- Absolute corrections for the instrument.

This produces the final, scientifically valid light curve stored in `final_EPN.lc`, ready for timing or variability analysis.

Bibliography

[1] J. A. J. Alford and J. P. Halpern. "X-ray monitoring of the transient magnetar XTE J1810–197 from 2003 to 2014". In: *The Astrophysical Journal* 818.2 (2016), p. 122.

[2] J. Bell Burnell. "The past, present and future of pulsars". In: *Nature Astronomy* 1 (2017), pp. 831–834. DOI: 10.1038/s41550-017-0323-x.

[3] A. M. Beloborodov. "Untwisting Magnetospheres of Neutron Stars". In: *The Astrophysical Journal* 703 (2009), pp. 1044–1060.

[4] F. Bernardini et al. "The X-ray evolution of the transient anomalous X-ray pulsar XTE J1810–197". In: *Astronomy and Astrophysics* 498 (2009), pp. 195–207.

[5] A. Borghese et al. "XMM-Newton observations of the transient magnetar XTE J1810–197 during its 2018 outburst". In: *Monthly Notices of the Royal Astronomical Society* 489 (2018), pp. 1919–1930.

[6] F. Camilo, S. M. Ransom, et al. "Transient pulsed radio emission from a magnetar". In: *Nature* 442 (2006), pp. 892–895.

[7] F. Camilo, J. Reynolds, et al. "Revival of the Magnetar XTE J1810-197: Observations with the Deep Space Network". In: *The Astrophysical Journal Letters* 856 (2018), p. L37.

[8] E. V. Gotthelf, J. P. Halpern, and J. A. J. Alford. "Renewed X-ray activity of the transient magnetar XTE J1810–197 observed in 2018". In: *The Astrophysical Journal Letters* 874.2 (2019), p. L25.

[9] E. V. Gotthelf, J. P. Halpern, M. Buxton, et al. "The Return to Quiescence of the Transient Anomalous X-Ray Pulsar XTE J1810-197". In: *The Astrophysical Journal* 605 (2004), pp. 368–373.

[10] Tolga Güver et al. *NICER Observations of the 2018 Outburst of XTE J1810-197*. 2019. DOI: 10.3847/2041-8213/ab212d. arXiv: 1905.04440 [astro-ph.HE].

[11] J. P. Halpern et al. "Discovery of the Transient Anomalous X-Ray Pulsar XTE J1810-197". In: *The Astrophysical Journal Letters* 632 (2005), pp. L29–L32.

[12] A. I. Ibrahim et al. "Discovery of a Transient Magnetar: XTE J1810-197". In: *The Astrophysical Journal Letters* 609 (2004), pp. L21–L24.

[13] F. Jansen et al. "XMM-Newton observatory. I. The spacecraft and operations". In: *Astronomy & Astrophysics* 365 (2001), pp. L1–L6.

[14] V. M. Kaspi and A. M. Beloborodov. "Magnetars". In: *Annual Review of Astronomy and Astrophysics* 55 (2017), pp. 261–301. DOI: 10.1146/annurev-astro-081915-023329.

[15] M. Lyutikov. "Explosive reconnection in magnetars". In: *Monthly Notices of the Royal Astronomical Society* 346.2 (2003), pp. 540–554. DOI: 10.1046/j.1365-2966.2003.07110.x.

[16] Sandro Mereghetti. "The strongest cosmic magnets: soft gamma-ray repeaters and anomalous X-ray pulsars". In: *The Astronomy and Astrophysics Review* 15.4 (2008), pp. 225–287. DOI: 10.1007/s00159-008-0011-z. arXiv: 1202.1651 [astro-ph.HE].

[17] Swift Science Center. *The Swift Technical Handbook*. Version 12.0. 2015. URL: https://swift.gsfc.nasa.gov/archive/.

[18] C. Thompson and R. C. Duncan. "The Soft Gamma Repeaters as Very Strongly Magnetized Neutron Stars. I. Radiative Mechanism for Outbursts". In: *The Astrophysical Journal* 473 (1996), pp. 322–342. DOI: 10.1086/178147.

[19] R. Turolla, S. Zane, and A. L. Watts. "Magnetars: the physics behind observations". In: *Reports on Progress in Physics* 78.11 (2015), p. 116901. DOI: 10.1088/0034-4885/78/11/116901.

[20] XMM-Newton Science Operations Centre. *XMM-Newton Users Handbook*. 2022. URL: https://xmm-tools.cosmos.esa.int/external/xmm_user_support/documentation/uhb/.